

GEOLOGY OF THE FISHTIE COPPER DEPOSIT, CENTRAL PROVINCE, ZAMBIA

by

Michael Dean Hendrickson

A thesis submitted to the Faculty and the Board of Trustees of the Colorado School of Mines in partial fulfillment of the requirements for the degree of Master of Science (Geology).

Golden, Colorado

Date \_\_\_\_\_

Signed: \_\_\_\_\_  
Michael D. Hendrickson

Signed: \_\_\_\_\_  
Dr. Murray Hitzman  
Thesis Advisor

Golden, Colorado

Date \_\_\_\_\_

Signed: \_\_\_\_\_  
Dr. Paul M. Santi  
Professor and Head  
Department of Geology and Geological Engineering

## ABSTRACT

The Fishtie copper deposit is located in Central Province, Zambia, approximately three miles south of the border with the Democratic Republic of Congo. It contains approximately 55 Mt of 1.04% Cu at a 0.5% Cu cut-off in oxide, sulfide, and mixed oxide-sulfide ore. The deposit is hosted in the Grand Conglomérat unit and overlying Kakontwe Limestone unit of the lower Nguba Group. The Grand Conglomérat directly overlies basement schists and quartzites at Fishtie. Mineralized zones are located adjacent to high angle normal faults. The thickest successions of the Grand Conglomérat occur adjacent to these faults indicating they had synsedimentary movement. Fishtie contains iron formation within the Grand Conglomérat unit that consists of bands of nearly monomineralic to intermixed magnetite, ankerite, apatite, and quartz. Iron formation thickens towards normal faults suggesting the faults formed conduits for iron-rich hydrothermal solutions. The absence of iron formation clasts in the diamictite and presence of disseminated magnetite, ankerite, and apatite in adjacent diamictites suggests the iron formation formed by replacement of host rocks. Later hydrothermal alteration and mineralization at Fishtie overprinted the iron formation and affected the entire preserved sequence of Katangan sedimentary rocks and locally basement rocks. Copper mineralization at Fishtie is similar to that observed in some deposits of the Zambian Copperbelt where it has been attributed to interaction of an oxidized ore fluid with trapped natural gas. Copper precipitation was associated with both muscovite and chlorite mineralization, together with weak silicification. Copper sulfides at Fishtie display a relatively homogeneous distribution of generally heavy sulfur isotopic values that could have resulted from sulfide derivation from either a sour gas reservoir or thermochemical reduction of Neoproterozoic seawater sulfate.

## TABLE OF CONTENTS

ABSTRACT .....	iii
LIST OF FIGURES .....	vii
LIST OF TABLES .....	xi
ACKNOWLEDGEMENTS .....	xii
CHAPTER 1      INTRODUCTION .....	1
CHAPTER 2      REGIONAL GEOLOGY .....	7
CHAPTER 3      STRATIGRAPHY AND LITHOLOGY OF THE FISHTIE COPPER DEPOSIT .....	12
3.1      Basement Rocks .....	13
3.2      Nguba Group - Grand Conglomérat Unit .....	18
3.3      Nguba Group - Kakontwe Limestone .....	28
CHAPTER 4      STRUCTURAL GEOLOGY OF THE FISHTIE AREA .....	35
CHAPTER 5      DIAGENETIC AND HYDROTHERMAL MINERALIZATION .....	39
5.1      Diagenetic Mineralization .....	41
5.2      Iron Formation .....	42
5.3      Potassium Feldspar and Biotite Mineralization .....	46
5.4      Muscovite Mineralization .....	48
5.5      Chlorite Mineralization .....	48
CHAPTER 6      SULFIDE MINERALIZATION .....	56
6.1      Supergene Mineralization .....	61
6.2      Paragenetic sequence of mineralization .....	64
CHAPTER 7      CARBON AND OXYGEN ISOTOPES OF ALTERED ROCKS .....	67
CHAPTER 8      SULFUR ISOTOPES .....	69

CHAPTER 9	DISCUSSION.....	72
9.1	Stratigraphic and Structural Architecture .....	72
9.2	Rapitan Iron Formation.....	73
9.3	Potassium Feldspar and Phyllosilicate Mineralization .....	76
9.4	Post Iron Formation Hydrothermal Sulfide Mineralization.....	79
CHAPTER 10	CONCLUSIONS.....	82
REFERENCES CITED	.....	85
APPENDIX A	AEROMAGNETIC, RADIOMETRIC, INDUCED POLARIZATION AND LANDSAT DATA .....	94
A.1	Methods.....	94
A.2	Results.....	95
APPENDIX B	MAJOR ELEMENT AND TRACE ELEMENT GEOCHEMISTRY .....	105
B.1	Methods.....	105
B.2	Results.....	105
APPENDIX C	SOIL GEOCHEMISTRY SURVEY DATA AND PROJECTED TO SURFACE COPPER GRADE.....	119
C.1	Methods.....	119
C.2	Results.....	120
APPENDIX D	THREE-DIMENSIONAL MODELING .....	126
D.1	Methods.....	126
D.2	Results.....	126
APPENDIX E	MODAL ABUNDANCE OF MINERALS .....	130
E.1	Methods.....	130
E.2	Results.....	130
APPENDIX F	CARBON AND OXYGEN ISOTOPE ANALYSIS.....	132

F.1	Methods.....	132
F.2	Results.....	133
APPENDIX G	SULFUR ISOTOPE ANALYSIS .....	134
G.1	Methods.....	134
G.2	Results.....	134

## LIST OF FIGURES

Figure 1.1	Generalized geologic map of the Central African Copperbelt area.....	2
Figure 1.2	Generalized geologic map of the Lusale basin area.....	3
Figure 1.1	Location of drill holes at the Fishtie copper deposit.....	4
Figure 1.4	Generalized geologic map of the Fishtie copper deposit .....	5
Figure 2.1	Generalized stratigraphy of the Zambian Copperbelt and Fishtie copper deposit.....	8
Figure 3.1	Hand sample photographs of the major rock units at the Fishtie copper deposit.....	14
Figure 3.2	Cross sections through the western, central, satellite, and eastern structural domains of the Fishtie copper deposit .....	15
Figure 3.3	Photomicrographs of basement rocks at the Fishtie copper deposit .....	18
Figure 3.4	Hand sample and photomicrographs of clast rims .....	20
Figure 3.5	Photomicrographs of least altered Grand Conglomérat unit diamictite....	23
Figure 3.6	Lonestone of quartzite within magnetite- and ankerite-rich siltstone.....	25
Figure 3.7	Photomicrographs and QEMSCAN® images of Grand Conglomérat siltstone .....	26
Figure 3.8	Photomicrographs and QEMSCAN® images of Kakontwe dolostone and dolomitic siltstone.....	29
Figure 3.9	Carbon and oxygen isotopic values of unaltered and altered Kakontwe Limestone units, calcite veins, and ankerite in iron formation from Fishtie. ....	32
Figure 3.10	Chemostratigraphy of carbon and oxygen isotopic values .....	33

Figure 5.1	Schematic distribution of biotite, muscovite, and chlorite mineralized zones and location of hypogene and supergene ore zones.....	40
Figure 5.2	Photomicrographs of iron formation within the Grand Conglomérat unit..	45
Figure 5.3	QEMSCAN® images of iron formation within the Grand Conglomérat unit .....	46
Figure 5.4	Photomicrographs and QEMSCAN® images of biotite-mineralized zones in the Grand Conglomérat unit diamictite .....	49
Figure 5.5	Photomicrographs and QEMSCAN® images of muscovite-mineralized zones in the Grand Conglomérat unit diamictite .....	51
Figure 5.6	Photomicrographs and QEMSCAN® images of chlorite-mineralized zones in the Grand Conglomérat unit diamictite .....	53
Figure 5.7	QEMSCAN® image of chlorite-mineralized Kakontwe Limestone unit dolomitic siltstone.....	56
Figure 6.1	Distribution of sulfide minerals in sections C-C' and D-D' .....	57
Figure 6.2	Photomicrographs of sulfide textures .....	62
Figure 6.3	Paragenetic sequence of minerals at the Fishtie copper deposit .....	65
Figure 8.1	Histograms of sulfur isotopic values.....	70
Figure A-1	Reduced to pole (RTP) aeromagnetic maps.....	96
Figure A-2	Terraced aeromagnetic maps .....	97
Figure A-3	Horizontal Gradient filtered aeromagnetic maps .....	98
Figure A-4	Analytic Signal filtered aeromagnetic maps .....	99
Figure A-5	Potassium radiometric anomaly maps .....	100
Figure A-6	Uranium radiometric anomaly maps.....	101

Figure A-7	Thorium radiometric anomaly maps .....	102
Figure A-8	Induced polarization anomaly maps of the Fishtie area.....	103
Figure A-9	Landsat image of the Lusale basin and surrounding area .....	104
Figure B-1	Graphs of major element values (in weight %) of the basement, altered basement, Grand Conglomérat diamictite and siltstone, iron formation, Kakontwe Limestone unit, and quartz-carbonate veins from DDH KEDD0012 .....	108
Figure B-2	Graphs of trace element values (in ppm) of the basement, altered basement, Grand Conglomérat diamictite and siltstone, iron formation, Kakontwe Limestone unit, and quartz-carbonate veins from DDH KEDD0012 .....	110
Figure B-3	Graphs of metal values (in ppm) of the basement, altered basement, Grand Conglomérat diamictite and siltstone, iron formation, Kakontwe Limestone unit, and quartz-carbonate veins from DDH KEDD0012.....	112
Figure B-4	Graphs of rare earth element values (in ppm) of the basement, altered basement, Grand Conglomérat diamictite and siltstone, iron formation, Kakontwe Limestone unit, and quartz-carbonate veins from DDH KEDD0012 .....	114
Figure B-5	Graphs of heavy rare earth elements (values in ppm) of the basement, altered basement, Grand Conglomérat diamictite and siltstone, iron formation, Kakontwe Limestone unit, and quartz-carbonate veins from DDH KEDD0012.....	116
Figure B-6	Graphs of light rare earth element values (in ppm) of the basement, altered basement, Grand Conglomérat diamictite and siltstone, iron formation, Kakontwe Limestone unit, and quartz-carbonate veins from DDH KEDD0012 .....	118
Figure C-1	Soil geochemistry contours on RTP magnetic map of the Fishtie area: Cu, Co, P, Bi, S, As .....	121

Figure C-2	Soil geochemistry contours on RTP magnetic map of the Fishtie area: Al, Ca, Ca and Mg, Mg, Fe, Mn .....	122
Figure C-3	Soil geochemistry contours on RTP magnetic map of the Fishtie area: K, Na, Ba, Be, Mo, Pb .....	123
Figure C-4	Soil geochemistry contours on RTP magnetic map of the Fishtie area: Ag, W, V, Cr, Ti, Ni .....	124
Figure C-5	Projected to surface copper grade of the Fishtie copper deposit for comparison to soil geochemistry maps .....	125
Figure D-1	Three-dimensional model of the upper surface of basement rocks, copper grade, and drill holes .....	127
Figure D-2	Three-dimensional model of the upper surface of basement rocks, copper grade, drill holes, and faults .....	128
Figure D-3	Three-dimensional slices of the upper surface of basement rocks, copper grade, and drill holes .....	129
Figure E-1	Modal abundances of minerals .....	131
Figure G-1	Box and whisker plot of $\delta^{34}\text{S}$ (CDT ‰) values .....	136

## LIST OF TABLES

Table B-1	Major element values (in weight %) of the basement, altered basement, Grand Conglomérat diamictite and siltstone, iron formation, Kakontwe Limestone unit, and quartz-carbonate veins from DDH KEDD0012.....	107
Table B-2	Trace element values (in ppm) of the basement, altered basement, Grand Conglomérat diamictite and siltstone, iron formation, Kakontwe Limestone unit, and quartz-carbonate veins from DDH KEDD0012.....	109
Table B-3	Metal values (in ppm) of the basement, altered basement, Grand Conglomérat diamictite and siltstone, iron formation, Kakontwe Limestone unit, and quartz-carbonate veins from DDH KEDD0012.....	111
Table B-4	Rare earth element values (in ppm) of the basement, altered basement, Grand Conglomérat diamictite and siltstone, iron formation, Kakontwe Limestone unit, and quartz-carbonate veins from DDH KEDD0012.....	113
Table B-5	Heavy rare earth element values (in ppm) of the basement, altered basement, Grand Conglomérat diamictite and siltstone, iron formation, Kakontwe Limestone unit, and quartz-carbonate veins from DDH KEDD0012 .....	115
Table B-6	Light rare earth element values (in ppm) of the basement, altered basement, Grand Conglomérat diamictite and siltstone, iron formation, Kakontwe Limestone unit, and quartz-carbonate veins from DDH KEDD0012 .....	117
Table F-1	Carbon and oxygen isotopic values .....	133
Table G-1	Sulfur isotopic values .....	135

## ACKNOWLEDGEMENTS

This study was made possible by First Quantum Minerals Ltd. and the Colorado School of Mines. Advisor Dr. Murray Hitzman and Dr. David Wood were instrumental in guiding the project from inception to completion. Committee members Dr. Richard Wendlandt and Dr. John Humphrey provided essential service and advice throughout the process. Ground support from Shindano Kalenda ensured fieldwork was completed on schedule. Dr. Katharina Pfaff and Matt Dye facilitated QEMSCAN® analysis and data reduction, and deserve many thanks.

## CHAPTER 1

### INTRODUCTION

The Fishtie sedimentary rock-hosted copper deposit (formerly known as the Kashime prospect) is located southeast of the Zambian Copperbelt. The deposit is 30 km north of the village of Mkushi, Zambia and approximately five km south of the Congolese border (Figure 1.1). It was discovered in 2004 by First Quantum Minerals Ltd. through soil geochemistry prospecting (Appendix C). Fishtie is located on the northeast edge of the Lusale basin (Figure 1.2), a Katangan outlier enclosed by metavolcanic and metasedimentary rocks of the Irumide Belt (Stillman, 1965). Between 2004 and 2010 First Quantum Minerals Ltd. completed 268 drill holes on the property (Figure 1.3). Mineralized zones occur within the lower portion of the Nguba Group at a stratigraphic position above that which hosts the majority of deposits in the Zambian Copperbelt (Selley et al., 2005). The known extent of copper-sulfide mineralized rock at Fishtie is approximately 300m wide by over 1 kilometer along a roughly east-west strike. The deposit is currently estimated to contain approximately 55 million tons at 1.04% Cu in oxide, sulfide, and mixed oxide-sulfide ore (Hanssen, 2008).

This study is based on detailed core logging of three fences of diamond drill holes through the deposit (B-B', C-C', D-D'; Figure 1.4). The architecture of the deposit was further delineated using company drill logs of additional holes to construct four cross sections and one long section through the deposit area. These sections were utilized to create a three-dimensional model of the geology and distribution of copper grades. Regional magnetic geophysical data collected by First Quantum Minerals Ltd. were analyzed through reduction to pole and filtered using standard horizontal gradient, analytic signal and terracing techniques (Appendix A).

Geological, geophysical, and geochemical data were then gridded and analyzed to aid in reconstruction of the area's geology.

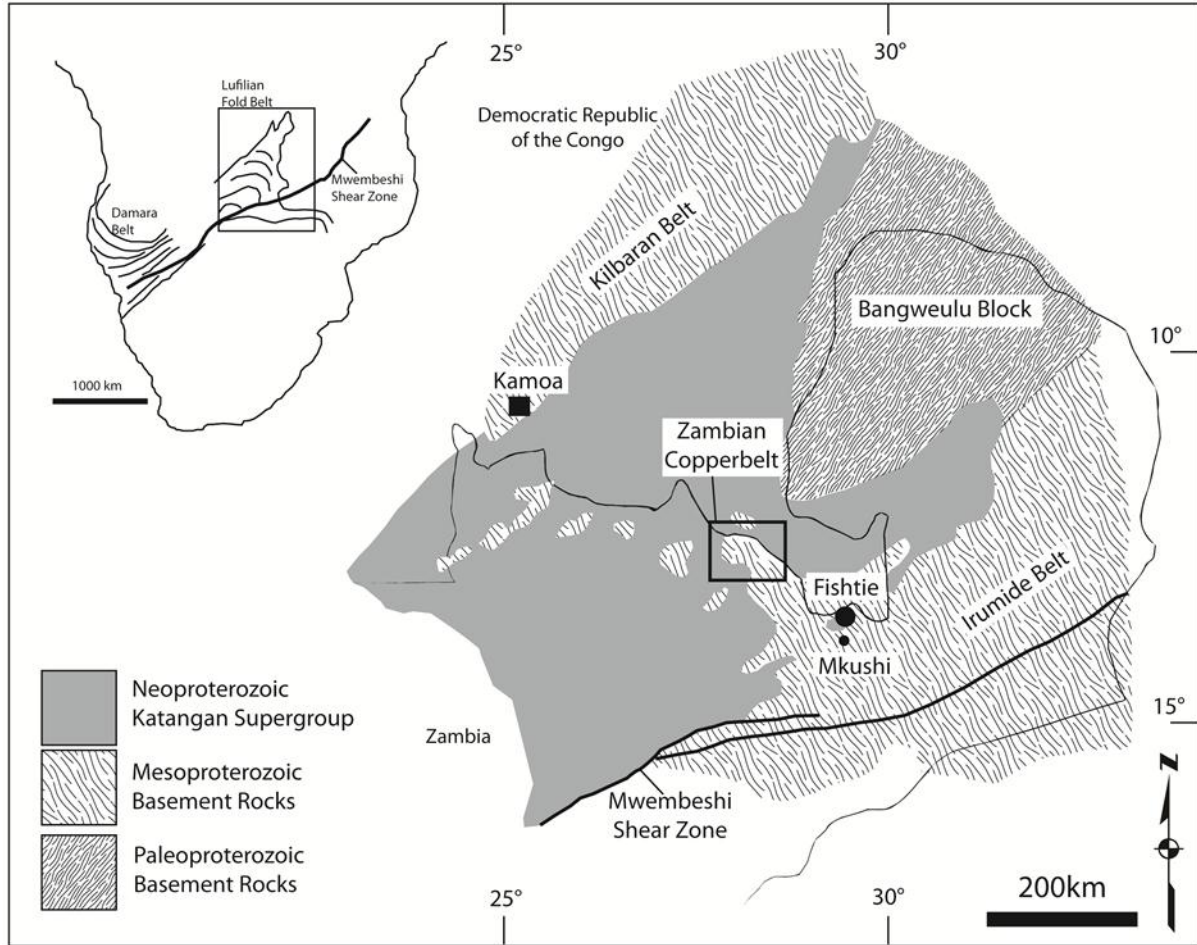


Figure 1.1: Generalized geologic map of the Central African Copperbelt area showing the distribution of rocks of the Katangan Supergroup. The Fishie copper deposit is hosted in the northeast corner of Lusale basin to the southeast of Zambian Copperbelt. The Fishie deposit is hosted in the same sequence as the giant Kamao deposit to the northwest along the western margin of the Katangan basin in the Democratic Republic of Congo. Modified from Selley et al. (2005).

Samples collected during logging were submitted for whole rock and trace element analysis (Appendix B). Additional samples were collected for petrographic and stable isotopic studies at the Colorado School of Mines. These samples were analyzed utilizing standard

transmitted and reflected light petrographic techniques and automated qualitative mineralogical analysis in order to delineate mineralogy and the paragenetic sequence of alteration and mineralization.

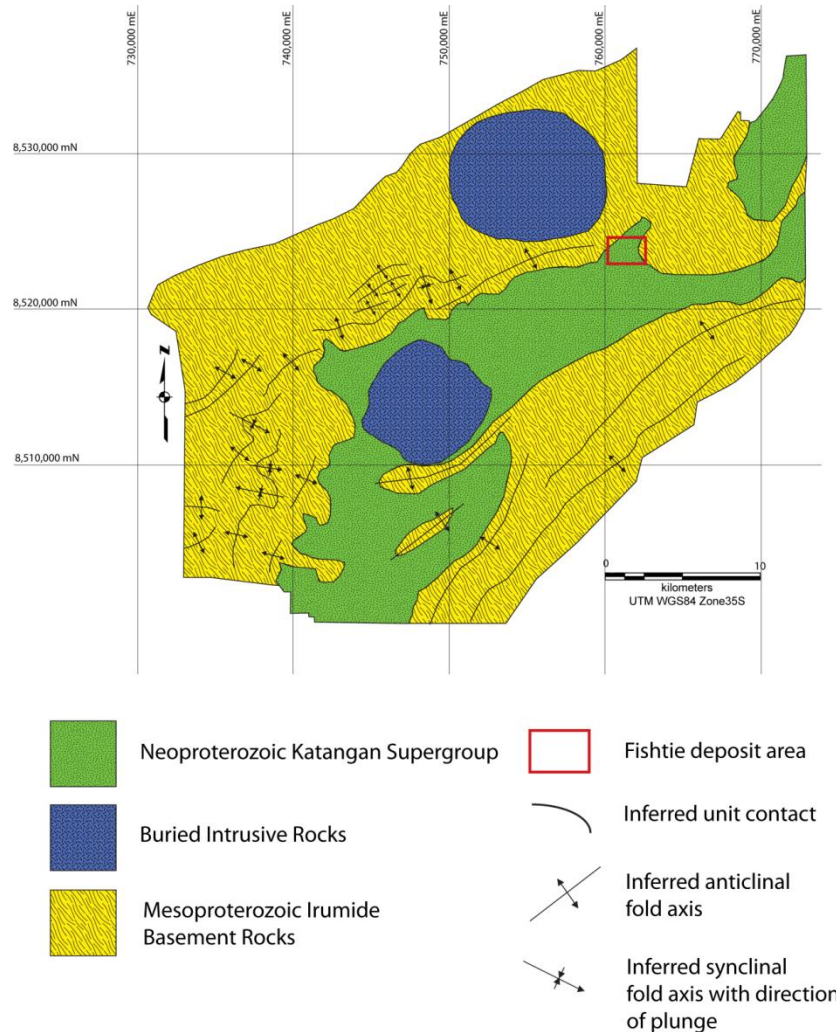


Figure 1.2: Generalized geologic map of the Lusale basin area compiled from aeromagnetic data gathered by First Quantum Ltd. and geological maps by the Geological Survey of Zambia (Stillman, 1965). The Fishtie deposit area is outlined in red. The Katangan Supergroup rocks to the northeast of Fishtie may have originally extended into the basin to the east of the Zambian Copperbelt (Figure 1.1). The two intrusions indicated on the map are inferred from the aeromagnetic data; neither appears to crop out at the surface. Structural trends in the basement rocks are derived from the Geological Survey of Zambia geological maps and modified with the aeromagnetic data.

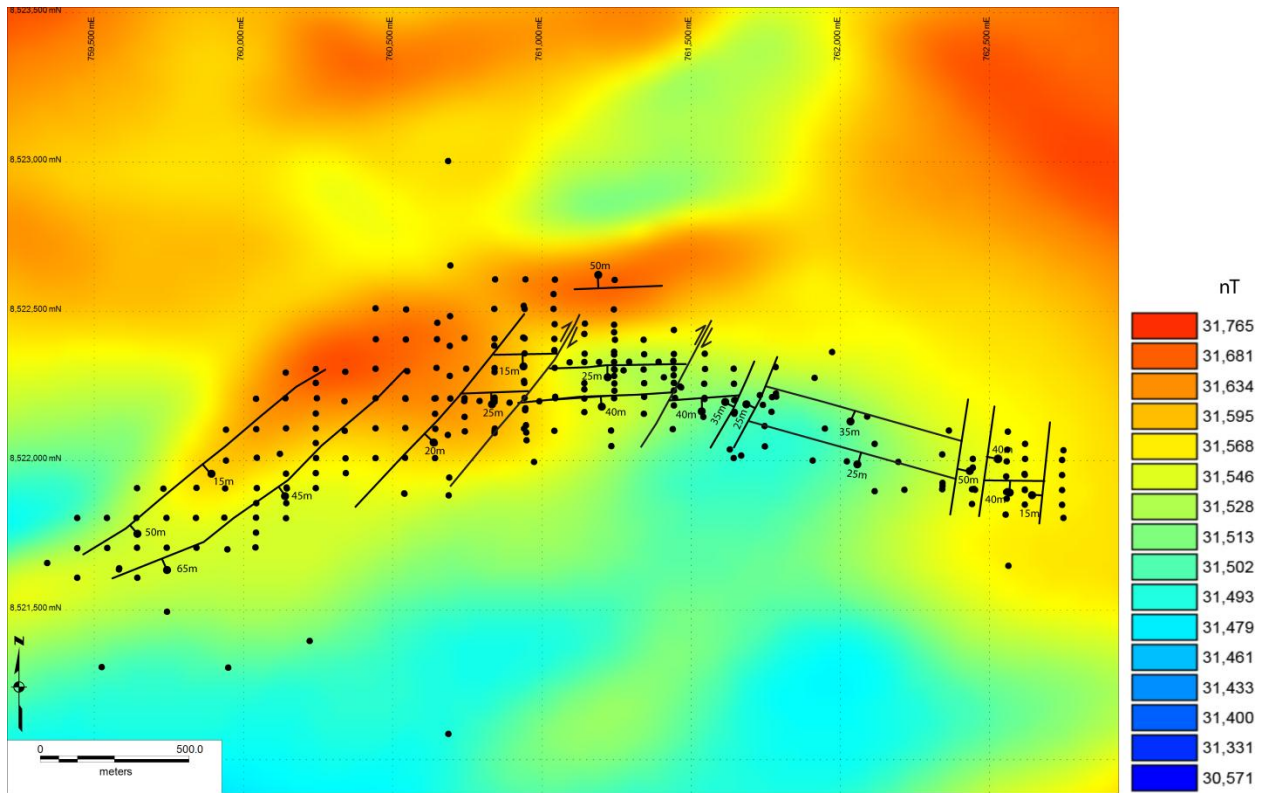


Figure 1.3: Location of drill holes at the Fishtie deposit. The drill holes are shown against reduced to pole magnetic data in nanoTeslas (nT); areas with higher values correspond to areas known to have a thinner veneer of Katangan metasedimentary rocks. The magnetic low to the north of the Fishtie deposit area represents an area with thicker Katangan metasedimentary rocks. The Fishtie deposit sits on a northeast trending magnetic high that probably represents a buried basement horst. The traces of faults in the area are derived from drill data are superimposed on the image and show that the deposit occurs along series of generally down to the south normal faults that form an arcuate array.

Qualitative mineral chemistry was accomplished with the QEMSCAN® instrument.

The QEMSCAN® instrument at the Colorado School of Mines is an automated quantitative mineralogy tool that utilizes a Carl Zeiss EVO50 SEM platform, four Bruker energy dispersive (EDS) detectors, and proprietary software to produce false-colored mineral maps from backscatter electron signals and EDS (energy dispersive spectrometer) spectra. A PC-based software suite, iDiscover™, allowed automated data acquisition and interactive data analysis. X-ray diffraction analysis of samples from the Fishtie deposit was not conducted to identify specific

clays minerals. All clays minerals are simply referred to as “clay(s)” for the purpose of this study.

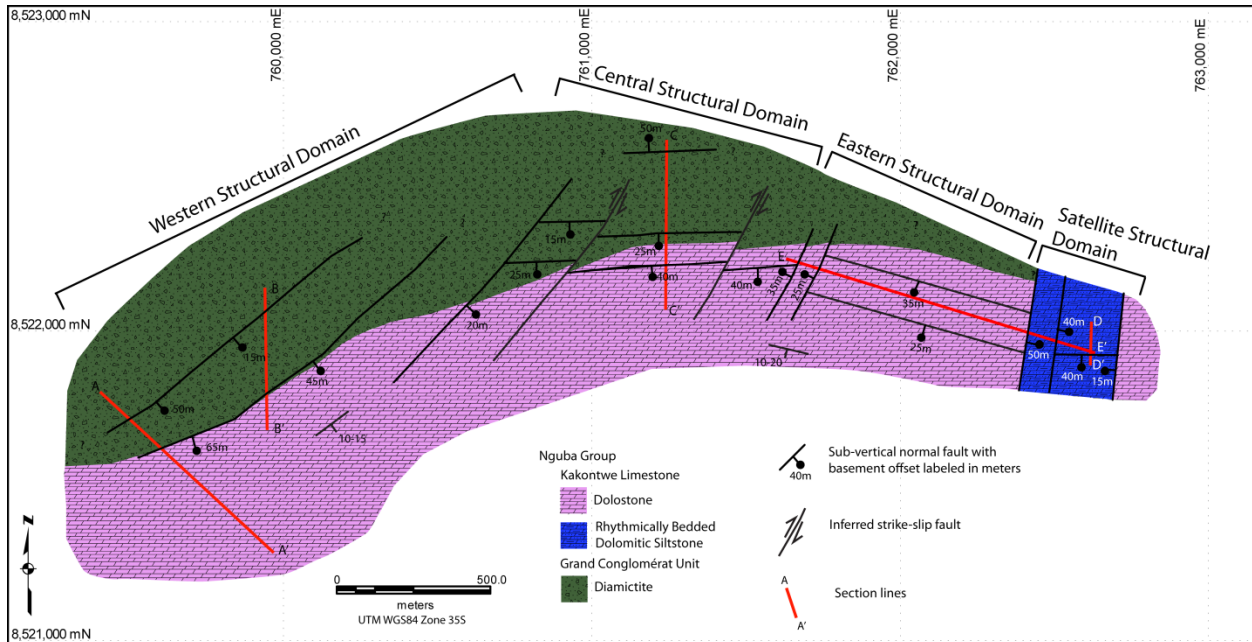


Figure 1.4: Generalized geologic map of the Fishtie copper deposit showing structural domains and location of cross section lines. Inferred near vertical normal faults define an arcuate pattern across the deposit area. More northerly trending dip-slip faults in the central structural domain appear to cut earlier generally east-trending normal faults and show offset in the center portion of the deposit indicating a component of strike-slip fault movement. Bedding strikes and dips in the Nguba Group Kakontwe Limestone unit were derived from maps produced by First Quantum Minerals Ltd.; beds strike parallel to the normal faults and dip shallowly to the southeast and southwest.

The Fishtie deposit is geologically significant because of its stratigraphic and structural setting. The deposit contains sulfides within the lower Nguba Group Grand Conglomérat unit. It is similar to the recently discovered, giant Kamao deposit in the Democratic Republic of Congo (DRC) (Schmandt et al., in press). Fishtie also contains mineralized zones in the lowermost portion of the stratigraphically overlying Kakontwe Limestone unit and is thus similar to the

Lonshi deposit to the north along the eastern edge of the Zambian Copperbelt (Hitzman et al., 2012).

The Grand Conglomérat unit at Fishtie directly overlies basement schists and quartzites and contains diamictites and siltstones as well as layers of magnetite-ankerite-apatite that have the appearance of a banded iron formation. These ironstones thicken toward synsedimentary normal faults and appear to represent a Rapitan-style of iron formation (Young, 1976; Klein and Beukes, 1993). This style of mineralization has not been previously described from the Katangan sequence in the Central African Copperbelt.

Sulfide mineralization post-dated formation of the ironstones in the Grand Conglomérat unit. Mineralization at Fishtie occurred along and adjacent to a series of generally east-west-trending normal faults. Sulfides in the Grand Conglomérat unit are mostly disseminated while sulfides in the Kakontwe Limestone unit occur as disseminated grains in carbonaceous beds and to a lesser degree occupy veins or form massive replacements. Much of the current copper reserves occur within weathered Kakontwe Limestone and consist of copper oxides; this style of supergene mineralized material was not investigated.

This study utilizes currently available data to present a detailed description of the stratigraphy and structure of the host rocks of the Fishtie deposit as well as the paragenetic sequence of diagenesis, iron formation, sulfide mineralization, and associated minerals. These data are then combined with information from stable isotopic studies to allow comparison with other, better known deposits in the Central African Copperbelt, particularly from the Kamoia deposit. The data derived from the study of the Fishtie deposit will allow for a better understanding of the geology and genesis of deposits throughout the Central African Copperbelt and will aid in future exploration throughout the district

## CHAPTER 2

### REGIONAL GEOLOGY

Ore hosting units at the Fishtie deposit overly rocks of the northeast-striking Mesoproterozoic Irumide belt that stretches from central Zambia to northern Malawi (De Waele et al., 2006). The Irumide belt is composed of a complexly deformed package of metamorphosed sedimentary, volcanic, and intrusive rocks. The portion of the Irumide belt underlying the Fishtie deposit is occupied by the Mkushi Gneiss Complex (Stillman, 1965) which is unconformably overlain by metasedimentary rocks of the Muva Supergroup that were deposited between ca. 1.85 and 1.65 Ga. The Muva Supergroup in this area is dominantly composed of quartzites and metapelitic rocks of the Manshya River, Kanona, and Mafingi groups (Dewaele et al., 2006). Though not observed in drill core, Irumide metamorphic rocks in the Lusale basin area appear to be cut by two major sub-circular intrusions seen on the aeromagnetic data (Figure 1.2; Appendix A); the inferred intrusion 2.5 km northwest of the Fishtie deposit is approximately 10 km in diameter and has a strong magnetic response, while the ~ 7 km in diameter intrusion in the center of Lusale basin has a comparatively weak magnetic signature.

Neoproterozoic metasedimentary rocks of the Katangan Supergroup with a maximum age of 880 Ma (Armstrong et al., 2005) unconformably overlie the Irumide metamorphic basement. These rocks host most copper deposits in the Central African Copperbelt and were deposited within a series of intracratonic basins developed on the Congo craton during the initial collision of the Congo continent with the Rodinian continent (Scotese, 2009) that eventually resulted in the break-up of Rodinia (Porada and Berhorst, 2000). These basins may have been of impactogen-type (Sengor et al., 1978). Preserved portions of Katangan Supergroup in the

Zambian Copperbelt form a sequence of rocks varying in thickness from ~1-3 Km, with a pre-erosional thickness estimated between 5 and 7 km (Annels, 1989; Woodhead, 2013).

In the Zambian Copperbelt the Katangan Supergroup has been subdivided into the Roan, Nguba, and Kundelungu groups (Cailteux et al., 2005; Selley et al., 2005). Copper deposits in the Zambian Copperbelt are hosted primarily in the Lower Roan Subgroup (Figure 2.1). The lowermost Mindola Clastics Formation contains laterally discontinuous sandstones and conglomerates. These are abruptly overlain in the western Zambian Copperbelt by a regionally extensive variably organic-rich marginal marine siltstone/shale termed the Copperbelt Orebody Member, colloquially known as the “Ore Shale”, that forms the basal unit of the Kitwe Formation. The Kitwe Formation is composed of interbedded siliciclastic and carbonate rocks and hosts the majority of ore deposits in the Zambian Copperbelt. In the eastern portion of the Zambian Copperbelt to the north of Fishtie, the Kitwe Formation contains dominantly siliciclastic sedimentary rocks. Throughout the Zambian Copperbelt the Kitwe Formation passes upwards into laterally extensive shallow marine carbonates and generally finer grained siliciclastic rocks with abundant evaporitic textures and mainly stratabound breccias (Woodhead, 2013). The overlying Mwashya Subgroup comprises mainly deeper water carbonaceous shales, siltstones, and clastic carbonate rocks (Cailteux et al., 2007; Bull et al., 2011). The Mwashya Subgroup in the Zambian Copperbelt contains a number of gabbroic intrusions. Compositionally similar mafic intrusions and extrusive units occur with the Mwashya Subgroup and lowermost Nguba Group rocks throughout the Central African Copperbelt and have ages ranging from 765 to 735 Ma (Key et al., 2001; Barron, 2003).

Roan Group rocks are absent at Fishtie where the basal unit of the Nguba Group, the Grand Conglomérat unit, directly overlies basement rocks (Figure 2.1). The Grand Conglomérat

is relatively thin and commonly mildly carbonaceous in the **Zambian Copperbelt** (Binda and Van Eden, 1972). At **Fishtie** the **Grand Conglomérat** unit comprises a <150m thick sequence of debris flows and diamictites that contains lenses of laminated siltstone and lithic sandstone.

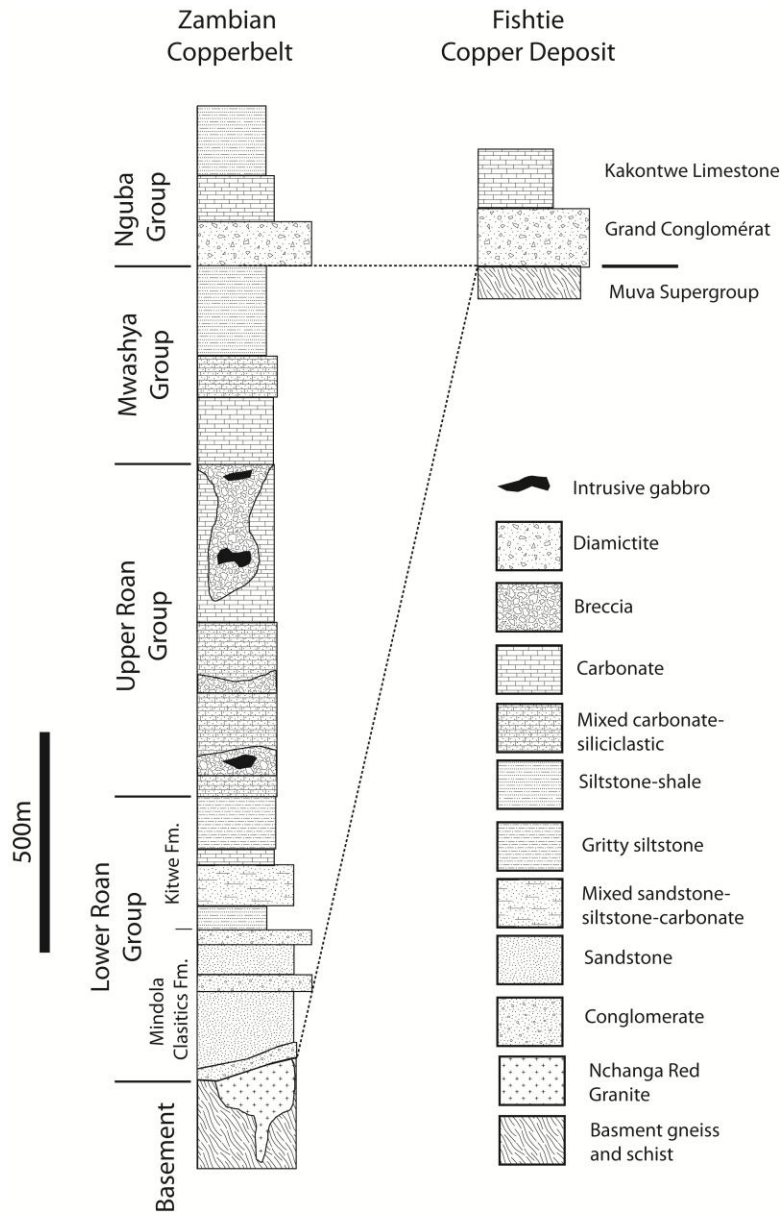


Figure 2.1: Generalized stratigraphy of both the Zambian Copperbelt and Fishtie copper deposit. Nguba Group rocks directly overlie basement rocks that form the footwall to the Fishtie deposit. Diamictite and carbonate successions at Fishtie are relatively thin, but are slightly thicker than those observed in the Zambian Copperbelt. Modified from Selley et al. (2005).

The Grand Conglomérat unit is believed to be correlative with glacial diamictites of Sturtian age. The precise age of the Sturtian glacial event is debated with most evidence pointing to a range between ~700 and ~725 Ma, though an age of ~740 Ma has also been proposed (Key et al., 2001; Bodiselitsch et al., 2005; Bowring et al., 2007; Smith, 2009; Xu, 2009; McDonald et al., 2010). It is overlain by massive carbonate rocks (Kakontwe Limestone; Cailteux et al., 2007) or carbonate-bearing to carbonate-poor siltstones and sandstones. Though not present in the Fishtie area, Nguba Group rocks above the Kakontwe Limestone consist of dolomitic sandstones and siltstones to the north in the DRC (Batumike et al., 2006, 2007).

Three significant tectonic events affected the Zambian Copperbelt. Extension associated with early rifting (post-880 Ma) formed isolated fault-controlled basins, which linked along master faults during deposition of the Copperbelt Orebody Formation (Selley et al., 2005). A second period of extension occurred during deposition of the upper portion of the Mwashya Subgroup through to deposition of the lower Nguba Group (~765–720 Ma); this rifting event was associated with mafic magmatism. Both these extensional events appear to be linked to collision between the Congo and Rodinia continents (Scotese, 2009). The Lusale basin appears to have been formed during the Mwashya extensional event. Basin inversion and later compressive deformation (~590–500 Ma) culminated in greenschist-grade metamorphism (~530 Ma) during the Lufilian event. The Lufilian event is part of a broad Pan-African orogenic event (Scotese, 2009). Allochthonous salt tectonism that probably began during Nguba Group time (Hitzman et al., 2012) continued into the Lufilian event; halokinesis has been suggested to account for the complex macro scale geometry of the Lufilian arc (de Magnée and François 1988, Kampunzu and Cailteux 1999; Jackson et al., 2003; Hitzman et al., 2012).

Geochronology of metamorphic rocks indicates the Lufilian event was a protracted orogenic event spanning ~100 m.y. U-Pb dating of monazite and Ar-Ar dating of biotite in greenschist facies rocks of the Zambian Copperbelt yield metamorphic ages of between 585 and 592 Ma (Rainaud et al., 2002). Hanson et al. (1993) estimated the main phase of metamorphism to have occurred at ~560-530 Ma based on U-Pb zircon dating of syn to post metamorphic rhyolites and granites in central Zambia. Peak metamorphism is estimated to have occurred at ~530 Ma as indicated by U-Pb ages of monazite in metamorphic rocks in northwestern Zambia (John et al., 2004).

## CHAPTER 3

### STRATIGRAPHY AND LITHOLOGY OF THE FISHTIE COPPER DEPOSIT

Basement rocks that form the footwall to the Fishtie deposit are composed of quartz-muscovite schists and quartzites (Figure 3.1a, b). Reports and maps published by the Zambia Geologic Survey indicate the Fishtie area is underlain by muscovite-kyanite-sillimanite, quartz-muscovite, biotite, and garnet-biotite schists, quartzites, and phyllites (Stillman, 1965). Based on the stratigraphic terminology proposed by Dewaele et al. (2006), Fishtie overlies rocks of the Mafingi or Manshya River groups of the Muva Supergroup. The Grand Conglomérat unit of the Nguba Group directly overlies basement rocks. At Fishtie the Grand Conglomérat unit consists dominantly of matrix supported diamictites (Figure 3.1c) with subsidiary siltstone units (Figure 3.1d) that are sometimes mineralized to magnetite-ankerite-apatite iron formation (Figure 3.1e). The Kakontwe Limestone unit overlies the Grand Conglomérat unit and is composed of massive limestone (Figure 3.1f), massive to finely bedded or algally laminated dolostone, and rhythmically bedded dolomitic siltstone (Figure 3.1g).

The Fishtie deposit area has virtually no outcrop. The area is covered by overburden composed of soil, residual weathered carbonate, and saprolite. Thicker residual soil and saprolite was developed above the Kakontwe Limestone unit than the Grand Conglomérat unit. Lithologies at Fishtie are described utilizing drill holes from the periphery of the deposit where the effects of hydrothermal alteration associated with iron oxide and sulfide precipitation are least obvious.

Cross sections through the deposit were created from detailed core logs by the author and company core logging databases (Figure 3.2). The author logged two holes in section B-B' (DDHs KEDD0033, 0034), six holes in section C-C' (DDHs KEDD0006, 008, 0012, 0063,

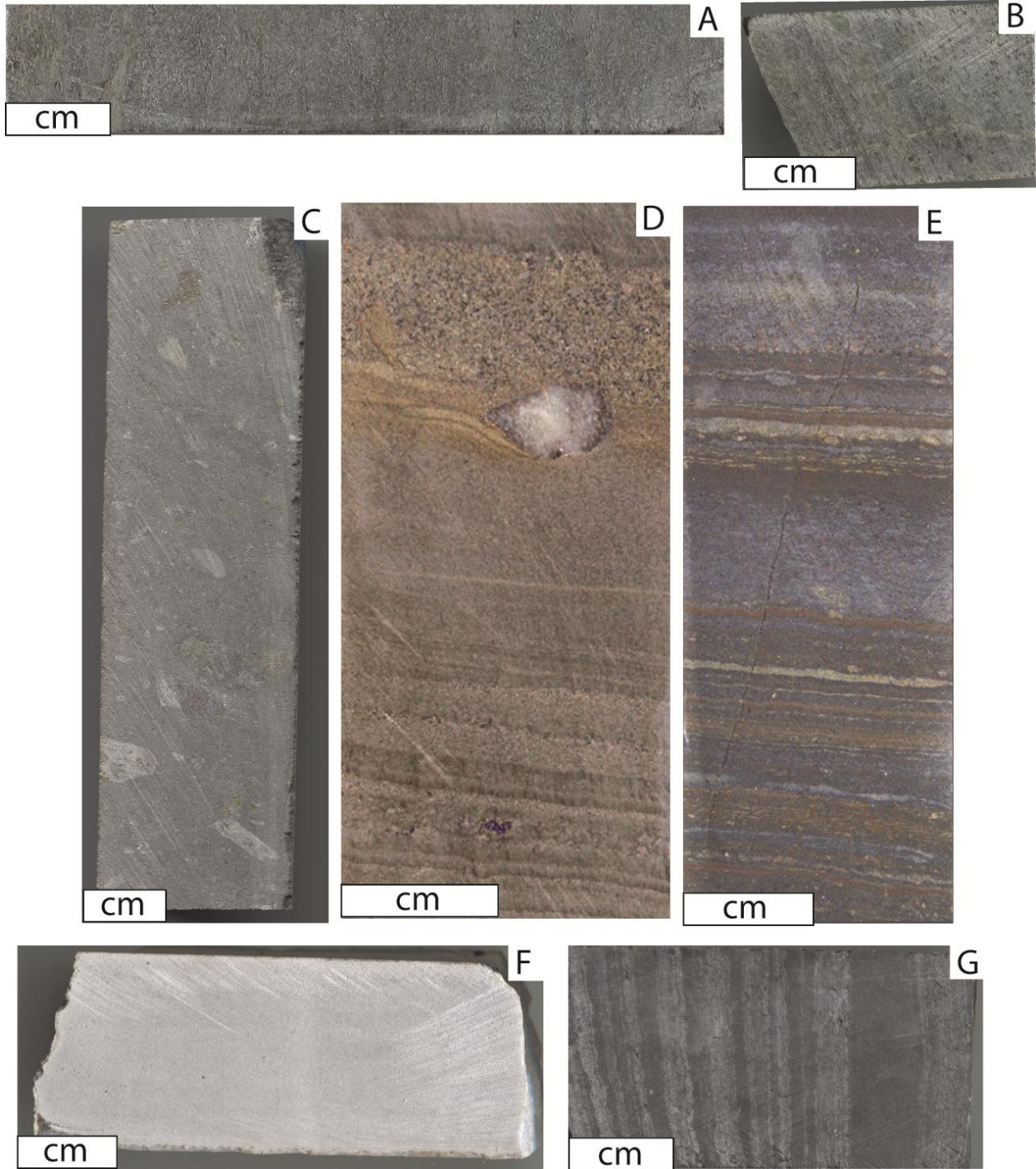
0064, 0089), and four holes in section D-D' (DDHs KEDD0085, 0134A, 0135, 0142). Sections A-A' and E-E' were constructed solely from company drill hole logs.

### **3.1 Basement Rocks**

Drilling at Fishtie has intercepted a maximum of 40 meters of the basement rocks. The basement is composed of interlayered schist and quartzite with individual lithologic layers ranging in thickness from 5 to 20 meters. The rocks display a prominent foliation. The foliation is generally at a low angle to bedding, where it is preserved in quartzite layers (Stillman, 1965).

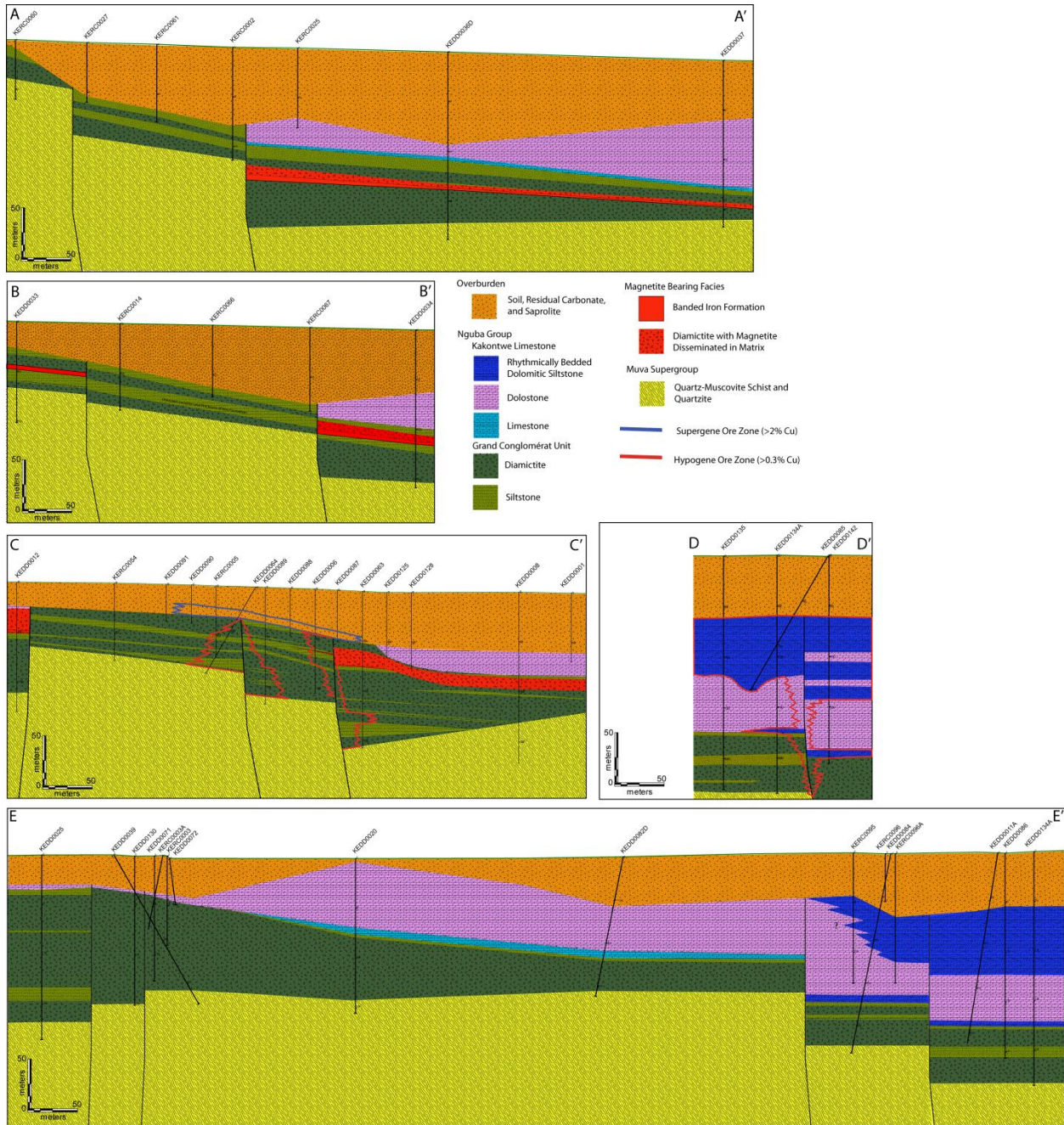
Schists contain dominantly muscovite and quartz with subordinate chlorite, biotite and dolomite. Muscovite occurs as euhedral laths up to several millimeters in length that define a distinct foliation (Figure 3.3a). While not observed at Fishtie, the schists have locally been noted to contain at least two foliations regionally with early kyanite rotated into a later foliation (Stillman, 1965). Fine-grained aggregates of white mica (“sericite”) commonly rim larger muscovite grains. Quartz occurs as subhedral grains up to 2 mm in diameter that define an inequigranular, interlobate texture. Quartz grains may be mantled and sometime cut by both fine- and coarse-grained muscovite. Potassium feldspar is subordinate to quartz and occurs as subhedral grains up to 200 microns in diameter. The potassium feldspar is typically altered to muscovite or fine-grained white mica. Plagioclase was not observed in samples of the basement schists examined for this study. A general absence of plagioclase in basement rocks of the area was also noted by Stillman (1965). Biotite occurs sporadically as anhedral crystals up to 100 microns in diameter that are intergrown with muscovite and commonly overgrown or replaced by chlorite. Dolomite occurs as irregular patches that are overgrown or embayed by muscovite, fine-grained white mica, chlorite, and biotite. Large (750+  $\mu\text{m}$ ) fans of chlorite rim and locally replace dolomite grains; some of these chlorite grains are partially replaced by white mica.

Figure 3.1: Hand sample photographs of the major rock units at the Fishtie copper deposit. (A) Typical quartz-muscovite basement schist from the central structural domain (DDH KEDD008, 133.2m). (B) Basement quartzite from the western structural domain displaying banding that probably represents relict bedding. The rock is composed dominantly of quartz with darker bands and nodules composed of biotite (DDH KEDD0034, 158m). (C) Clast-poor Grand Conglomérat diamictite from the central structural domain with subrounded to subangular clasts of quartzite and lesser carbonate in a grey matrix. This matrix color is diagnostic of muscovite mineralization (DDH KEDD0063, 125.9m). (D) Siltstone within the Grand Conglomérat unit containing a dropstone of vein quartz that deforms underlying beds. The siltstones have been pervasively mineralized by ankerite, probably during formation of the iron formation, and contain minor disseminated magnetite. Coarser grained siltstone layers contain disseminated bornite, some of which is intergrown with quartz. The dropstone has a discontinuous rim of bornite and chlorite (DDH KEDD0018, 103m). (E) Iron formation within the Grand Conglomérat unit. The iron formation consists of dark bands of magnetite-quartz, brown bands consisting of ankerite, magnetite, and quartz, and pale apatite-rich bands. Grey bands are weakly altered but do contain disseminated magnetite. The sample contains several small pebbles of ankerite- and apatite-rich material that could be rip-up clasts of iron formation beds or replacements of lonestone clasts (KEDD-0032, 78.9m). (F) Pale massive dolostone in the Kakontwe Limestone unit from the eastern structural domain displaying very faint algal banding (DDH KEDD0079, 74m). (G) Rhythmically bedded dolomitic siltstone from the Kakontwe Limestone unit from the satellite structural domain that generally overlies massive carbonate rocks at the base of the unit (DDH KEDD0142, 139.5m).



Chlorite also occurs as small to moderate sized crystals intergrown with and replacing fine-grained white mica. Biotite and chlorite are sometimes intergrown and concordant with the foliation defined by white mica. Chlorite also replaces biotite.

Figure 3.2: Cross sections through the western, central, satellite, and eastern structural domains of the Fishtie copper deposit. Sections A-A', B-B', C-C', and D-D' are oriented roughly N-S, and section E-E' is a long section across the eastern structural domain that is oriented roughly E-W. Nguba Group diamictite sharply overlies basement quartzites and quartz-muscovite schist. Thickening of Grand Conglomérat unit diamictite packages towards several of the high angle normal faults indicates synsedimentary subsidence. The hypogene ore zones are highest grade in the Grand Conglomérat unit near inferred high angle normal faults in section C-C' and within Kakontwe Limestone unit dolomitic siltstones in section D-D'. Hypogene copper mineralized zones are not well developed in section A-A', B-B', and E-E'. KEDD denotes diamond drill hole and KERC denotes reverse circulation drill hole.



Quartzite layers are composed of 10 to 2000 $\mu$ m diameter, sub- to anhedral, undulose quartz grains that display an intragranular seriate texture and show sub-grain rotation and grain boundary migration (Figure 3.3b). Intergrown muscovite, biotite, and chlorite occur interstitial to

quartz grains. Tourmaline is present as small (<15 micron) pleochroic (green) euhedral crystals. The quartzite layers locally display large-scale (up to 0.5 m) relict cross-bedding textures.

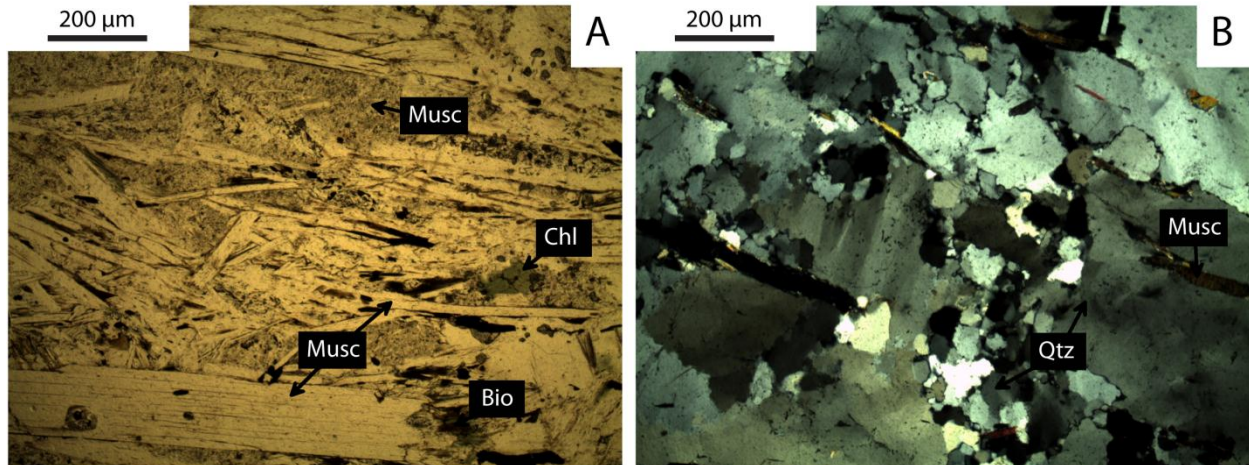


Figure 3.3: Basement schist and quartzite. (A) Photomicrograph of muscovite-rich basement schist from the eastern structural domain. Large, euhedral muscovite laths define the foliation and are partially altered to sericite (DDH KEDD0076, 142.8m). (B) Cross-polarized photomicrograph of basement quartzite from the western structural domain. Quartz crystals define an inequigranular texture. Most quartz displays an undulose texture. Grain boundary granulation is common (KEDD0076 176.8m).

### 3.2 Nguba Group - Grand Conglomérat Unit

The Grand Conglomérat unit of the lowermost Nguba Group ranges in thickness from ~20 to 150 meters at Fishtie and contains both diamictites and siltstones. Drilling indicates that the unit is thickest adjacent to inferred high-angle normal faults (Figure 3.2) suggesting accommodation space was tectonically generated during sedimentation. Diamictite beds in the Grand Conglomérat unit are commonly massive; individual beds range from 5 to 30 meters in thickness. Diamictite beds do not display grading and are matrix supported with clasts comprising 15-30% of the rock (Figure 3.1c); diamictite beds near the base of the unit tend to have more abundant clasts than those near the top of the unit. Clasts do not display sorting or have a preferred orientation. They are typically subangular to subrounded and range in size from

<1mm to greater than 2 meters in diameter; apparently faceted clasts are present. The majority of clasts are quartzite, muscovite-quartz schist, or vein quartz. A lesser number of dolostone, limestone, and albitized and/or chloritized mafic igneous rock clasts are also present. While the quartzite, schist, vein quartz, and mafic igneous clasts could be derived from the basement sequence beneath the Grand Conglomérat unit, the carbonate clasts do not appear to have a local basement source.

Clasts in the diamictite display discontinuous or less commonly complete rims of coarse-grained minerals. Rims are sometimes developed at opposite ends of clasts and have the appearance of pressure shadows (Figure 3.4a); this texture of bipolar clots of coarse minerals growing on clasts is reminiscent of the textures at the Kamoia deposit (Schmandt et al., in press). Such rims are thickest and most abundant within and proximal to the ore zone. Rims commonly contain chlorite, biotite, potassium feldspar, ankerite, quartz, and copper sulfides. The mineralogy of the coarse-grained rims mirrors the fine-grained alteration mineral assemblages in the diamictite matrix except that the rims rarely contain muscovite (Figure 3.4b, c). The mineral assemblage in these rims does not change vertically throughout the stratigraphic sequence as at the Kamoia deposit (Schmandt et al., in press). There may be a lateral change in rim mineral assemblages at Fishtie moving out from normal faults though this could not be convincingly demonstrated with the available drilling data.

The dark blue-grey to grey-green colored matrix of the diamictite at Fishtie was originally composed of fine-grained detrital quartz, feldspar, clay and carbonate minerals (Binda and Van Eden, 1972). During diagenesis and hydrothermal fluid infiltration, clay in the matrix was likely converted to potassium feldspar, muscovite, biotite, or chlorite and detrital plagioclase feldspar was largely replaced by albite and potassium feldspar.

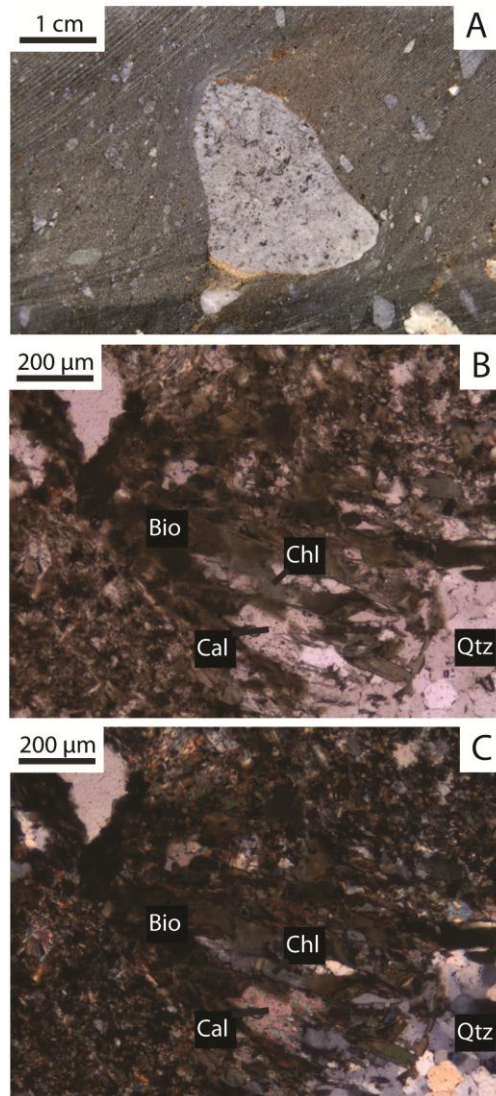


Figure 3.4: Grand Conglomérat unit. (A) Intrusive basement clast within the Grand Conglomérat unit diamictite. The clast displays a discontinuous rim of tan colored ankerite and biotite. Ankerite occurs in the matrix of the diamictite to the upper right of the clast (KEDD0029, 42.3m). (B) Plane-polarized photomicrograph of a coarse-grained mineral rim on the edge of a quartzite clast (pressure shadow) composed of biotite, chlorite, and lesser calcite. The coarse-grained clast mineralogy mirrors fine grained alteration mineralogy in matrix (DDH KEDD0008, 98.6m). (C) Cross polarized photomicrograph of (B) (DDH KEDD0008, 98.6m).

The matrix of the diamictite is fine grained with individual grains ranging in size from 2.5 to 20  $\mu\text{m}$  in diameter (Figure 3.5a). Away from iron oxide or sulfide mineralized zones the matrix of the diamictites is composed of quartz, albite, potassium feldspar, white mica, and

carbonate minerals with lesser chlorite, biotite, and heavy minerals (tourmaline, apatite, and rutile). Pyrite occurs sporadically throughout the matrix as small anhedral grains.

The diamictite matrix contains approximately 20% apparently detrital grains of quartz, potassium feldspar, and muscovite. Quartz is the most common detrital mineral. Individual grains are subrounded to angular in shape and range from 10 to 300  $\mu\text{m}$  in diameter. The irregular shape of many quartz grains is partially due to irregular quartz overgrowths that were later etched and partially dissolved. Many quartz grains, including those with authigenic quartz rims, are rimmed by a thin coating of potassium feldspar and/or muscovite (Figure 3.5b). Albite occurs as generally small subangular to subrounded grains; no remnant detrital plagioclase has been observed at Fishtie. Albite grains are locally altered to an assemblage of muscovite, biotite, and chlorite. Potassium feldspar also occurs as small subrounded to subangular grains that are detrital or represent replaced detrital plagioclase. Muscovite occasionally occurs as detrital grains up to 500  $\mu\text{m}$  in length. Grains of originally detrital dolomite are commonly replaced by ankerite, and are also present in many samples (Figure 3.5b).

The finest-grained portion of the diamictite matrix is composed of quartz, white mica, biotite, chlorite, potassium feldspar, and dolomite-ankerite, with lesser rutile and apatite (3.5c). White mica is the most common phyllosilicate. Fine-grained white mica occurs throughout the matrix but is particularly common adjacent to potassium feldspar grains suggesting that it was formed by replacement of the potassium feldspar. Biotite grains in diamictite matrix range from 10 to 40  $\mu\text{m}$  in length. Biotite is commonly intergrown with chlorite. Rutile is a very minor constituent of the diamictite matrix and occurs as small (50  $\mu\text{m}$  in diameter) subhedral crystals.

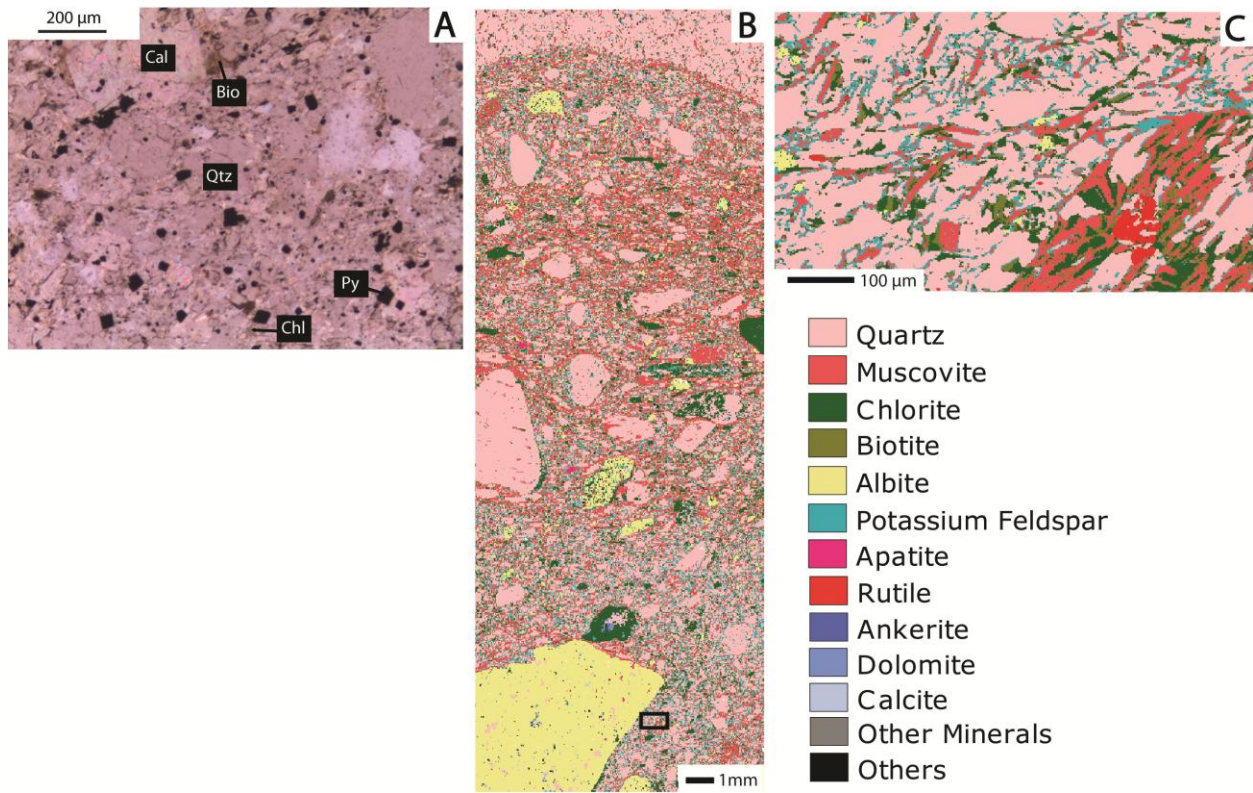
The matrix of the diamictites at Fishtie may display a weakly developed, steeply dipping foliation, especially adjacent to the generally east-west-striking normal faults in the deposit area.

This foliation is most pronounced adjacent to lithic clasts. The foliation is defined by the vertical alignment of muscovite, chlorite, biotite, and sometimes dolomite. This foliation is somewhat similar to that observed in the lower portion of the diamictite sequence at the Kamoia deposit where it has been interpreted to represent a fluid dewatering texture that was formed during diagenesis and hydrothermal alteration (Schmandt et al., in press).

Siltstones within the Grand Conglomérat unit occur as 0.1-10 meter thick intervals within the diamictites. Individual beds within siltstone packages range up to 5 mm thick. The beds commonly display grading. The siltstones contain lonestones up to several centimeters in diameter which indent underlying beds and are draped by overlying beds (Fig 3.6). These clasts have the appearance of dropstones and provide good evidence for glacial influence during sedimentation.

The siltstone beds are composed of fine-grained quartz, potassium feldspar, white mica, biotite, chlorite, and carbonate minerals (Figure 3.7a, b, c, d). Coarser beds have abundant detrital quartz and feldspar (now all potassium feldspar) grains. They occur as both subrounded grains (50 to 200  $\mu\text{m}$  in diameter) that define a roughly equigranular texture and smaller, anhedral grains. Coarser grained beds are commonly cemented by carbonate minerals (calcite, dolomite, and ankerite) that form anhedral grains 20-60  $\mu\text{m}$  in diameter. Rutile is present as small (10-20  $\mu\text{m}$ ) sub- to anhedral grains in many coarser grained beds. Pyrite is a minor constituent of the coarser grained siltstone beds and is rarely present in amounts greater than 1 percent. The pyrite occurs as relatively large (up to 500  $\mu\text{m}$ ) sub-spherical crystals that form aggregates (Figure 3.7c, d). The shape of these pyrite grains suggests they represent diagenetic framboids.

Figure 3.5: Grand Conglomérat diamictite. (A) Plane-polarized photomicrograph of relatively weakly altered diamictite. Phyllosilicates are weakly developed and a primary detrital matrix of subround quartz grains is well preserved. Calcite is abundant and likely represents carbonate cementation that occurred during diagenesis as well as possibly detrital grains. Minor pyrite is present as cubic crystals (DDH KEDD0034, 108m). (B) QEMSCAN® image at a 15 micron resolution of diamictite displaying weak potassium feldspar and muscovite mineralization of the matrix. This sample contains clasts of quartz as well as several albite-rich and chlorite-rich clasts in a matrix of muscovite, biotite, and potassium feldspar. The clasts are dominantly subrounded to less common subangular quartz. The clast at the top of the image is quartzite with quartz grains in a quartz, biotite, and muscovite matrix. The sample also contains several subrounded to subangular clasts composed dominantly of albite containing fine grains of chlorite that were likely detrital plagioclase feldspar grains. Other generally elongate clasts are dominantly composed of chlorite. These were likely mafic igneous clasts. The central portion of the sample has a muscovite-rich matrix while the matrix above and below this is more potassium feldspar rich. Muscovite commonly replaces potassium feldspar. The matrix also contains relatively minor biotite that is locally replaced by chlorite. Several of the quartz clasts display discontinuous rims of chlorite and less commonly muscovite; the muscovite appears paragenetically early relative to chlorite. Carbonate minerals are rare in this sample. Minor calcite is present within some quartz clasts and as rare small grains in the matrix. The black box shows the location of image (C) (DDH KEDD0076, 174m). (C) High resolution (2 micron) QEMSCAN® image of the least altered diamictite matrix in (B). The sample contains subrounded to subangular, commonly somewhat elongate quartz grains with interstitial potassium feldspar, muscovite, biotite, and chlorite. The muscovite forms flakes up to approximately 100 microns in length. Potassium feldspar cements quartz grains, most likely as an alteration product from original detrital clay. Muscovite replaces potassium feldspar. Irregular grains of biotite are intergrown with both potassium feldspar and muscovite. Biotite crystals are partially replaced by chlorite throughout the sample. Several anhedral grains of albite, probably after detrital plagioclase, are present. The sample also displays an aggregate of rutile crystals (DDH KEDD0076, 174m).



Finer grained beds within the siltstone layers tend to be richer in phyllosilicate minerals than coarser grained beds. The fine-grained beds are composed dominantly of white mica with subsidiary biotite, chlorite, quartz, and potassium feldspar (Figure 3.7a, b). Fine-grained white mica forms small subhedral crystals or aggregates of crystals interstitial to quartz, potassium feldspar, and carbonate minerals. Chlorite and biotite commonly occur together as small subhedral grains. Chlorite occurs as subhedral crystals that are rimmed or overgrown by biotite. Rare apatite occurs as small (10-30  $\mu\text{m}$ ) rounded to angular grains.

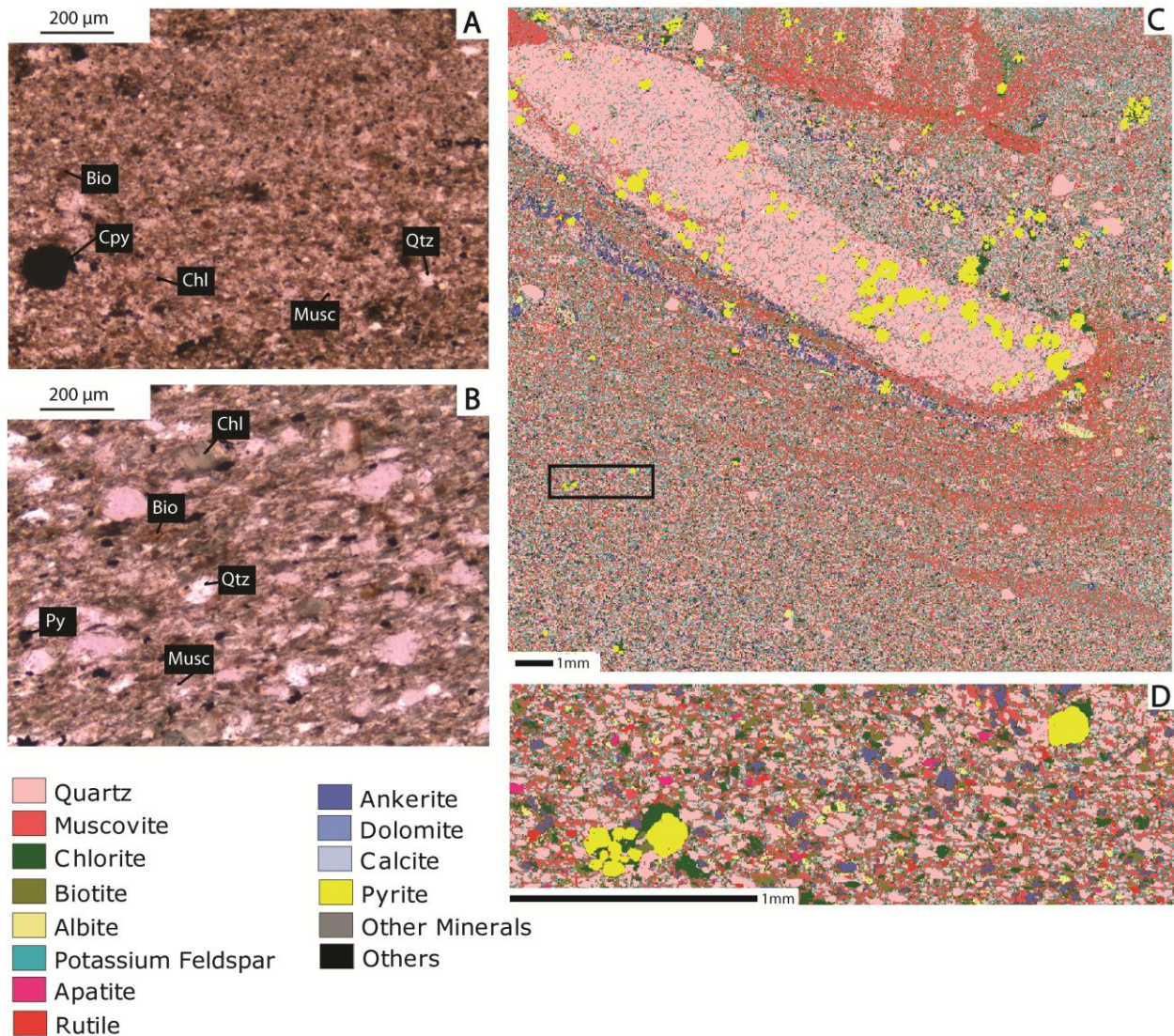
The Grand Conglomérat unit diamictites at Fishtie are dominantly high-energy mass-flow deposits that contain clasts derived from both the adjacent basement uplifts and more distal Roan Group outcrops. They are also likely to contain glacial dropstones. The diamictites are interbedded with silty turbidity current deposits that contain glacial dropstones. The presence of

exotic clasts, striated clasts, and dropstones clearly demonstrates the sequence is partially glaciogenic in origin (Cahen, 1978).



Figure 3.6: Lonestone of quartzite within magnetite- and ankerite-rich siltstone (weakly developed iron formation) from within the Grand Conglomérat unit. The clast deforms underlying beds. The texture suggests this is a dropstone deposited from melting ice (DDH KEDD-0034, 113.5m).

Figure 3.7: Grand Conglomérat unit siltstones. (A) Plane-polarized photomicrograph of a fine-grained siltstone from the eastern structural domain. The rock consists of quartz, muscovite, biotite, and chlorite. The sample is mineralized and contains chalcopyrite grains (opaque) up to 100 microns in diameter (KEDD0023, 102.7m). (B) Plane-polarized photomicrograph of a relatively coarse grained siltstone bed from the central structural domain. The sample contains detrital clasts of quartz in a matrix of fine-grained muscovite, biotite, and chlorite (DDH KEDD0008, 104m). (C) QEMSCAN® image utilizing a 15 micron resolution, of siltstone underlying a diamictite layer from a weakly altered portion of the deposit in the eastern structural domain. The matrix of the diamictite contains subrounded to subangular grains of detrital quartz up to 0.6 mm in diameter set in a matrix of quartz, potassium feldspar, muscovite, biotite, and chlorite. A quartzite clast dominates the central part of the sample. The clast is composed of subrounded quartz grains surrounded by potassium feldspar and a containing muscovite-rich band. A clast of biotite-quartz-muscovite schist is present at the top of the image. Biotite in this clast is partially replaced by chlorite. Both clasts and portions of the matrix of the rock have been overgrown by rounded grains of pyrite up to 0.5 mm in diameter. Many of these pyrite grains are intergrown with or overgrown by chlorite. Both the quartzite and schist clasts display rims of muscovite. The muscovite rim on the quartzite clast is discontinuous. It is best developed beneath and on both ends of the clast. The muscovite rim beneath the clast has an outer rim of ankerite. These rims were probably formed during hydrothermal mineralization. The siltstone below the diamictite contains a similar mineral assemblage to the diamictite but grain sizes are smaller. Wispy muscovite-rich bands through the matrix likely represent relict clay-rich seams. The area of image (D) is outlined in black (DDH KEDD0076, 168m). (D) QEMSCAN® image utilizing a 2 micron resolution, of the siltstone in (C). The siltstone is composed of detrital grains of quartz, feldspar, and carbonate grains in a matrix of muscovite and biotite. The quartz grains display irregular shapes suggesting many have authigenic overgrowths that underwent quartz dissolution. The only plagioclase feldspar present is albite that displays irregular edges and commonly contains minor amounts of chlorite. The carbonate grains show subrounded to irregular shapes suggestive of derivation from sedimentary grains. They consist almost entirely of ankerite suggesting hydrothermal alteration of the sample. Several of the ankerite grains are rimmed or cut by potassium feldspar. Muscovite in the sample forms small flakes to irregular clots. Biotite is present as irregular to somewhat elongate grains. Chlorite is sometimes intergrown with or replaces biotite and also occurs as discrete grains. The matrix also contains a number of apatite and rutile grains that display subrounded to irregular shapes. The sample contains several grains of subrounded to subhedral pyrite that is commonly intergrown with or overgrown chlorite (DDH KEDD0076, 168m).



Thickening of the Grand Conglomérat unit toward normal faults indicates deposition in actively growing grabens. The rapid thickness changes displayed by the Grand Conglomérat unit at Fishtie are similar to those described from the Itawa area to the north along the eastern edge of the Zambian Copperbelt (Binda and Van Eden, 1972). The Grand Conglomérat unit at Fishtie is similar to other described sequences of this unit along the southern margin of the Katangan basin (Master and Wendorff, 2011).

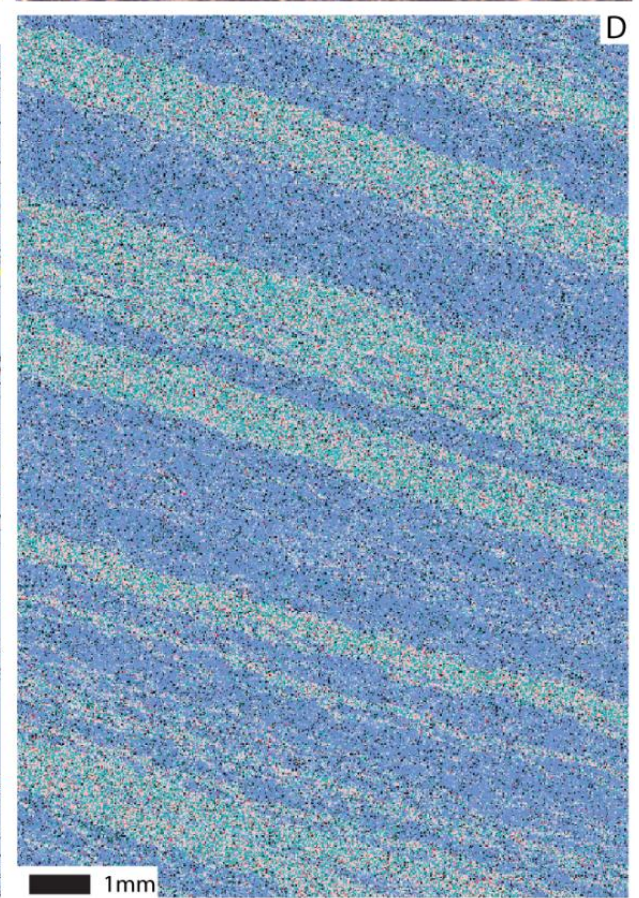
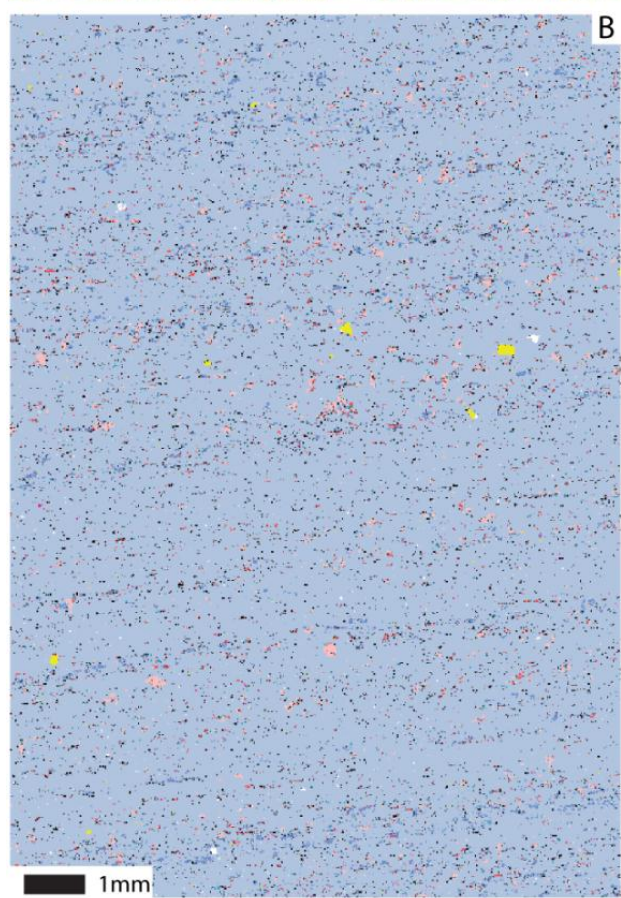
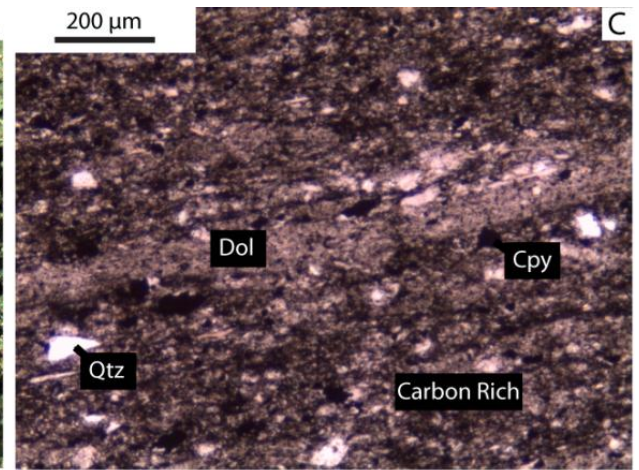
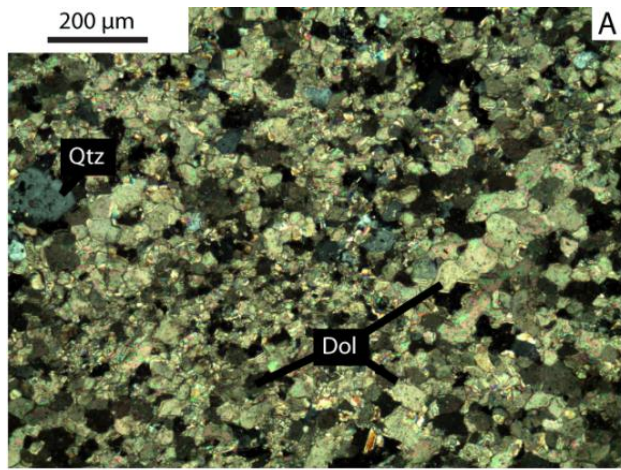
### **3.3 Nguba Group - Kakontwe Limestone**

Drilling at Fishtie has intersected a maximum thickness of 120 meters of the Kakontwe Limestone (Cailteux et al., 2007). The Kakontwe Limestone unit at Fishtie consists largely of dolostone and partially dolomitized limestone (3.8a, b); company logs indicate that limestone beds are locally present near the base of the formation. The base of the unit generally consists of grey massive dolostones that commonly display planar to domal stromatolitic laminations. These are overlain by a mixed zone of massive dolostone containing layers of pink colored dolostone with thin argillaceous bands and distinctive pink to green interval. This is capped by variably dolomitized argillaceous banded limestone with thin argillaceous bands, a pinstriped dolostone layer, and dolomitic siltstones. The pinstriped dolostone layer displays interlayered white and pink to grey and green beds that average 5 millimeters in thickness. Dolomitic siltstone beds are laterally equivalent to variably dolomitized limestones in the upper portions of the Kakontwe Limestone unit at Fishtie and appear to increase in abundance and thickness to the east. They are commonly finely laminated.

Massive dolostones and pinstriped dolostones consist largely of 10-100 micron sized grains of anhedral dolomite. Dolomite replaces anhedral calcite grains of similar size. The dolomite is relatively free of inclusions but may display some dusting near grain margins. Massive and pinstriped dolostones contain small amounts of disseminated subrounded quartz grains, rare white mica, and minor cubic to subhedral pyrite grains up to 150 microns in diameter (Figure 3.8a).

Dolomitic siltstones are composed of alternating dolomite- and siliciclastic-rich beds. Individual beds range from 1mm to greater than 30 mm in thickness and rhythmically alternate between dolomite-rich, siliciclastic-rich, and carbonaceous layers (Figure 3.8c, d).

Figure 3.8: Photomicrographs and QEMSCAN® images of the Kakontwe Limestone unit. (A) Cross-polarized photomicrograph of massive dolostone. Dolomite occurs as subrounded to subangular grains that are intergrown with subordinate quartz. Calcite is less common, and forms small grains (KEDD0135, 141.5m). (B) QEMSCAN® image utilizing a 15 micron resolution, of Limestone from the least altered portion of the deposit. Calcite is dominant with lesser dolomite that forms weakly developed planar bedding planes. Minor quartz and potassium feldspar occur as small grains throughout the sample. Pyrite is sporadic as small subhedral crystals (DDH KEDD0076, 115m). (C) Plane-polarized photomicrograph of dolomitic siltstone. Quartz and dolomite occur as subrounded to subangular grains and have abundant carbonaceous material interstitial to grain boundaries (KEDD0142, 139.5m). (D) QEMSCAN® image utilizing a 15 micron resolution, of rhythmically bedded dolomitic siltstone. Beds alternate between dolomite rich and siliciclastic rich. Siliciclastic beds are composed of small subround to subangular quartz and potassium feldspar grains. Dolomite rich beds contain minor quartz and potassium feldspar and have increased abundance of carbonaceous material (DDH KEDD0085, 150m).



- |           |                    |          |                |
|-----------|--------------------|----------|----------------|
| Quartz    | Albite             | Ankerite | Other Minerals |
| Muscovite | Potassium Feldspar | Dolomite | Others         |
| Chlorite  | Apatite            | Calcite  |                |
| Biotite   | Rutile             | Pyrite   |                |

The siliciclastic beds contain quartz, dolomite, and potassium feldspar in addition to minor white mica. They are generally carbonaceous with organic material forming irregular masses interstitial to dolomite, quartz, and potassium feldspar grains. Organic material also forms semi-continuous layers within the dolomitic siltstones up to 3mm thick.

Carbon and oxygen isotopic analysis was performed on suites of samples from the basal 90m of the Kakontwe Limestone unit from two drill holes at Fishtie. The Kakontwe Limestone unit in both holes was largely dolomitized indicating post depositional diagenetic alteration; neither hole displayed significant hydrothermal alteration or mineralization. Many workers believe that dolomitized carbonate rocks may retain their original  $\delta^{13}\text{C}$  composition as the high concentration of carbon in the carbonate rocks relative to meteoric fluids makes the  $\delta^{13}\text{C}$  ratio much more resistant to diagenesis than  $\delta^{18}\text{O}$  (Halverson et al., 2005).

The carbon and oxygen isotopic values of the carbonate rocks at Fishtie (Appendix F) are similar to those in the Kakontwe Limestone to the north on the eastern edge of the Zambian Copperbelt (Itawa drill hole IT-26; Bull et al., 2011) and to those at the Kipushi deposit to the northwest of the Zambian Copperbelt (Berger et al., 2013) (Figure 3.9). They are heavier than isotopic values in the thin limestone beds present within siltstones and sandstones of the lower Nguba Group above the Grand Conglomérat at the Kamoia deposit on the western margin of the Katangan basin (Schmandt, 2012) (Figure 3.9).

The differing isotopic values between carbonate rocks in the Kakontwe Limestone unit in the Fishtie-Zambian Copperbelt region and the Kamoia area may reflect fundamentally different depositional environments. The Kakontwe Limestone in the Fishtie-Zambian Copperbelt area formed a regionally extensive shelf-type carbonate (Wendorff and Key, 2009) while at Kamoia

limestone above the Grand Conglomerate forms thin (<2m thick) discontinuous beds in reddened siltstones (Hitzman pers. comm., 2012).

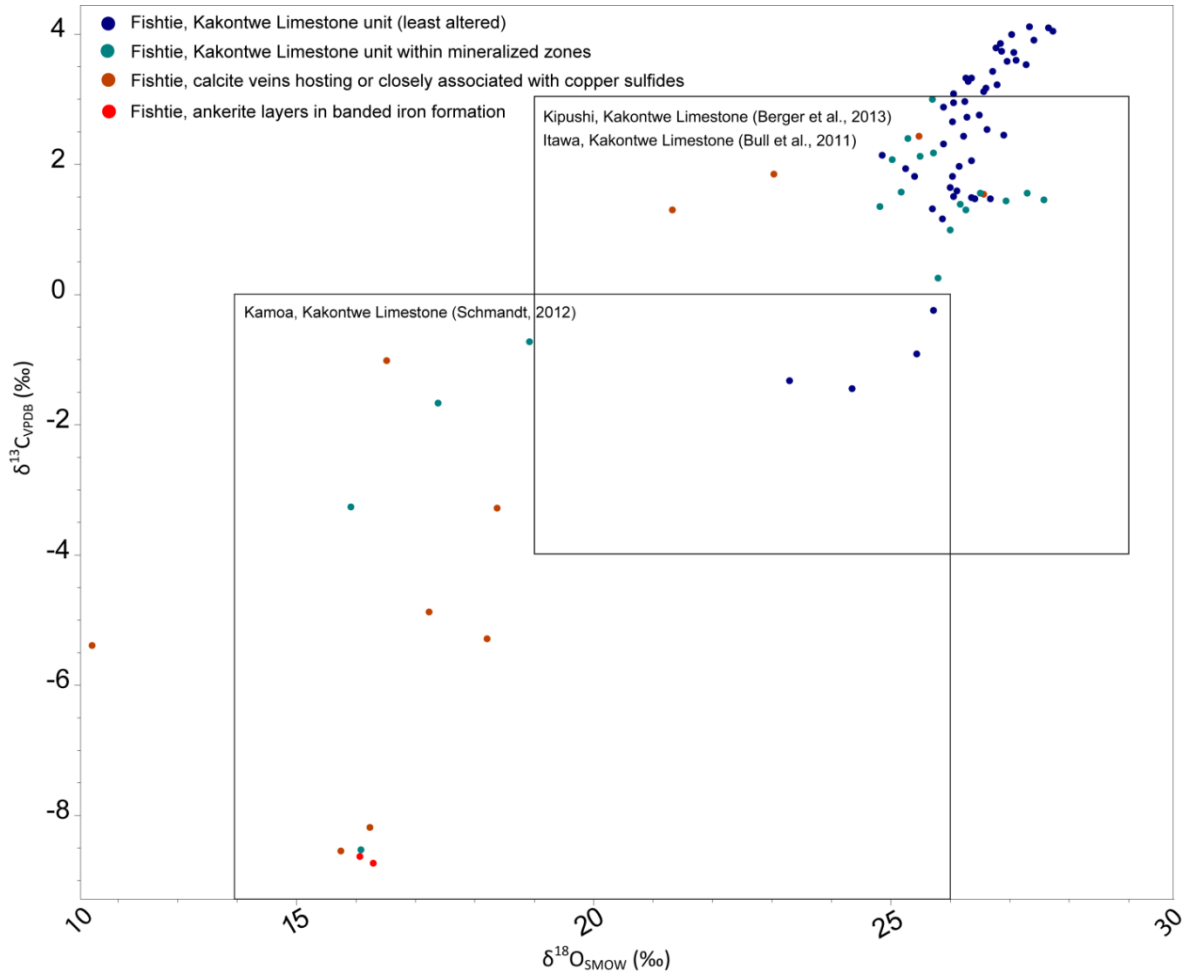


Figure 3.9: Carbon and oxygen isotopic values of unaltered and altered samples of the Kakontwe Limestone unit, calcite veins, and ankerite in iron formation within the Grand Conglomerat unit from Fishtie. Boxes outlining carbon and oxygen isotopic data from unaltered Kakontwe Limestone rocks from the eastern Zambian Copperbelt (Bull et al., 2011), the Kipushi deposit (Berger et al., 2013), and the Kamao deposit (Schmandt, 2012) indicate that there is substantial overlap between the data from Fishtie, the Zambian Copperbelt, and Kipushi but that the carbonate rocks in the lower Nguba Group at Kamao display distinctly lower isotopic values. There is a trend to lighter carbon and oxygen isotopic values in samples from mineralized zones at Fishtie from the least altered samples. Calcite from veins hosting sulfides, or spatially closely associated with sulfides, tends to have even more depleted carbon and oxygen isotopic values at Fishtie. Ankerite from the iron formation at Fishtie display extremely depleted values relative to dolomite from the least altered Kakontwe Limestone unit.

Carbon and oxygen isotopic chemostratigraphy through the lower 90m of the Kakontwe Limestone unit at Fishtie shows a regular variation in both carbon and oxygen isotopic values through the section from lighter values immediately above the Grand Conglomérat unit to heavier values in the upper portions of the unit (Figure 3.10). The pink colored dolostone units, in particular the pinstriped dolostone layers, have lighter isotopic values than the enclosing more massive dolostones. The carbon isotopic values from these two closely spaced drill holes, while displaying similar patterns, do have distinctly different values calling into question whether they reflect original  $\delta^{13}\text{C}$  compositions; similar results have been reported in other Neoproterozoic cap carbonate sequences (Jiang et al., 2003).

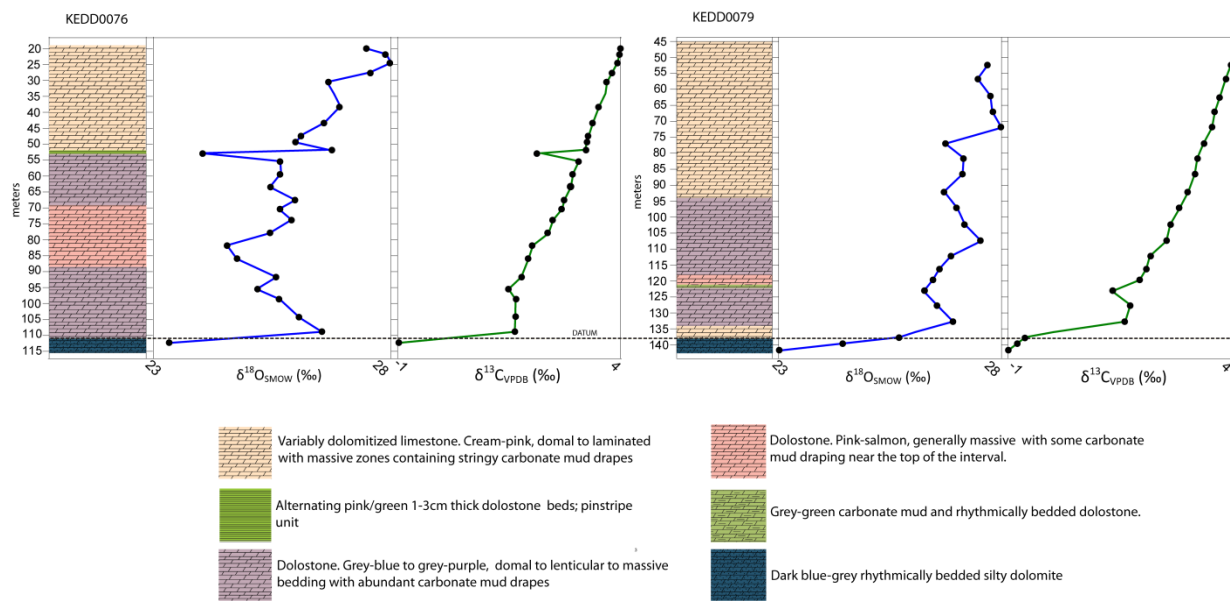


Figure 3.10: Stratigraphy of the Kakontwe Limestone unit in drill holes KEDD0076 and 0079 which are located approximately 230 m from one another in the eastern structural domain. Both drill holes show a progression from dolostones at the base of the sequence up into dolomitized limestone. The  $\delta^{13}\text{C}_{\text{VPDB}}$  (‰) and  $\delta^{18}\text{O}_{\text{SMOW}}$  (‰) values of samples from these drill holes display a general trend towards lighter values with depth. Values at the base of the sequence probably reflect the negative carbon excursion (Rasthof anomaly) associated with the Sturtian glacial event (Halverson et al., 2010).

Data from around the world indicate that negative  $\delta^{13}\text{C}$  excursions are present both beneath the Sturtian glacial diamictites (Islay anomaly) and at the base of the cap carbonate rocks above the diamictites (Rasthof anomaly; Yoshioka et al., 2003; Halverson et al., 2005). Both these anomalies are observed in the Itawa section through the Kakontwe Limestone at Itawa to the north of Fishtie (Bull et al., 2011). The data from Fishtie appears to indicate the presence of the Rasthof anomaly. Thus, the carbon isotopic chemostratigraphy of the Kakontwe Limestone at Fishtie is consistent with global composite curves (Jacobson and Kaufman, 1999; Halverson et al., 2010).

## CHAPTER 4

### STRUCTURAL GEOLOGY OF THE FISHTIE AREA

Regional magnetic data (Figure 1.3; Appendix A) suggests the Fishtie deposit is located above a basement horst on the northern margin of the Lusale basin. Drilling indicates that the deposit area contains a series of sub-vertical normal faults that strike sub-parallel to the basin margin and form an arcuate pattern (Figure 1.3; 1.4; 3.2). These faults are inferred from offsets of the contact between basement rocks and the Grand Conglomérat unit and the contact between the Grand Conglomérat and Kakontwe Limestone units. None of the generally vertical drill holes logged for this study intersected deformed rocks that could represent a normal fault. The normal faults in the Fishtie area appear to control both thickness and facies variations in the Grand Conglomérat and Kakontwe Limestone units. They also apparently controlled the thickness and grade of both iron oxide and sulfide mineralized zones.

Most of the normal faults display downthrow to the south into the Lusale basin (Figure 1.3; 1.4; 3.2). Maximum offsets along the normal faults appear to be <100m. Available data suggest the normal faults have lengths of up to 1.5 km though lateral extensions of many of the faults are not well constrained by drilling data. Measurement of offsets along the faults suggests a regular progression of displacement (Figure 1.3; 1.4). The geometry of the fault and displacement gradients along individual faults suggest they may form a series of segmented fault arrays in which displacement was transferred between structures by ramp-relay zones (Walsh and Watterson, 1989).

The normal fault pattern was utilized to divide the deposit area into different structural domains (Figure 1.4). Normal faults in the western structural domain strike north-northeast and dip steeply to the southeast. The central structural domain has generally east-trending normal

faults that dip to the south. These faults are offset along a series of north-striking dip-slip faults. Normal faults in the eastern domain strike west-northwest and dip to the southwest. The satellite domain covers an area with a thicker preserved sequence of the Kakontwe Limestone unit that appears to contain both east- and north-striking normal faults.

The western structural domain contains three laterally unconstrained northeast-trending, subvertical to steeply south dipping faults with normal offsets of 15 to 65 m. The Grand Conglomérat unit thickens significantly towards the southernmost normal fault (Section A-A', Figure 3.2). This fault appears to have had approximately 50m of synsedimentary displacement (sections A-A', B-B', Figure 3.2). Iron formation within the Grand Conglomérat unit in this domain thickens toward the normal fault. The Kakontwe Limestone unit is present only to the south of this fault; to the north it has been eroded or replaced by weathered saprolite.

The central structural domain contains the thickest and highest-grade portion of the Fishtie deposit as currently known. This domain contains two east-trending normal faults with down to the south displacements. Drilling suggests the central domain is bound to the north by an east-trending normal fault with north side down displacement of approximately 50m (section C-C', Figure 3.2). The Grand Conglomérat unit thickens significantly towards the southernmost east-trending fault in the central domain; this fault displays an offset of approximately 40m. Drilling suggests that this thickening may be caused primarily by increased thicknesses of siltstone layers within the Grand Conglomérat unit. Such thickening is not evident towards the east-trending fault immediately to the north, which has an apparent normal offset of 25m. Iron formation occurs both adjacent to the southernmost east-trending normal fault and further south (section C-C', Figure 3.2). Iron formation is also present in the central structural zone along the hanging wall to the northernmost east-trending fault. Sulfide mineralization occurred adjacent to

both of the down to the south east-trending faults but was much more intense along the northern fault. Current drilling suggests the Kakontwe Limestone unit is laterally equivalent to the uppermost portion of the Grand Conglomérat unit in the central structural zone.

The east-trending normal faults in the central structural domain appear to be cut and offset by two northeast-trending dextral strike-slip faults. Similar trending normal faults appear to separate the central and eastern structural domains. These steeply dipping faults appear to display normal movement with a combined downthrow to the west of approximately 60m.

The eastern structural domain contains at least two generally east-southeast-trending normal faults. The southernmost normal fault in this domain has a normal offset of approximately 25m while the northern fault has a normal offset of 35m to the south. A long section through the eastern structural domain (section E-E', Figure 3.2) indicates the Grand Conglomérat unit progressively thins to the east across this domain. There has been insufficient drilling to determine whether the east-southeast-trending normal faults controlled thickness variations in the Grand Conglomérat or Kakontwe Limestone units.

The eastern structural domain is separated from the satellite structural domain by two north-northeast-trending sub-vertical normal faults that have a combined normal downthrow of over 100 meters. The satellite structural domain forms a graben bound to the east and west by generally north-trending normal faults. Normal faults on the west side of this graben have a combined offset of approximately 100m; the more poorly constrained normal fault marking the eastern edge of the graben appears to have an offset of only 15m. Drilling is insufficient in this area to determine whether the Grand Conglomérat unit displays thickness changes relative to the east-northeast-trending normal faults; there appears to be no changes in the thickness of the Grand Conglomérat unit relative to the north-trending normal faults. Thickness and facies

changes relative to both fault sets are apparent in the overlying Kakontwe Limestone unit, which contains more dolomitic siltstone to the north and east (section D-D', Figure 3.2). Although sulfide mineralization of the Kakontwe Limestone unit occurred in the satellite structural domain, it appears that iron formation was not developed in the Grand Conglomérat unit in this area.

## CHAPTER 5

### DIAGENETIC AND HYDROTHERMAL MINERALIZATION

The fine grain size of the metasedimentary rocks at Fishtie made differentiating detrital grains, diagenetic minerals, minerals precipitated during genesis of iron formation, and hydrothermal mineral assemblages difficult. Though the rocks at Fishtie undoubtedly experienced low-grade metamorphism during the Lufilian event, no obvious metamorphic fabrics are present in the Katangan sequence. Hydrothermal mineral assemblages were delineated during logging and then examined with transmitted and reflected light petrography. Representative samples of end member mineral assemblages were analyzed using the QEMSCAN® instrument to better understand both mineralogy and textures.

Diagenetic mineralization of the Grand Conglomérat unit diamictites and siltstones is difficult to distinguish from later hydrothermal mineralization, but likely included albitization of plagioclase and conversion of calcite to dolomite. The paragenetically earliest hydrothermal event was the formation of a magnetite-ankerite-apatite assemblage that defines the iron formation in the Grand Conglomérat unit. This was followed by potassic mineralization of the Grand Conglomérat unit and dolomitic siltstones of the Kakontwe Limestone units.

Hydrothermal mineralization in the Grand Conglomérat unit resulted in the growth of potassium feldspar, biotite, muscovite, and chlorite. The mineralogy of diamictites in the Grand Conglomérat unit correlates to color which changes from grey (least altered) to brownish to pale grey to greenish within the Fishtie area. These color changes were noted during logging and confirmed with petrographic observation. The petrographic correlation of dominant mineral assemblages to zones mapped in drill core form the basis for delineation of different alteration zones.

Grey diamictites generally contain moderate to relatively abundant potassium feldspar as well as an assemblage of biotite, muscovite, and chlorite. Brownish diamictites contain significant amounts of biotite with less muscovite and chlorite. Pale grey colored diamictites generally contain relatively abundant muscovite. Greenish diamictites are chlorite rich. The distribution of these different colored intervals can be grouped into schematic mineralized zones (Figure 5.1). It is difficult to tell from the available data the relative timing relationships between these styles of mineralization though it appears the chlorite mineralization is generally late. The Kakontwe Limestone unit most commonly displays potassium feldspar and chlorite mineralization.

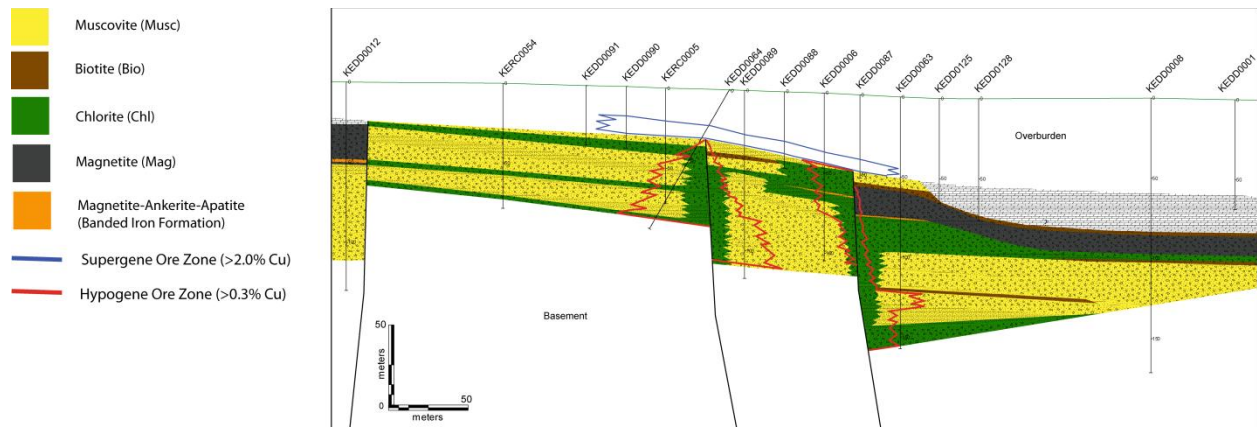


Figure 5.1: Schematic distribution of hydrothermal minerals and location of hypogene and supergene ore zones in cross section C-C'. Iron formation occurs adjacent to the southernmost and northern normal faults. It is overlain in the south by a zone with disseminated magnetite in the diamictite that thickens towards normal faults and is inferred to form a continuous layer in the south part of the section. Biotite mineralized zones occur primarily in the upper portions of the section and are not associated with economic copper-sulfide mineralized zones. Muscovite mineralized zones are present throughout this section and are associated with higher concentrations of copper sulfides. Chlorite is concentrated near the high angle normal faults and is typically associated with well-mineralized copper-sulfide zones. KEDD denotes diamond drill hole and KERCO denotes reverse circulation drill hole.

Hydrothermal mineral assemblages were best developed adjacent to the inferred high angle normal faults while diagenetic assemblages are best preserved distal to such structures. Although copper sulfides occur with biotite-dominant, muscovite-dominant, and chlorite-dominant mineral assemblages in the Grand Conglomérat unit they appear most abundant in chlorite-rich assemblages and least abundant in biotite-rich assemblages.

As in the Kamoia deposit (Schmandt et al., in press), lithic clasts in the Grand Conglomérat unit commonly display rims with coarser grained alteration minerals. These rims may completely enclose a clast but are generally discontinuous. The mineralogy of the rims reflects the dominant mineralogy (biotite, muscovite, or chlorite) of the surrounding diamictite matrix (Figure 3.4). Some of the mineral rims on diamictite clasts, particularly those with abundant chlorite, contain coarse copper sulfides. Unlike Kamoia, such mineral rims rarely form preferentially above or below a clast. In contrast to Kamoia there does not appear to be a regular variation in mineralogy of the clasts vertically from the base of the Grand Conglomérat unit at Fishtie. Instead there is a lateral zonation away from the normal faults that mirrors that of the dominant mineral assemblage in the diamictite matrix.

### **5.1 Diagenetic Mineralization**

Diagenetic mineralization of the Grand Conglomérat unit diamictites and siltstones can rarely be discerned due to later hydrothermal events. Petrography and QEMSCAN® analysis indicates that before diagenesis and later hydrothermal mineralization the Grand Conglomérat unit diamictites were composed of small detrital grains of quartz and feldspar together with lithic clasts in a muddy, clay-rich matrix. Grand Conglomérat unit siltstones were likely composed of detrital grains of quartz, feldspar, calcite, dolomite, and clay while dolomitic siltstones in the Kakontwe Limestone unit were composed of calcite and dolomite grains and cements with minor detrital quartz, feldspar, and clay.

Rare quartz overgrowths on quartz grains in both diamictite and siltstone beds of the Grand Conglomérat unit likely formed during early diagenesis. Precipitation of additional quartz, together with carbonate minerals would have occurred during burial at shallow depths (<2 km) and low temperatures (~100°C). These conditions would also have allowed formation of chlorite from detrital clay and potassium feldspar overgrowths on detrital feldspar and quartz (Morad et al., 2000; Tucker et al., 2011). The presence of albite pseudomorphing detrital plagioclase in rocks at Fishtie suggests that diagenetic albitization occurred due to increased burial temperatures (Morad et al., 2000; Tucker et al., 2011). The preponderance of dolomite and relative absence of calcite in the Grand Conglomérat unit also indicates elevated burial temperatures.

The Kakontwe Limestone unit contains both limestone and dolostone beds. The presence of abundant stromatolitic textures suggests portions of the unit may have been originally deposited as dolostone. Neomorphism and early diagenesis would have resulted in recrystallization of original carbonate grains and precipitation of early carbonate cements. With burial much of the original calcite or aragonite in the unit was converted to dolomite.

## **5.2 Iron Formation**

Iron formation is restricted to the Grand Conglomérat unit where it is interlayered with siltstone beds. Iron formation occurs adjacent to the southernmost normal faults in the western and central structural domains where it attains maximum thicknesses of 10m. Iron formation has also been intersected on the northern edge of the central structural domain where it is associated with a north side down normal fault (section C-C', Figure 3.2). Well-developed iron formation is restricted to near the top of the Grand Conglomérat unit. Disseminated magnetite and ankerite are locally present within diamictites and siltstones primarily above lenses of iron formation

(Figure 5.1). Iron formation thickens and the amount of disseminated magnetite in diamictites and siltstones above the iron formation increases towards the normal faults.

Iron formation is composed of quartz, magnetite, ankerite, apatite, chlorite, and biotite (Figure 5.2a, b). Iron formation typically consists of alternating bands or beds rich in magnetite, ankerite, or apatite all of which commonly contain minor to significant quartz. Geochemically, samples of the iron formation contain up to 46 wt. %  $\text{Fe}_2\text{O}_3$  and are siliceous (32-58 wt. %  $\text{SiO}_2$ ) (Appendix B). They contain up to 4 wt. %  $\text{P}_2\text{O}_5$  due to apatite and are anomalous in barium with values up to 240 ppm though no barite has been observed petrographically. The iron formation has very low manganese contents, with maximum values less than 1 wt. %. The iron- or phosphorous-rich layers are commonly interbedded with siltstone or thin diamictite beds that contain significant disseminated magnetite and/or ankerite. Both the siltstone beds and some iron-rich beds display textures suggestive of graded bedding as well as slumps and intraformational folds. Individual bands within the iron formation may consist of nearly monomineralic or bimineralic assemblages of magnetite and quartz or ankerite or apatite (Figure 5.2a, b).

Siltstone and diamictite beds above iron formation layers commonly contain disseminated anhedral to subhedral magnetite (10-100 $\mu\text{m}$ ) (Figure 5.2c, d). Disseminated magnetite in these beds is commonly intergrown with chlorite that is in turn partially replaced by biotite. The distribution and textures of this magnetite suggest it grew in the diamictite after deposition. No clasts of iron formation have been observed in the diamictite, even in diamictite directly overlying iron formation bands. The iron formation lacks significant muscovite and potassium feldspar and generally contains less biotite than typical siltstones in the Grand Conglomérat unit. It does contain relatively abundant chlorite and has  $\text{Al}_2\text{O}_3$  values that are

similar to the adjacent siltstones (Appendix B). Distinct detrital grains of quartz similar to those present in Grand Conglomérat unit siltstones are absent in the samples of iron formation examined for this study.

Magnetite in iron formation forms subhedral to euhedral grains that are up to 100 $\mu$ m in diameter. It is most commonly intergrown with quartz. Magnetite in both the iron formation and in the diamictites may be replaced by hematite that is in turn locally replaced by goethitic iron oxides (“limonite” in QEMSCAN images). Ankerite in the iron formation occurs as small to moderate sized (20-200  $\mu$ m) subhedral to anhedral crystals. Thin beds within the iron formation may consist almost entirely of either magnetite or ankerite and contain minor to abundant quartz. Apatite occurs as a minor constituent throughout the iron formation but also forms thin, nearly monomineralic apatite bands. The apatite is anhedral to subhedral and ranges up to 200 $\mu$ m in diameter. Chlorite is common as small (10-50  $\mu$ m) anhedral grains that rim or are intergrown with magnetite, and are in turn rimmed by biotite (Figure 5.3a, b, c).

The absence of iron formation clasts together with the presence of disseminated magnetite in the diamictites suggest that the iron formation formed largely by precipitation of a magnetite-ankerite-apatite assemblage within the more permeable siltstones in the Grand Conglomérat unit, rather than as a chemical sediment. The presence of apparent graded beds within the iron formation is also difficult to reconcile assuming iron formation was a chemical sediment, as it would appear to be difficult to produce graded beds from amorphous iron-rich gels or chemically-deposited varves (Bekker et al., 2010).

The iron formation is anomalous in copper with values ranging between 80 and 650 ppm (Appendix B). Petrography demonstrates that chalcopyrite overgrows magnetite both within the

iron formation and within the diamictite. These relationships clearly indicate that copper mineralization postdates the iron formation.

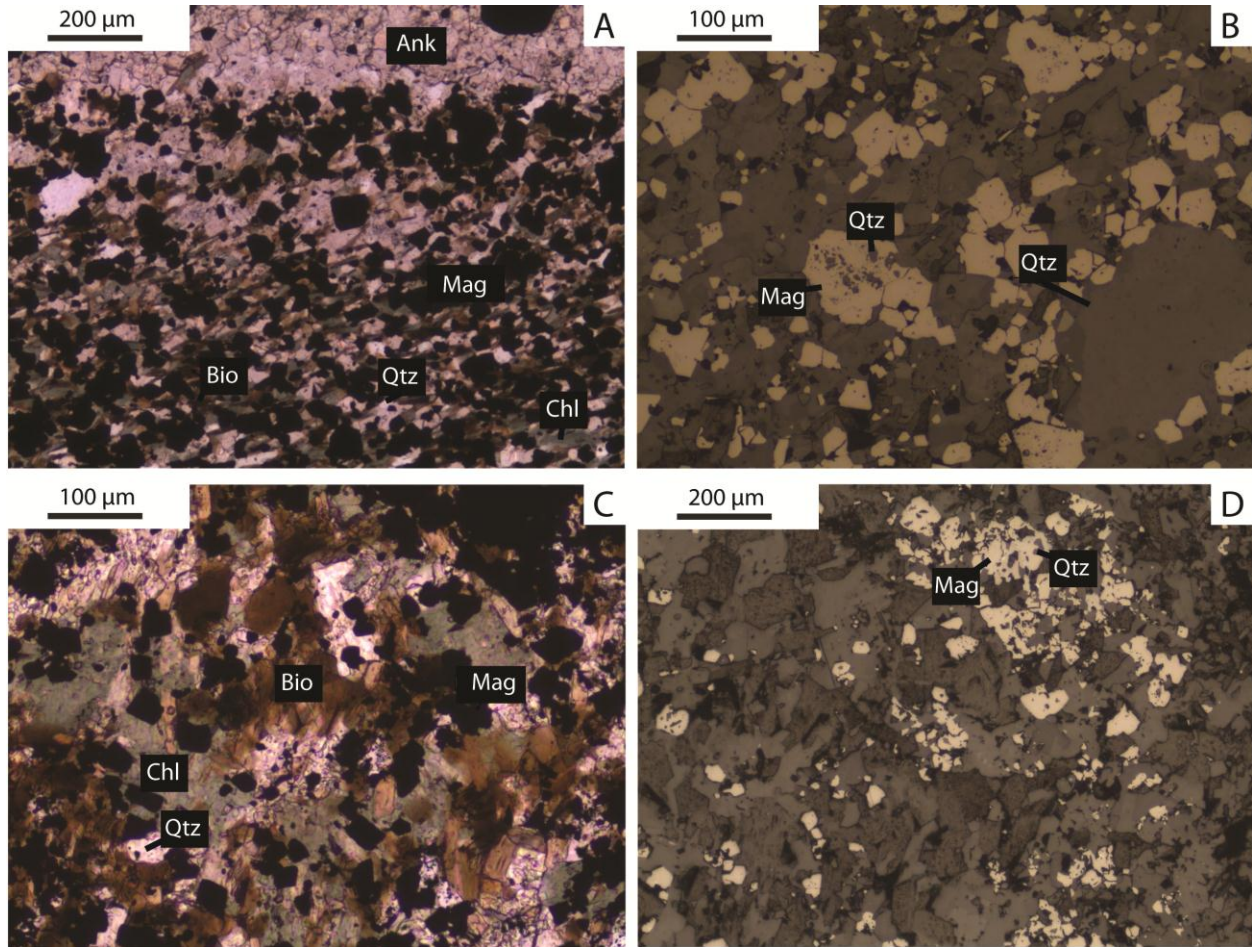


Figure 5.2: Iron formation within the Grand Conglomérat unit from the central structural domain. (A) Plane-polarized photomicrograph of iron formation consisting of interlayered bands of ankerite and magnetite. The magnetite layers consist of aggregates of euhedral magnetite that is locally replaced by hematite and intergrown with chlorite (DDH KEDD0006, 62m). (B) Reflected light photomicrograph of magnetite in the iron formation intergrown with chlorite (DDH KEDD0006, 62m). (C) Typical magnetite crystals in Grand Conglomérat unit diamictite matrix. The magnetite has euhedral to subhedral shapes and is intergrown with chlorite and lesser quartz and ankerite (KEDD0008, 97m). (D) Reflected light photomicrograph of Grand Conglomérat unit diamictite containing disseminated subhedral to anhedral magnetite (KEDD0008, 97m).

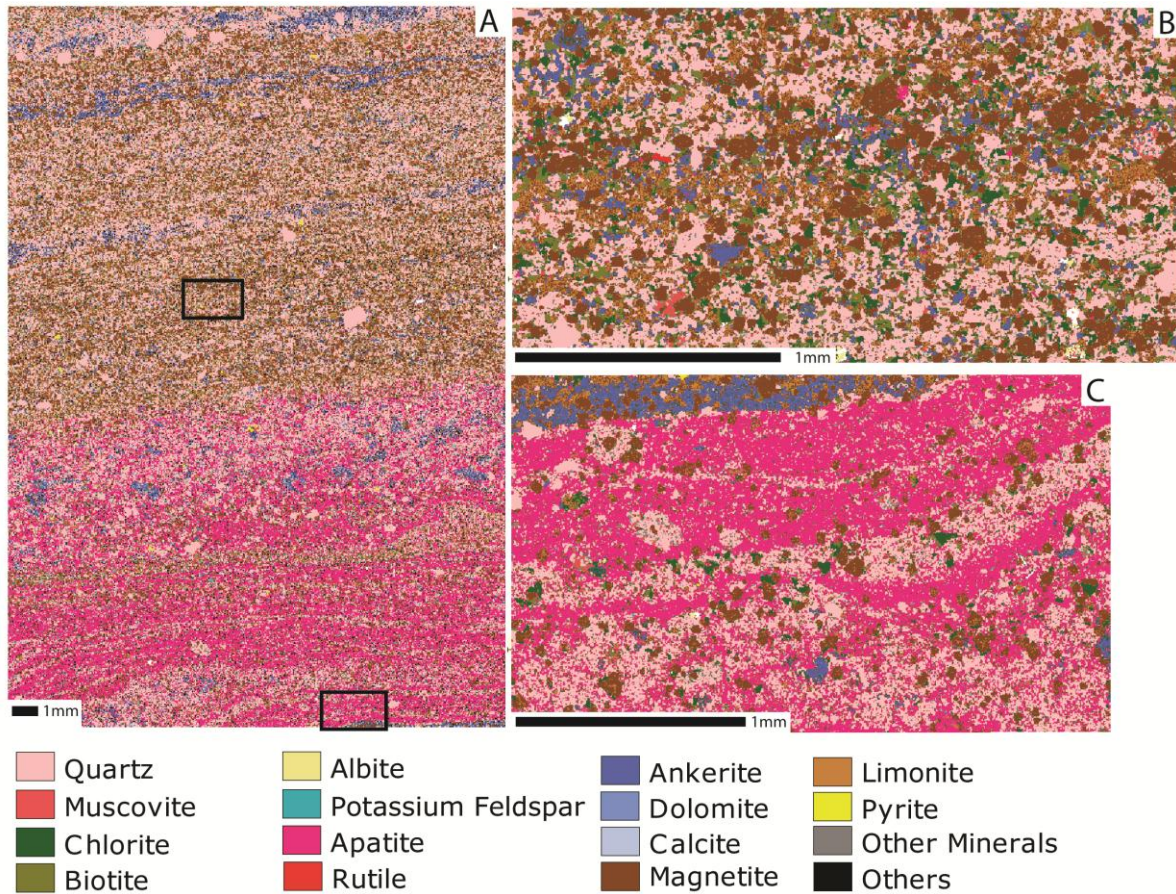


Figure 5.3: Iron formation within the Grand Conglomérat unit from the western structural domain (DDH KEDD0033, 44m). (A) QEMSCAN® image with a 15 micron resolution of typical iron formation. The upper part of sample contains abundant magnetite that is intergrown with quartz and minor ankerite and apatite. The lower portion of the sample is apatite rich. A band with irregular clots of ankerite separates the two domains. The apatite-rich zone contains quartz-rich and magnetite-rich bands that appear to represent relict siltstone beds. The area of images (B) and (C) are outlined in black. (B) Enlarged view of iron formation in (A) at 2 micron resolution. The sample consists of intergrown quartz, magnetite, and ankerite with minor chlorite, biotite, muscovite, and apatite (DDH KEDD0033, 44m). (C) Enlarged view of iron formation in (A) at 2 micron resolution. The sample is composed of apatite and quartz with intergrown magnetite, chlorite, and ankerite. Apatite occurs as semi-continuous bands that are depleted in magnetite and chlorite. Ankerite at the base of the image occurs as a continuous band intergrown with magnetite.

### 5.3 Potassium Feldspar and Biotite Mineralization

Potassium feldspar, commonly with intergrown biotite, is common throughout the Grand Conglomérat unit and dolomitic siltstones of the Kakontwe Limestone unit. Potassium feldspar is

most abundant in zones that were logged as weakly altered. In the Grand Conglomérat unit potassium feldspar is generally present as thin rims on quartz grains, as intergrowths with biotite, or as scattered grain remnants in areas with abundant biotite, muscovite, and/or chlorite. These textural relationships suggest an early period of potassic mineralization involving the precipitation of both potassium feldspar and biotite. Potassium feldspar is essentially absent in iron formation though these rocks may have contained little clay, plagioclase feldspar, or white mica that would have allowed for the alteration to potassium feldspar. In the Zambian Copperbelt detrital clay and plagioclase feldspar were pervasively replaced by potassium feldspar during hydrothermal alteration (Darnley, 1960; Selley et al., 2005). Schmandt et al. (in press) noted a similar potassic alteration event at the Kamoia deposit that was largely overprinted by later silicification and chlorite mineralization.

The Grand Conglomérat diamictite locally displays a distinct brownish color resulting from an abundance of biotite (Figure 5.4a, b, c). Such biotite-rich diamictite is most common at the top of the Grand Conglomérat unit at Fishtie (Figure 5.1) though minor biotite occurs throughout the unit. Biotite in such zones forms semi-continuous aggregates of grains throughout matrix and is locally concentrated around the margins of clasts. It is commonly intergrown with potassium feldspar. Biotite may contain small (10-50  $\mu\text{m}$ ) subhedral to anhedral inclusions of muscovite (Figure 5.4a) and commonly replaces chlorite (Figure 5.4b). Apatite is common in matrix as small (10-40  $\mu\text{m}$ ) rounded crystals that are rimmed or partially replaced by calcite or dolomite. The biotite-rich samples investigated with petrography and QEMSCAN® analysis contain more albite than other samples examined. Albite occurs as detrital grains that are often rimmed or partially replaced by biotite (Figure 5.4c). Calcite forms small to moderate sized (20-

150+  $\mu\text{m}$ ) anhedral crystals in matrix. It may contain small cores of dolomite or display thin rims (5-15  $\mu\text{m}$ ) of dolomite (Figure 5.4d, e).

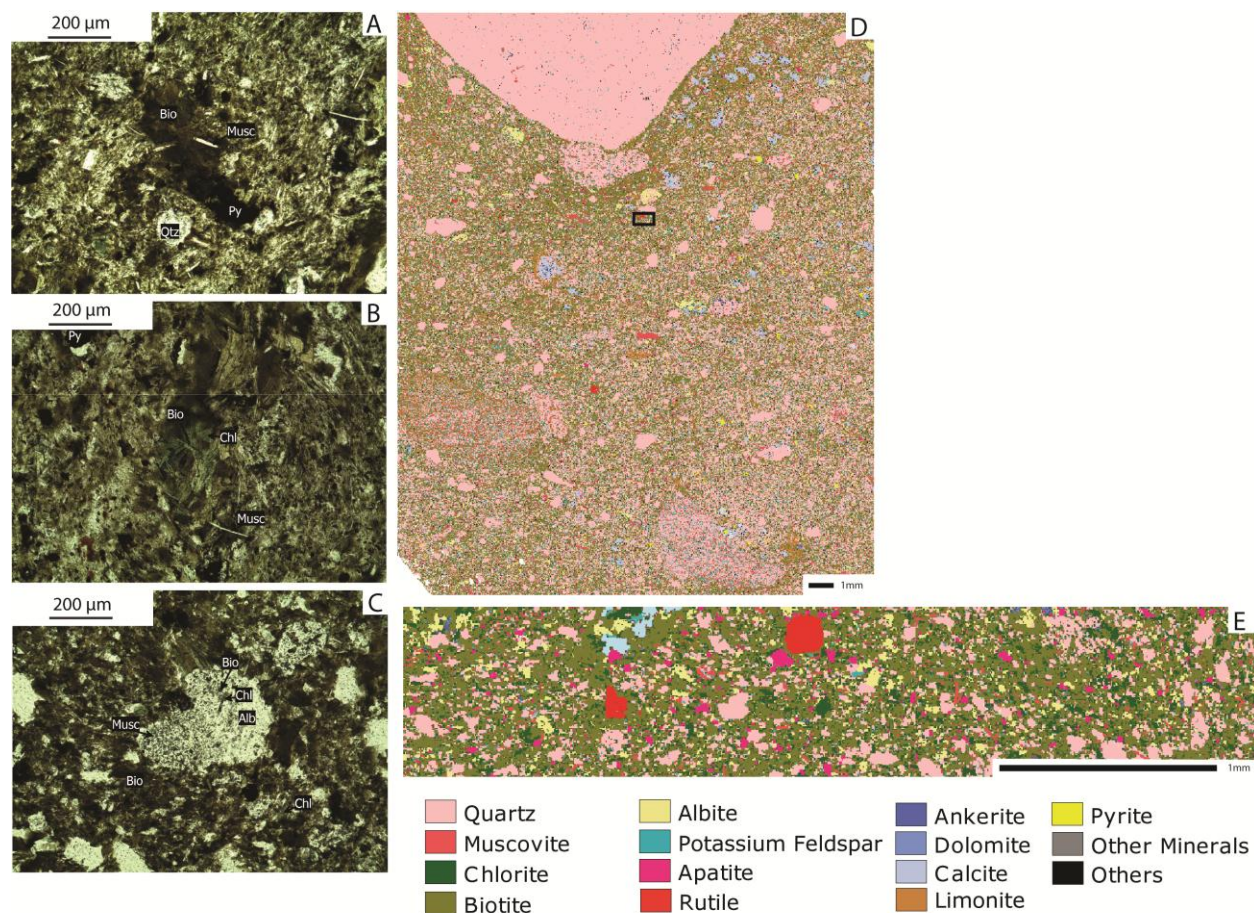
#### **5.4 Muscovite Mineralization**

Grey colored diamictites are the most common diamictite type at Fishtie. They contain abundant muscovite. Extremely muscovite-rich diamictites are spatially associated with areas of copper mineralization (Figure 5.1). In the matrix of grey colored diamictite beds muscovite forms aggregates of crystals that exceed one millimeter in length and overgrow detrital and diagenetic quartz and albite and disseminated magnetite and apatite in diamictites above iron formation (Figure 5.5a, b). Muscovite is often intergrown with, but more commonly replaces, potassium feldspar. Muscovite rarely occurs as coarse flakes up to 1mm in length around the margins of clasts in the diamictite where it is intergrown with or replaced by biotite and chlorite. Muscovite-mineralized rocks generally lack calcite and dolomite but contain ankerite. Ankerite is commonly restricted to clast rims or to chlorite-rich zones where it is associated with sulfides suggesting it is related to a later phase of mineralization (Figure 5.5c, d).

#### **5.5 Chlorite Mineralization**

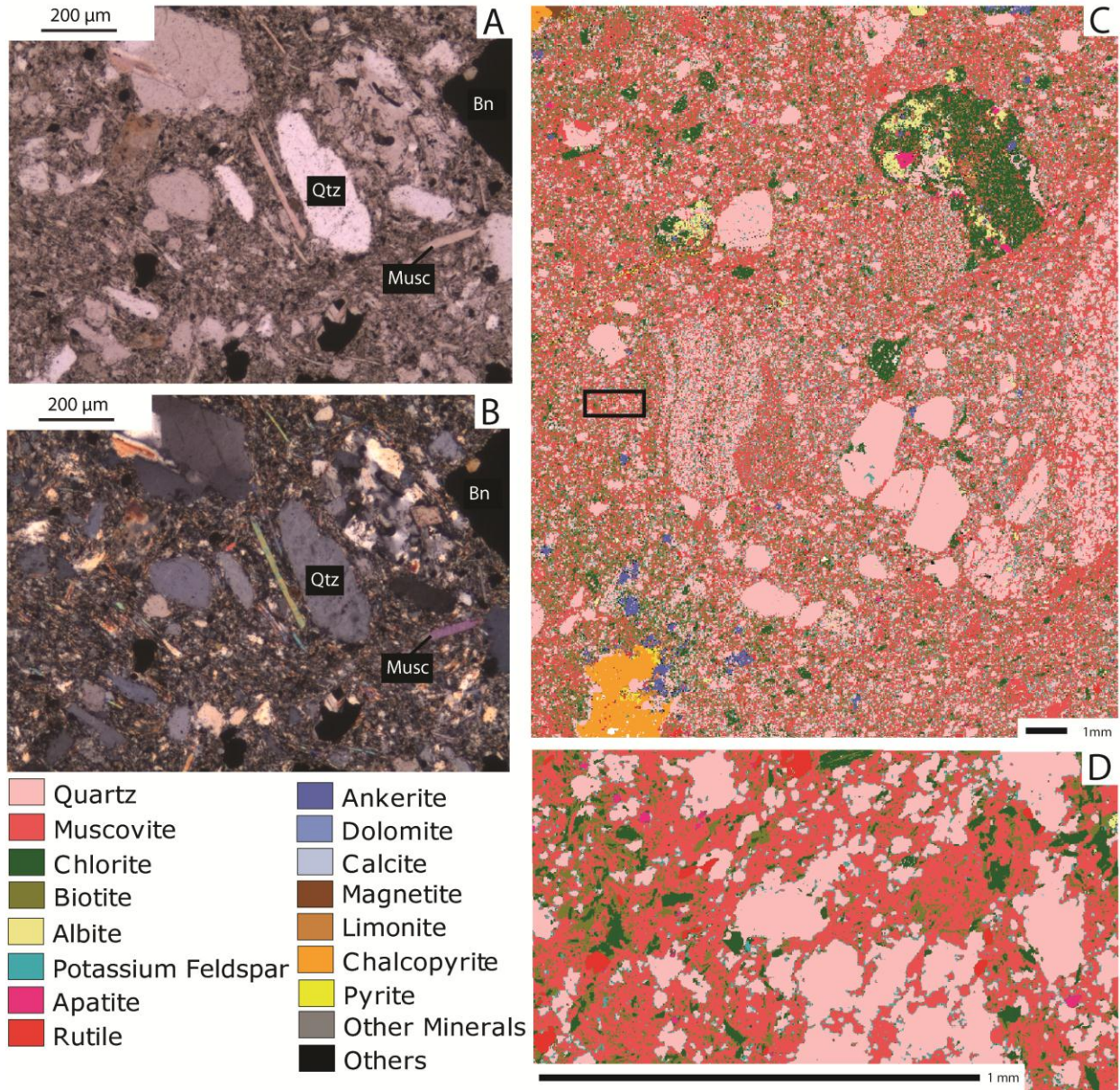
Chlorite is present throughout the Grand Conglomérat unit as well as in copper-sulfide mineralized areas of the Kakontwe Limestone unit. It is also present intergrown with magnetite, ankerite, and apatite in the iron formation. While the chlorite in the iron formation is likely related to its formation, that in the Grand Conglomérat (removed from areas of magnetite alteration associated with the iron formation) and Kakontwe Limestone units is commonly intergrown with sulfide minerals indicating it represents a separate hydrothermal event. Grand Conglomérat unit diamictites with a distinct greenish color are present adjacent to several of the normal faults at Fishtie (Figure 5.1).

Figure 5.4: Biotite-mineralized Grand Conglomérat unit diamictite. (A) Plane-polarized photomicrograph of biotite-mineralized diamictite. Biotite occurs as pervasive small to moderate sized sub- to anhedral crystals that contain inclusions of muscovite indicating it has been replaced by biotite. Pyrite is present as small subhedral crystals (DDH KEDD0008, 98.6m). (B) Plane-polarized photomicrograph showing biotite replacing chlorite and muscovite. (DDH KEDD0008, 98.6m). (C) Plane polarized photomicrograph showing biotite partially replacing the outer edges of an albite grain. The interior of the albite grain is partially altered to muscovite, chlorite, and biotite (DDH KEDD0008, 98.6m). (D) QEMSCAN® image at a 15 micron resolution of biotite-mineralized diamictite. The sample contains subrounded clasts of vein quartz, quartzite, and schist set in a matrix of biotite and quartz with subsidiary chlorite replacing biotite. The matrix contains relatively sparse muscovite which occurs as inclusions in biotite aggregates suggesting it has been largely replaced as shown in (A). The sample contains relatively abundant small grains of albite intergrown partially replaced by biotite as shown in (C). The sample also contains relatively abundant disseminated apatite intergrown with biotite. Several grains of calcite are present, some of which have cores of ankerite. Minor pyrite and pyrrhotite are present as small disseminated grains within biotite. The area of image (D) is outlined in black (DDH KEDD0089, 46.3m). (D) QEMSCAN® image showing an enlargement of (C) at a 2 micron resolution. The image emphasizes the lack of muscovite and the abundance of biotite. The matrix of the diamictite is composed of biotite that encloses very small grains of quartz with lesser albite, apatite, muscovite, chlorite, and calcite. Biotite replaces albite, muscovite, and chlorite (DDH KEDD0089, 46.3m).



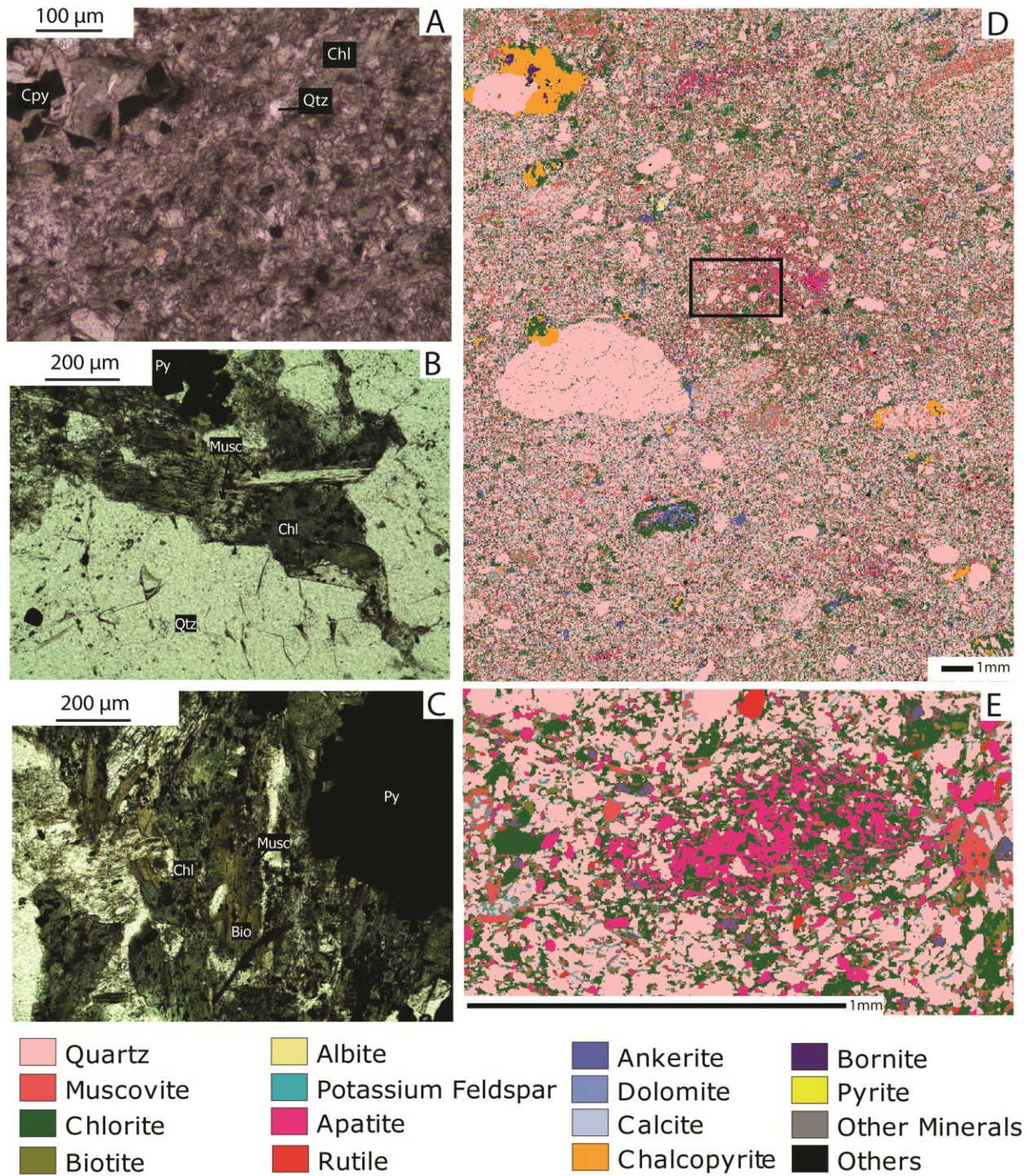
The greenish color of the diamictites is caused by abundant chlorite in the diamictite matrix (Figure 5.6a). This chlorite replaces both muscovite and biotite (Figure 5.6b, c). The chlorite forms small to moderate sized (20-200+ μm) anhedral grains. It does not display a preferred orientation. The chlorite-mineralized rocks are distinguished by abundant fine-grained quartz in the diamictite matrix (Figure 5.6d, e). This quartz lacks the obvious detrital shapes seen in samples lacking abundant chlorite. The textures suggest that this quartz precipitated during chlorite formation. Chlorite also forms relatively thick rims (100-200 μm) on the margins of clasts in the diamictites. Some of this clast-riming chlorite replaces biotite.

Figure 5.5: Muscovite-mineralized zones in the Grand Conglomérat unit diamictite. (A) Plane-polarized photomicrograph from muscovite-mineralized diamictite showing well developed and elongate muscovite laths and pervasive fine-grained white mica that overprints the detrital mineralogy. Minor biotite and chlorite are present. Disseminated grains of bornite are relatively common (DDH KEDD0064, 79.5m). (B) Cross polarized photomicrograph of the muscovite-mineralized diamictite in (A) (DDH KEDD0064, 79.5m). (C) QEMSCAN® image at 15 micron resolution of muscovite-mineralized diamictite. The diamictite contains clasts of vein quartz, schist, and altered mafic rocks in a fine-grained matrix dominated by muscovite and quartz. The clasts range from rounded to angular in shape. A clast consisting of chlorite, biotite, albite, apatite, and quartz is probably altered mafic igneous material. The matrix of the diamictite is dominated by muscovite that contains intergrown or replacive biotite that is itself locally replaced by chlorite. The matrix contains potassium feldspar primarily along the contact between quartz grains and muscovite and as several small clots preserved within muscovite. The texture suggests muscovite has replaced potassium feldspar. This sample contains an irregular aggregate of chalcopyrite with minor pyrite that is rimmed by quartz and ankerite. Ankerite is common in the lower portion of the image as irregular grains apparently intergrown with muscovite. The location of image (D) is outlined in black (DDH KEDD0008, 107m). (D) QEMSCAN® image showing an enlargement of the diamictite matrix in image (C) at a 2 micron resolution. The matrix consists of muscovite with lesser quartz, biotite, and potassium feldspar. Potassium feldspar is best preserved within or immediately adjacent to quartz grains. Biotite is commonly replaced by muscovite. The textures in this sample are interpreted to indicate that clay in the matrix of the diamictite was originally replaced by potassium feldspar and biotite, both of which were later replaced by muscovite; chlorite appears late. There are patches of anhedral ankerite scattered through the matrix (DDH KEDD0008, 107m).



Chlorite is both intergrown with and mantles apatite grains and grain aggregates. Chlorite also overgrows ankerite that occurs as small (20-50  $\mu\text{m}$ ) anhedral crystals throughout the matrix. Copper-sulfide minerals are most commonly intergrown with chlorite suggesting it is temporally related to the dominant period of sulfide mineralization (Figure 5.7).

Figure 5.6: Chlorite-mineralized Grand Conglomérat diamictite (A) Plane-polarized photomicrograph of chlorite-mineralized diamictite showing small chlorite crystals intergrown with or overgrowing quartz grains. Minor muscovite and biotite are present and replaced by chlorite. Coarse chalcopyrite is intergrown with chlorite (DDH KEDD0062, 101.4m). (B) Plane-polarized photomicrograph showing chlorite partially replacing the outer edges of a relatively thin muscovite lath and nearly completely replacing a larger crystal of muscovite directly below it (DDH KEDD0012, 41.5m). (C) Plane-polarized photomicrograph showing chlorite partially replacing a biotite crystal in the center of the image. Chlorite is intergrown with pyrite indicating the textural relationship with biotite is related to hydrothermal mineralization and not a retrograde reaction. Muscovite also partially replaces the same biotite crystal (DDH KEDD0012, 41.5m). (D) QEMSCAN® image at 15 micron resolution of chlorite-mineralized diamictite. Lithic clasts consist of vein quartz with some schist clasts and one chlorite-rich clast that may represent an altered mafic igneous rock. The matrix consists of intergrown small quartz and chlorite grains together with lesser ankerite, muscovite, and biotite. Chlorite replaces both muscovite and biotite. The sample contains several areas with abundant apatite, commonly with intergrown chlorite. Chalcopyrite with minor bornite rims several vein quartz clasts and appears to replace a portion of a quartz-rich clast. The location of image (E) is outlined in black (DDH KEDD-0006, 53.6m). (E) QEMSCAN® image showing an enlargement of (D) at a 2 micron resolution. The matrix of the diamictite consists of small grains of subrounded to irregularly shaped quartz that are set in a matrix of chlorite with minor apatite, muscovite, and biotite. Muscovite and biotite both appear to be replaced by chlorite. Apatite forms irregular clots that are intergrown with chlorite. Ankerite occurs as small grains interstitial to quartz (DDH KEDD0006, 53.6m).



The textures suggest that this quartz precipitated during chlorite formation. Chlorite also forms relatively thick rims (100-200  $\mu\text{m}$ ) on the margins of clasts in the diamictites. Some of this

clast-riming chlorite replaces biotite. Chlorite is both intergrown with and mantles apatite grains and grain aggregates. Chlorite also overgrows ankerite that occurs as small (20-50  $\mu\text{m}$ ) anhedral crystals throughout the matrix. Copper-sulfide minerals are most commonly intergrown with chlorite suggesting it is temporally related to the dominant period of sulfide mineralization (Figure 5.7). The chlorite-quartz assemblage present in the Fishtie samples is somewhat reminiscent of the late magnesian alteration assemblages present in throughout the Central African Copperbelt (Hitzman et al., 2012) but most prominent in the deposits in the DRC. Chlorite is observed primarily as a peripheral alteration assemblage at the Kamoia deposit (Schmandt et al., in press).

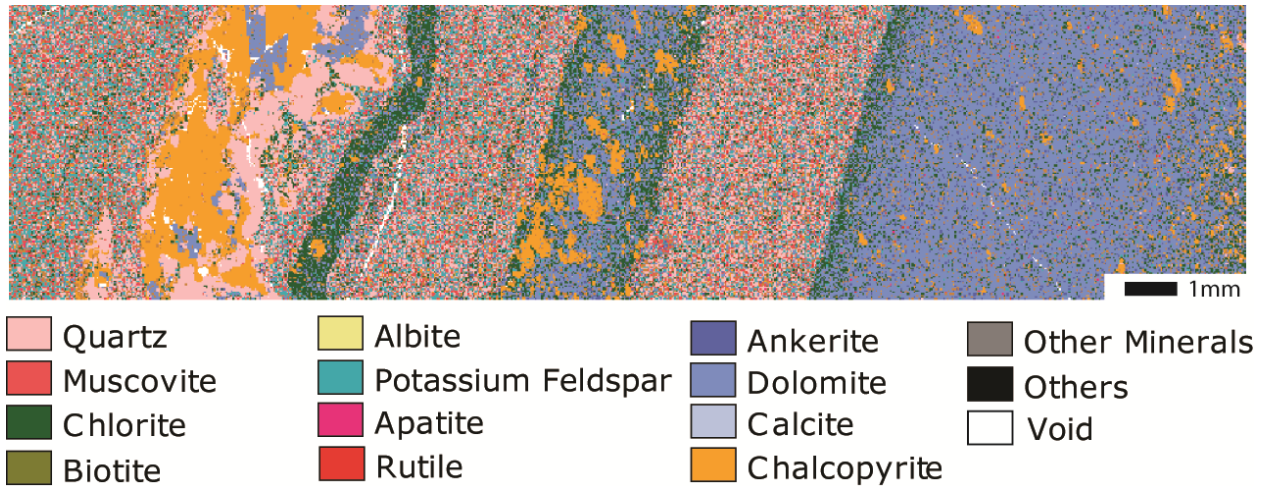


Figure 5.7: Chlorite-mineralized Kakontwe Limestone unit dolomitic siltstone. Sample is composed of alternating dolomite and siliciclastic rich beds, and a bedding parallel vein. Small to large grains of sub to anhedral chalcopyrite are concentrated in beds of dolomite with abundant carbonaceous material. Chalcopyrite is intergrown with chlorite in dolomite rich beds and potassium feldspar in siliciclastic beds (DDH KEDD0085, 85.5m).

## CHAPTER 6

### SULFIDE MINERALIZATION

Rocks in the Fishtie area contain both iron and copper sulfides. Iron sulfides include both pyrite and pyrrhotite. Fine-grained (< 50 microns) pyrite with subrounded shapes suggestive of a framboidal habit occurs throughout the Grand Conglomérat unit but never exceeds 1 volume percent of the rock; such pyrite appears to be more common in Grand Conglomérat unit siltstone beds than in the diamictites. Minor pyrite with a similar habit is also sparingly present in dolomitic siltstones of the Kakontwe Limestone unit. Disseminated pyrrhotite is restricted to the Grand Conglomérat unit diamictites. Pyrrhotite is most common outside of the area that underwent copper sulfide mineralization. While disseminated pyrrhotite and pyrite may be present in the same sample, generally they occur separately. A later generation of coarser grained, generally subhedral pyrite is also present at Fishtie and appears to be temporally associated with copper sulfide precipitation.

Copper sulfides at Fishtie are present from the basement rocks up to the highest levels of the Kakontwe Limestone unit preserved in the area. The amount of copper sulfides appears to be strongly controlled by proximity to normal faults that show evidence of synsedimentary movement. There are also distinct stratigraphic controls. The highest grades of copper contained in hypogene sulfides occur in the central and satellite structural domains within Grand Conglomérat unit diamictites immediately adjacent to normal faults, along the contact between the Grand Conglomérat and Kakontwe Limestone unit, and within dolomitic siltstone layers within the Kakontwe Limestone unit (Figure 6.1).

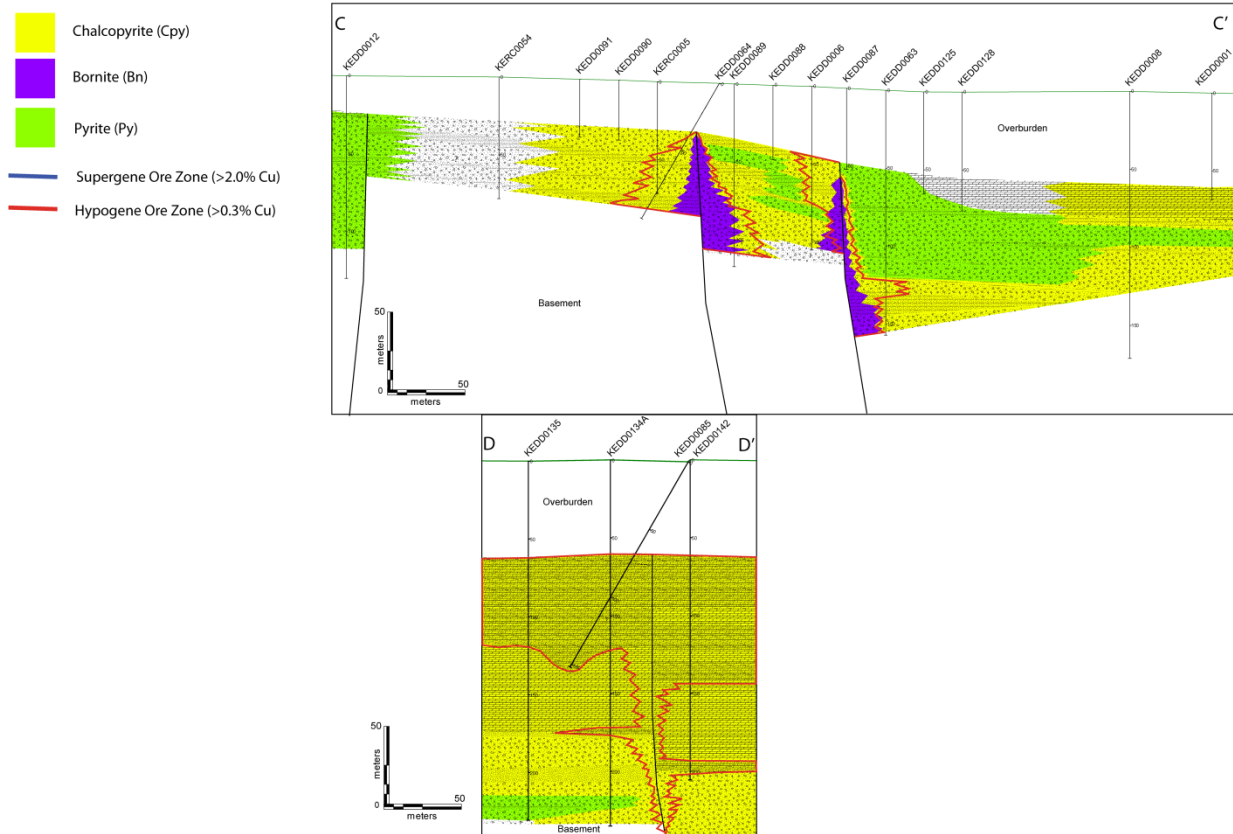


Figure 6.1: Distribution of sulfide minerals in sections C-C' (central structural domain) and D-D' (satellite structural domain). In C-C' bornite is concentrated near the base of the diamictite adjacent to the downthrown side of the northernmost down to the south high angle normal fault and transitions upwards and laterally to chalcopyrite and then pyrite. In D-D' chalcopyrite is the dominant copper sulfide. KEDD denotes diamond drill hole and KERCO denotes reverse circulation drill hole.

Within the central structural domain sulfide mineralization of the Grand Conglomérat unit was focused along the northern of the two south dipping normal faults. Intense mineralization appears to have been restricted to within 50m of the fault plane. Less intense sulfide mineralization also occurred along the southern normal fault that controlled the location of earlier iron formation mineralization (C-C'; Figure 6.1). The presence of significant supergene mineralization within saprolite and soil developed within the weathered Kakontwe Limestone unit suggests these faults may also have resulted in significant mineralization above the Grand

Conglomérat unit. A south side down synsedimentary fault in the satellite structural zone also controlled significant sulfide mineralization primarily at the base of and within the Kakontwe Limestone unit. Sulfides in this zone extend at least 100m laterally from the south dipping normal fault although the geometry of copper-sulfide mineralized zones (D-D'; Figure 6.1) suggests another south dipping normal fault north of the currently drilled area may have been the primary conduit for hydrothermal fluids. Such a fault, if present, would make the fault pattern in this structural domain similar to that in the central structural domain.

The Fishtie deposit contains a simple suite of sulfide minerals. Chalcopyrite is the dominant copper-sulfide. Bornite is present in higher-grade zones though it is the dominant sulfide only locally. Pyrite occurs throughout the Fishtie area but is most common on the fringes of the chalcopyrite zone. Pyrrhotite is restricted to the Grand Conglomérat unit. Assay values and whole rock geochemistry indicate that the deposit contains geochemically anomalous cobalt. Highest cobalt grades occur within high-grade copper zones. Sparse carrollite was observed in late carbonate-copper sulfide veins in the Kakontwe Limestone unit. The available geochemical data does not suggest that Fishtie contains significant silver or that there is a well-developed zinc-lead fringe to the copper system as observed in the Kamoia deposit (Schmandt et al., in press).

Copper sulfide mineralogy is zoned at Fishtie. In the central structural domain there is a clear trend from a bornite-rich assemblage at the base of the Grand Conglomérat unit adjacent to the normal fault upwards to a more chalcopyrite-rich assemblage higher in the unit. Bornite reappears at the top of the Grand Conglomérat unit at the contact with the Kakontwe Limestone unit though it is subordinate to chalcopyrite. Though poorly defined by current drilling there appears to be a lateral zonation from more bornite-rich assemblages adjacent to the northernmost

normal fault laterally to chalcopyrite- and finally pyrite-rich assemblages both to the north and south in the Grand Conglomérat unit. Similar, though poorly defined, vertical and lateral zonation of sulfide minerals appears to occur in the satellite structural domain. Copper sulfides in basement rocks at Fishtie are almost exclusively chalcopyrite. In mixed sulfide assemblages, bornite is commonly observed to replace chalcopyrite while chalcopyrite generally replaces pyrite.

Within the Grand Conglomérat unit sulfides occur as very fine-grained (<50 microns) disseminations throughout the diamictite matrix and as coarse-grained crystals on clast margins (Figure 6.2a). Sulfides are more prevalent in the diamictites of the Grand Conglomérat unit than in siltstone layers. As at Kamoia (Schmandt et al., in press) the largest volume of sulfides is present as disseminated grains in the diamictite matrix. Fine-grained sulfides are generally anhedral and equi-dimensional.

Sulfides on clast rims are generally coarse grained and anhedral (Figure 6.2b). Sulfide mineral aggregates sometimes exceed 3 cm in diameter. The sulfides are intergrown and locally appear to replace biotite, chlorite, muscovite, potassium feldspar, and carbonate minerals (dolomite and ankerite) (Figure 6.2c). Sulfide mineral assemblages in an individual sample are generally similar in both fine-grained disseminated sulfides and coarse-grained clast rim sulfides similar to what is observed with other hydrothermal mineral assemblages. These relationships suggest simultaneous precipitation of both fine- and coarse-grained sulfides.

Quartz-carbonate-(sulfide) veins up to 15 centimeters in width occur sparingly in the Grand Conglomérat unit. Thin quartz-carbonate veins (1-5 cm) are most abundant and are commonly barren. Sulfide-bearing veins do not constitute an economically significant portion of the resource in the Grand Conglomérat unit at Fishtie.

Copper sulfides in the Kakontwe Limestone unit occur primarily as concentrations of disseminated sulfides along bedding planes in dolomitic siltstone beds and less commonly as disseminated grains within massive dolostones. Highly carbonaceous beds may contain abundant sulfides (up to 30 volume percent locally; Figure 6.2d) that appear megascopically as semi-massive sulfide bodies. Sulfides in such beds appear to be intergrown with hydrothermal potassium feldspar. The Kakontwe Limestone unit also contains quartz-dolomite-sulfide veins in the satellite portion of the deposit. These veins may be up to 0.3 m wide. Veins appear to have both subhorizontal orientations peneconcordant with bedding planes and subvertical orientations that probably parallel normal faults. These veins contain dominantly chalcopyrite with lesser bornite and pyrite and locally carrollite; they represent the most significant zones of cobalt within the deposit.

Sulfide minerals are sparse in the basement rocks. Pyrite and pyrrhotite occur as fine to coarse grains with coarse-grained muscovite that forms the dominant metamorphic foliation. Copper sulfides occur primarily as coarse-grained disseminations in quartz-muscovite schist and in quartz-sulfide veins cutting schist and quartzite. Chalcopyrite is the dominant mineral. Copper sulfides within the schist are generally intergrown with coarse-grained, unfoliated aggregates of either muscovite and/or chlorite (Figure 6.2e).

Two main episodes of sulfide precipitation occurred at the Fishtie copper deposit. The earliest was formation of diagenetic pyrite in the siltstone units of the Grand Conglomérat and to a lesser extent in the diamictite matrix. It is unclear if pyrrhotite was also deposited during or shortly after diagenesis or whether it formed as a result of metamorphism of the sequence during the Lufilian event. Copper sulfide and ore stage pyrite mineralization occurred after iron formation mineralization and affected both the Grand Conglomérat and Kakontwe Limestone

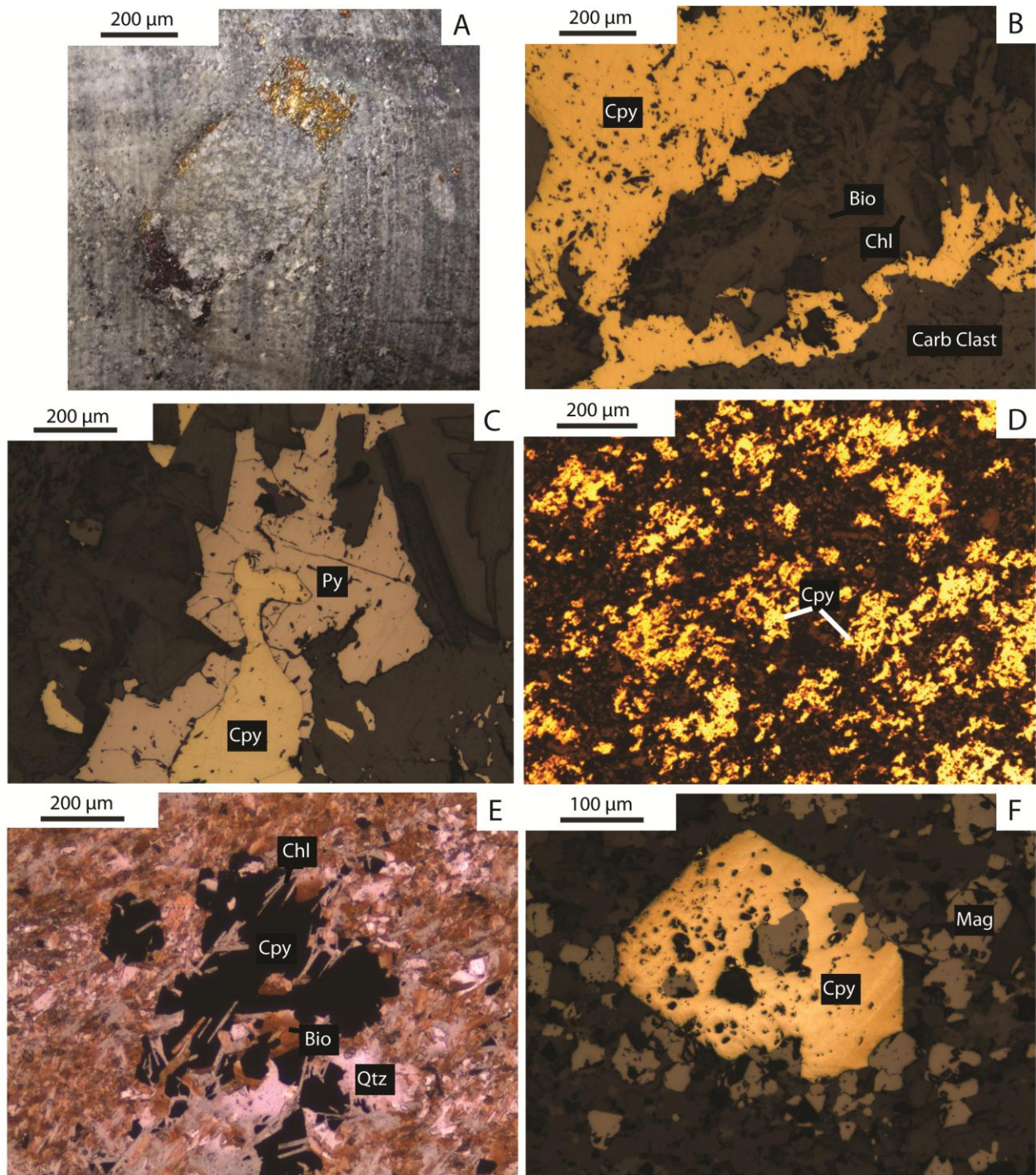
units. Ore stage pyrite is distinguished by its coarser grain size relative to diagenetic pyrite. It occurs within in clast rims within the diamictite and as grains overgrowing magnetite in iron formation.

The age of copper mineralization relative to other hydrothermal mineralization at Fishtie is difficult to precisely constrain. Chalcopyrite clearly overgrows and replaces magnetite in the iron formation (Figure 6.2f). It is intergrown with potassium feldspar within dolomitic siltstones of the Kakontwe Limestone unit suggesting it is, at least in part, age equivalent with the potassic mineralization event. Bornite, chalcopyrite, and pyrite are intergrown with or replace muscovite and biotite within coarse mineral rims to clasts in the Grand Conglomérat. Copper sulfides are also intergrown with late chlorite in both the matrix of the diamictite and in coarse mineral rims indicating a relatively late period of sulfide mineralization. Thus, mineral textures suggest copper sulfide mineralization extending from the period of potassic mineralization through the period of chlorite mineralization. The behavior of sulfide minerals during metamorphism is poorly constrained due to the general lack of metamorphic textures at Fishtie in rocks of the Nguba Group sequence.

### **6.1 Supergene Mineralization**

Though not investigated as part of this study, the Fishtie deposit contains a significant amount of oxide and mixed oxide-sulfide material. The supergene-mineralized zone occurs within saprolites developed at the base of the weathering zone. The highest-grade portions of this supergene body occur within the central structural domain between the two south dipping normal faults (Figure 6.1) and form a 1m to 30m thick zone approximately 450m long (east-west) and 125m wide (north-south). This zone appears to approximately correspond to the upper contact of the Grand Conglomérat unit with the Kakontwe Limestone unit.

Figure 6.2: Sulfide textures at the Fishtie copper deposit. (A) Quartzite clast in the Grand Conglomérat unit with a discontinuous rim of sulfides. Intergrown bornite, quartz, and chlorite (top) and chalcopyrite, quartz, and chlorite (bottom) appear to grow in pressure shadows around the clast (KEDD-008, 112.6m). (B) Reflected light photomicrograph of a coarse mineral rim on a carbonate clast consisting of intergrown chalcopyrite, biotite, and chlorite; the biotite is replaced by chlorite (DDH KEDD0017, 118m). (C) Reflected light photomicrograph of chalcopyrite intergrowth with pyrite in a chlorite-rich clast rim (DDH KEDD0062, 101.7). (D) Reflected light photomicrograph of chalcopyrite in a carbonaceous interval of dolomitic siltstone within in the Kakontwe Limestone unit (DDH KEDD0136, 124m). (E) Plane-polarized photomicrograph of chalcopyrite intergrowth with chlorite and biotite in basement quartz-muscovite schist (DDH KEDD0076, 175.6m). (F) Reflected light photomicrograph of chalcopyrite overgrowths on magnetite in the iron formation within the Grand Conglomérat unit (DDH KEDD0032, 79.2m).



A more weakly developed supergene mineralized zone is present at the base of the weathering zones within the Kakontwe Limestone unit in the satellite structural zone. Minor

amounts of supergene malachite and chalcocite are found throughout the entire sequence intersected by drilling in areas adjacent to normal faults.

The supergene mineralized zones consist of brown to reddish fine-grained to almost conglomeratic saprolite composed of limonite-goethite, clay, copper oxide and carbonate minerals (malachite >> azurite), and chalcocite with remnant wall rock carbonate minerals and minor quartz. Grades over one meter in this material may exceed 4.5% Cu.

## **6.2 Paragenetic sequence of mineralization**

Diagenesis predated hydrothermal mineralization and resulted in precipitation of quartz and carbonate minerals during burial at shallow depths (<2 km) and low temperatures (~100°C). These conditions could also have led to formation of chlorite from clay and feldspar overgrowths on detrital feldspar and quartz (Morad et al., 2000; Tucker et al., 2011). Diagenesis of the carbonate rocks of the Kakontwe Limestone unit likely began during deposition and resulted in recrystallization of carbonate grains and precipitation of carbonate cement.

End-member mineralogy types at Fishtie indicates three main hydrothermal mineralization episodes (iron oxide-ankerite-apatite (iron formation), potassic, and chlorite) affected the rocks.

Development of the iron formation followed or was partly synchronous with diagenesis, and was characterized by small to moderate sized sub- to euhedral magnetite crystals intergrown with ankerite and chlorite which were in turn overprinted by apatite. Iron formation is concentrated in the siltstone units of the Grand Conglomérat and to a lesser extent in diamictite matrix proximal to faults. Iron oxide-ankerite-apatite mineralization in the diamictite matrix occurred primarily stratigraphically above intense iron formation mineralization in siltstone units.

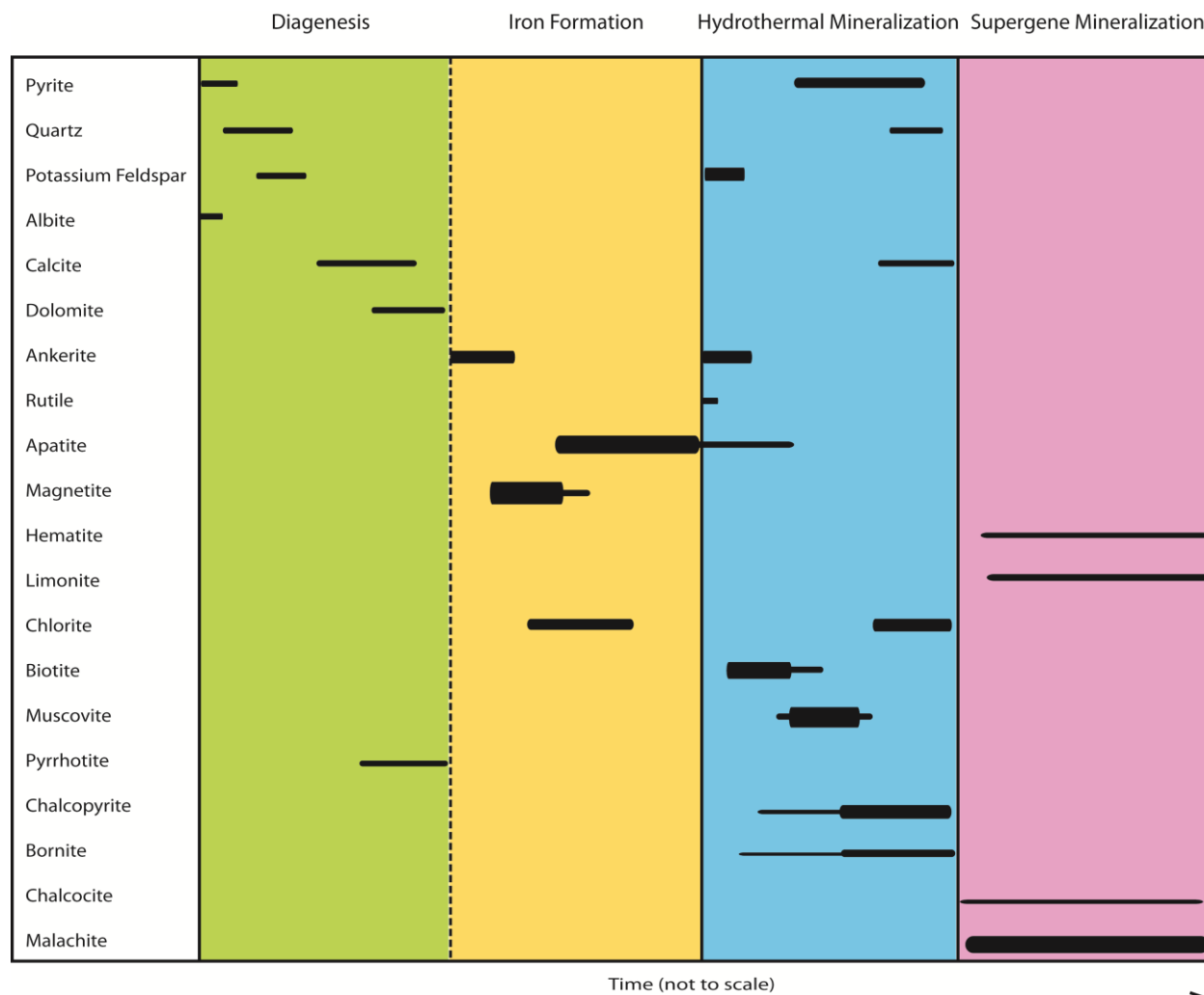


Figure 6.3: Paragenetic sequence of minerals during diagenesis, precipitation of iron formation, hydrothermal mineralization, and supergene mineralization at the Fishtie copper deposit.

Mineral assemblages and textures indicate iron oxide-ankerite-apatite mineralization was followed by potassic and chlorite mineralization (Figure 6.3). Potassic mineralization occurred ubiquitously throughout the deposit area. It is characterized by increased size and abundance of potassium feldspar, biotite, and muscovite. Potassium feldspar mineralization occurred first and was at least partly synchronous with biotite mineralization that was followed by a pervasive muscovite mineralization episode. This mineral assemblage is common in deposits of the Zambian Copperbelt (Selley et al., 2005). However, due to the large area affected by potassic

mineralization it does not serve as a primary vector to ore. Chlorite mineralization initiated in the waning stages of potassic mineralization and was characterized by increased abundance of chlorite and intergrown quartz.

Copper sulfide mineralization appears to have occurred during both potassic and chlorite mineralization. Supergene enrichment with the formation of malachite and lesser chalcocite within the Kakontwe Limestone unit near the contact with the Grand Conglomérat occurred during weathering.

## CHAPTER 7

### CARBON AND OXYGEN ISOTOPES OF ALTERED ROCKS

The isotopic composition of carbonate minerals within the iron formation, altered and mineralized samples of the Kakontwe Limestone unit, and carbonate-sulfide veins was investigated to better understand the process of alteration and mineralization at Fishtie. Ankerite in the iron formation has carbon and isotopic values that are approximately six per mil lighter than unaltered carbonates in the overlying Kakontwe Limestone unit (Figure 3.9; Appendix F). While isotopically lighter values would be expected within the glacial diamictites relative to the overlying cap carbonate rocks (Halverson et al., 2010), these extremely light values are more likely due to infiltration of hydrothermal fluids.

The least altered dolomite and limestone in the Kakontwe Limestone unit have  $\delta^{18}\text{O}_{\text{SMOW}}$  and  $\delta^{13}\text{C}_{\text{VPDB}}$  values averaging 26.3 ‰ and 2.5 ‰ respectively (Figure 3.10; Appendix F). Kakontwe carbonate rocks from mineralized areas and those containing hydrothermal potassium feldspar display a range of values that overlap those of the unaltered samples but extend to lighter carbon and oxygen values (Figure 3.9). With the exception of one outlier with a carbon isotopic value of 8.5‰, most of the samples have carbon isotopic values similar to those of the unaltered carbonates. However, oxygen isotopic values display a marked trend towards lighter isotopic values.

Carbonate minerals in sulfide-bearing veins display a more dramatic shift to lighter values of carbon and especially oxygen isotopic values. Oxygen isotopic values can be significantly affected at lower water to rock ratios than carbon values (Sverjensky, 1981; Zheng and Hoefs, 1993) and are commonly used as an indicator of post-depositional alteration (Brand and Veizer, 1980; Derry et al., 1992). Such hydrothermal modification of isotopic values was

recognized in the Zambian Copperbelt by Annels (1989) and Sweeney and Binda (1989). Light  $\delta^{13}\text{C}$  and  $\delta^{18}\text{O}$  values can also result from temperature effects during hydrothermal alteration, due to the incorporation into secondary carbonates of isotopically light C and O produced by oxidation of organic matter (in situ or mobile hydrocarbons) during either low-temperature ( $\sim 60^\circ\text{--}80^\circ\text{C}$ ) bacterial sulfate reduction or high temperature ( $>100^\circ\text{C}$ ) thermochemical sulfate reduction (Ohmoto and Goldhaber, 1997).

## CHAPTER 8

### SULFUR ISOTOPES

Isotopic values of apparently diagenetic and hydrothermal sulfides were measured to constrain sulfur sources at the Fishtie copper deposit (Figure 8.1; Appendix G). The range of isotopic values present in the sulfide assemblages at Fishtie indicates that there was no significant homogenization of isotopic values during the Lufilian metamorphic event.

Fine grained, disseminated pyrite (n=3) from within Grand Conglomérat unit siltstones both distal to and within the ore zone have  $\delta^{34}\text{S}$  values near +11‰. These values overlap those known from Neoproterozoic sedimentary pyrites from other areas in the world (Strauss, 1997). However, diagenetic pyrite from the Zambian Copperbelt commonly has  $\delta^{34}\text{S}$  values lighter than 0‰ (McGowen et al., 2003) and framboidal diagenetic pyrite in siltstone layers within the Grand Conglomérat at the Kamoia deposit also display light values from -11 to +3‰ (Schmandt et al., in press). The relatively heavy sulfur isotopic values of apparently diagenetic pyrite at Fishtie indicate replacement of early framboidal pyrite by ore stage pyrite.

Ore stage pyrite and chalcopyrite at Fishtie display relatively heavy sulfur isotopic values. Chalcopyrite from clast rims and as disseminated grains within in the matrix of Grand Conglomérat unit diamictites from within the main ore body in the central structural domain displays  $\delta^{34}\text{S}$  values that range from 7 to 13‰ with an average of 9‰. Chalcopyrite from clast rims and as disseminations in the Grand Conglomérat unit diamictite matrix in the satellite structural domain displays slightly lighter  $\delta^{34}\text{S}$  values of 10 to 11 ‰. Bornite and chalcopyrite from small quartz-carbonate veins in the Grand Conglomérat unit display  $\delta^{34}\text{S}$  values that range from 3 to 6‰ with an average of 4‰.

Sulfides in the Kakontwe Limestone unit display significantly heavier isotopic values than those within the Grand Conglomérat. Ore stage cubic pyrite from Kakontwe Limestone unit dolomitic siltstones in the satellite structural domain has  $\delta^{34}\text{S}$  values that range from 15 to 26 ‰ with an average value of 20‰. Chalcopyrite from the same portion of the deposit has  $\delta^{34}\text{S}$  values that range from 14 to 25‰ with an average value of 19‰. Chalcopyrite in quartz-carbonate veins in Kakontwe Limestone unit from the satellite structural domain has  $\delta^{34}\text{S}$  values that range from 13-19‰ with an average value of 16‰ (Figure 8.1).

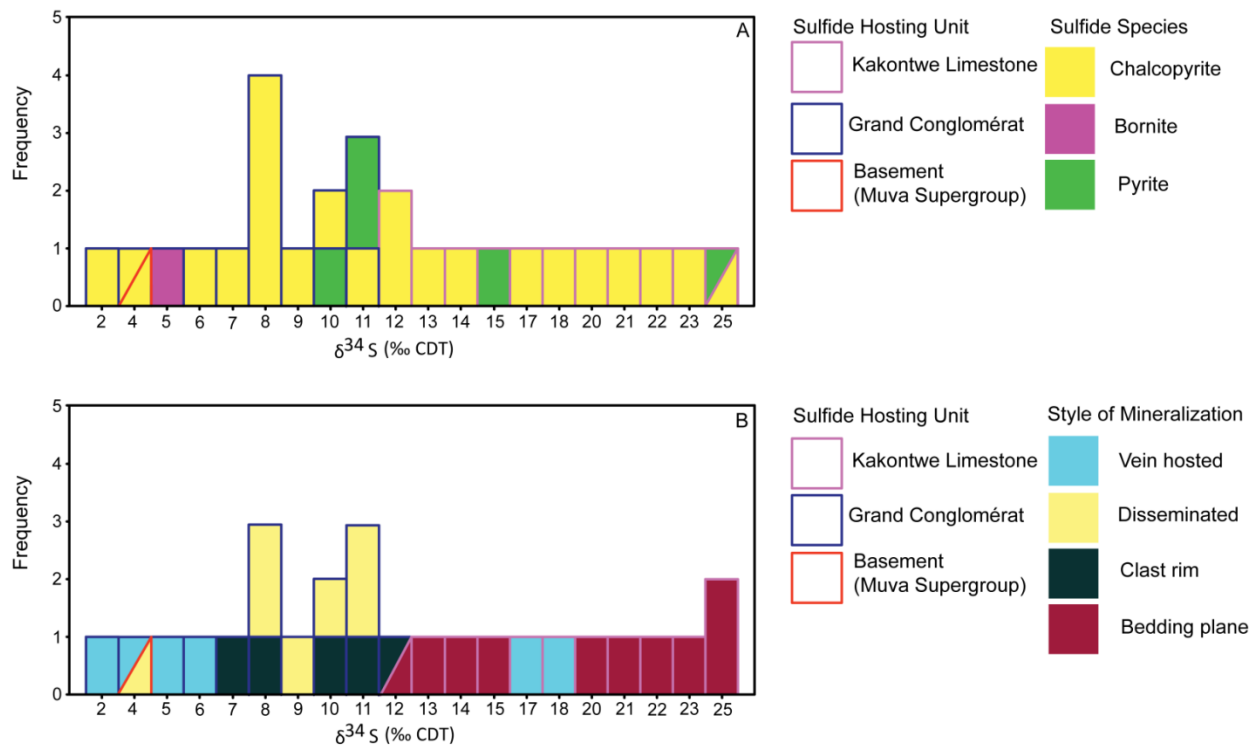


Figure 8.1: Histograms of sulfur isotopic values. (A) Sulfur isotopic values of sulfides species (solid color) as a function of host lithology (outline color). Chalcopyrite and pyrite in Kakontwe Limestone units have consistently higher sulfur isotopic values than sulfides in the underlying Grand Conglomérat unit with relatively little overlap between the two. (B) Sulfur isotopic values as a function of the style of mineralization (solid color) and host lithology (outline color). The style of mineralization (vein, disseminated, clast rim, along bedding planes) does not appear to affect the sulfur isotopic composition of sulfides.

Similar trends to heavier sulfur isotopic values with increasing stratigraphic height in the stratigraphic sequence have been noted in several deposits in the Zambian Copperbelt (Selley et al., 2005). A trend to increasing sulfur isotopic values with stratigraphic height has also been observed in the Kamoia deposit (Schmandt et al., in press). The reasons for these trends are unclear.

The isotopic values of copper sulfides and coeval pyrite at Fishtie suggests that these sulfides did not simply derive their reduced sulfur from diagenetic sulfides as has been suggested for the majority of sulfides at Kamoia (Schmandt et al., in press). Instead, much of the reduced sulfur in the copper sulfides must have come from reduction of seawater sulfate. The  $\delta^{34}\text{S}$  sulfur isotopic composition of seawater during the Neoproterozoic at the onset of the Sturtian glaciation is estimated to have been between +15 and +25 ‰ CDT (Claypool et al., 1980; Strauss et al., 2001). Values of anhydrite from within the Roan Group throughout the Central African Copperbelt have  $\delta^{34}\text{S}$  values that average approximately +17‰ (Selley et al., 2005) while sulfate within the Mwashya Subgroup immediately below the Grand Conglomérat at Kamoia average +20‰ (Schmandt et al., in press). The values of the copper sulfides and ore stage pyrite at Fishtie suggest isotopic fractionation ( $\Delta_{\text{SO}_4\text{-sulfides}}$ ) values of 0 to approximately 12 ‰.

## CHAPTER 9

### DISCUSSION

The Fishtie deposit represents a substantial concentration of copper with geochemically anomalous cobalt in rocks at the base of the Nguba Group. Its stratigraphic position differs from most of the deposits within the Central African Copperbelt. It is at a similar stratigraphic position to the recently discovered giant Kamao deposit on the western edge of the Katangan basin (Schmandt et al., in press) where sulfides occur at the base of the Grand Conglomérat as well as to the Lonshi deposit immediately north in the southeastern portion of the Zambian Copperbelt where sulfides are located primarily at the upper contact of the Grand Conglomérat with the overlying Kakontwe Limestone (Hitzman et al., 2012).

#### **9.1 Stratigraphic and Structural Architecture**

Mineralization at Fishtie appears to have been largely controlled by high-angle normal faults that show evidence of having had synsedimentary movement. Not all normal faults at Fishtie appear to have formed conduits for hydrothermal fluids. Iron formation was developed adjacent to several of the faults at Fishtie. However, later precipitated sulfides are more abundant on other, subparallel normal faults. These relationships indicate that the volumes of hydrothermal fluids utilizing individual faults within the normal fault array at Fishtie varied through time.

Unlike Kamao where the Grand Conglomérat lies above a sequence of apparently permeable sandstones that pinch out away from the basin margin (Schmandt et al., in press), the Grand Conglomérat unit at Fishtie sits directly above relatively impermeable basement schists and quartzites. Thus, hydrothermal fluids at Fishtie could gain entry to the Grand Conglomérat sequence only along structural zones rather than being able to infiltrate upwards from a porous

and permeable sequence below the Grand Conglomérat as at Kamoia. These relationships undoubtedly controlled the geometry of the different orebodies. At Fishtie copper sulfides occur in relatively narrow zones adjacent to normal faults while at Kamoia a laterally extensive blanket of mineralized rock was formed that was zoned upwards from the basal surface of the Grand Conglomérat.

Fishtie is similar to Lonshi where hydrothermal fluids penetrated through the Grand Conglomérat and spread out along the upper contact of the unit with the Kakontwe Limestone. Hydrothermal fluids were able to penetrate the Grand Conglomérat at both Fishtie and Lonshi due to its relative thinness (~150m) compared to the hundreds of meters of diamictite present at Kamoia.

Kamoia is located adjacent to the western margin of the main Katangan basin. Lonshi sits on the edge of a major basin flanking the eastern edge of the Zambian Copperbelt that appears to be a sub-basin to the main Katangan basin (Hitzman et al., 2012). The Fishtie deposit occurs within the Lusale basin that appears to be an outlier to the sub-basin hosting Lonshi. The apparently relatively small size of the Lusale basin may account for the smaller size of the Fishtie deposit (e.g. 55 Mt of 1.04% Cu) relative to Kamoia (810 Mt of 2.69% Cu) or Lonshi (42 Mt of 3.6% Cu) (Hitzman et al., 2012).

## **9.2 Rapitan Iron Formation**

The Cryogenian-Ediacaran interval of the Neoproterozoic marks the return of large-scale iron formations, termed Rapitan-type, after an absence of over one billion years (Klein and Buekes, 1993). Rapitan-type iron formations of Sturtian age are recognized at eight locations around the world and a ninth locality is likely Sturtian in age. The known Sturtian age localities are in the Damara Belt of Namibia (Badenhorst, 1988; Clifford, 2008), the southern Namibia-South Africa border region (Macdonald et al., 2010), the MacKenzie Mountains of northwest

Canada (Gross, 1965; Young, 1976; Yeo, 1981; Klein and Beukes, 1993), southern California (Prave, 1999; Corsetti and Kaufman, 2003), the Ural Mountains of Russia (Chumukov, 2007), South Australia (Preiss, 1987; Lottermoser and Ashley, 2000), southern China (Jiafu et al, 1987; Wang and Li, 2003), and the Tuva area near the border of Russia and Mongolia (Ilyin, 2009; Macdonald et al., 2009). The major iron formations within the Jadcadigo Group of the Urucum district at Corumbá along the Bolivia-Brazil border may be Sturtian in age (Dorr, 1945; Urban et al., 1992; Trompette et al., 1998; Klein and Ladeira, 2004).

Although ironstones have long been known within the Central African Copperbelt (Cornet, 1910), they have not previously been recognized as correlatives with other Neoproterozoic Rapitan-type iron formation. Most ironstones in the Central African Copperbelt occur within rocks of the Mwashya Subgroup beneath the Grand Conglomérat (Cornet, 1910; Jamotte, 1950; Master and Wendorff, 2011). Iron formation at Fishtie occurs within, and is most prominent near the top of, the Grand Conglomérat unit. Iron formation is recognized at a similar stratigraphic position to that at Fishtie within the Grand Conglomérat in northwestern Botswana (Hitzman, pers. comm., 2013).

The iron formation at Fishtie consists of magnetite, ankerite, apatite, and quartz with various layers having one or more of these minerals as the dominant constituents. The absence of iron formation clasts in diamictite beds overlying iron formation layers together with the presence of disseminated magnetite, ankerite, and apatite in diamictite beds adjacent to the iron formation suggests the iron formation was formed by precipitation the magnetite-ankerite-apatite assemblage within siltstones postdating deposition of the Grand Conglomérat unit. This is unlike most of the Rapitan-type iron formations that appear to have formed as chemical sediments. The Fishtie iron formation differs from most other Rapitan-type iron formations in being composed

almost exclusively of magnetite while most other examples are hematite-rich. The magnetite could have formed from hematite during the Lufilian metamorphic event.

Neoproterozoic iron formations occur both immediately beneath and within glacially associated diamictites suggesting an association with glaciation. Like many other Rapitan-type iron formations, those at Fishtie display rapid thickness changes over short lateral distances. At Fishtie the iron formation is clearly related to normal faults. Thus, it is similar to other Rapitan-type iron formations that have been interpreted to have formed in either closed rift basins or on reactivated continental margins (Trompette et al., 1998; Young, 2002).

The high phosphorous content of the Fishtie iron formation conforms to values observed in many other Neoproterozoic iron formations (Bekker et al., 2010). Such high values may be related to the higher phosphorous contents of contemporaneous seawater as reflected by the numerous sedimentary phosphorite deposits of this age or they could be due to input of hydrothermal fluids. The REE pattern for the Fishtie iron formation, like that of other Neoproterozoic iron formations, does not display a positive Eu anomaly and has high Ce values due to the abundance of apatite.

The location of the Fishtie iron formation within a graben and its “replacive” nature suggests it formed from hydrothermal fluids rather than from large-scale iron oxide precipitation due to fluctuating seawater chemistry. Formation of Neoproterozoic iron formation due to hydrothermal processes (Yeo, 1981, 1986) rather than changes in seawater chemistry due to widespread glaciation (Kirschvink, 1992; Klein and Beukes, 1993; Hoffman et al., 1998b) remains a contentious issue (Young, 2002, Macdonald et al., 2010b). Iron formation requires anoxic waters with a S:Fe ratio of  $<2$  to enable reduced iron to be carried in solution without being precipitated as pyrite (Canfield, 2004). The presence of anomalous barium in the iron

formation suggests the hydrothermal fluid did not contain sulfate. At Fishtie, and other Rapitan-type iron formation localities, sulfur-poor hydrothermal fluids mixed with oxygenated water upon entry into the ocean or with pore fluids in porous and permeable sediments probably located near the sea floor. These oxygenated waters either lacked sulfate, perhaps due to diminished sulfate input from continents during glaciation (Canfield et al., 2008) following potentially very high levels of ocean sulfate in the time immediately preceding the Sturtian (Hitzman et al., 2010), or because conditions were not conducive for bacterial sulfate reduction, again possibly due to extensive ice cover (Macdonald et al., 2010b).

Debouching of early iron-rich hydrothermal fluids did result in extensive pyrite formation in some portions of the Katangan basin. The Kamoia deposit lacks iron formation but contains abundant diagenetic pyrite in siltstones that are lithologically equivalent to the siltstones hosting the iron formation at Fishtie (Schmandt et al., in press). Whether Kamoia contains abundant pyrite due to a difference in hydrothermal fluid chemistry or due to local variations in seawater chemistry is unknown but has important implications for a better understanding of iron-rich hydrothermal systems in the Neoproterozoic.

### **9.3 Potassium Feldspar and Phyllosilicate Mineralization**

Hydrothermal mineralization postdating the iron formation is widely developed in both the Grand Conglomérat and Kakontwe Limestone units at Fishtie. Early diagenetic albite growth, as noted in the Zambian Copperbelt (Woodhead, 2013), may have occurred at Fishtie although it is commonly difficult to definitively assign a paragenetic age to the relatively sparse albite present in the Grand Conglomérat unit. The widespread calcium-magnesium metasomatism described from the Zambian Copperbelt by Selley et al. (2005) appears to be absent at Fishtie with the possible exception of dolomitization within the Kakontwe Limestone unit. There is little to no phlogopite in argillaceous rocks at Fishtie and anhydrite is apparently

absent in all units.

Potassic mineralization was likely the earliest phase of hydrothermal mineralization postdating iron formation. It resulted in widespread precipitation of potassium feldspar, possibly together with biotite, primarily within silty rocks both within both the Grand Conglomérat and Kakontwe Limestone units. Both potassium feldspar and biotite, together with quartz and ankerite, are commonly found in mineral rims to clasts within the diamictites.

Similar styles of potassic mineralization have been noted throughout the Central African Copperbelt, particularly in Roan Group rocks of the Zambian Copperbelt (Darnely, 1960; Selley et al., 2005). As noted by Woodhead (2013) in the Zambian Copperbelt, it is difficult to correlate potassic mineralization at Fishtie directly with copper sulfide precipitation. Replacive potassium feldspar and biotite with similar textures to those at Fishtie are present in the basal portion of the Grand Conglomérat at Kamoia (Schmandt et al., in press).

Grand Conglomérat unit diamictites at Fishtie locally contain abundant muscovite. The distribution of such zones is not well defined, though they appear to be spatially associated with the presence of increased amounts of copper sulfides suggesting muscovite mineralization was associated with copper mineralization. Muscovite-rich zones are relatively poor in carbonate minerals and commonly contain only sparse ankerite. Muscovite is relatively rare in mineral rims to clasts in diamictites, similar to Kamoia (Schmandt et al., in press).

Muscovite in the muscovite-rich zones at Fishtie appears to have replaced potassium feldspar and to a lesser degree biotite. Normal seawater, or introduction or production of an in-situ low pH fluid, could account for the instability of potassium feldspar in the rocks at Fishtie. Such relatively acidic conditions could have been generated during sulfide precipitation by the liberation of  $H^+$  during the interaction of a metal-bearing fluid with  $H_2S$ . However, since

potassium feldspar and/or carbonate are major constituents of many Zambian Copperbelt ores (Selley et al., 2005) and are present in some mineralized rocks at Fishtie it is unlikely that sulfide deposition alone lowered the pH sufficiently to destabilize these minerals.

Anomalously abundant sericite (fine-grained muscovite) has also been noted in the Zambian Copperbelt at several arenite-hosted orebodies (e.g. Chibuluma, Mufulira: Darnley, 1960; Nchanga-Chingola: McGowan et al., 2003). The geometries of the sericite-rich deposits in the Zambian Copperbelt are comparable to physical hydrocarbon traps (Selley et al., 2005). The position of the Fishtie orebodies adjacent to normal faults could also have formed physical traps with the Kakontwe Limestone unit serving as the cap rock. The low  $\delta^{13}\text{C}$  values of carbonates associated with altered and mineralized rocks at Fishtie support the possibility of the former presence of organic matter such as liquid or gaseous hydrocarbons. Thus, as noted by Selley et al. (2005), it is possible that muscovite mineralization was due to the presence of sulfuric acid generated from the reaction of excess  $\text{H}_2\text{S}$  in sour gas with an oxidized ore fluid. Alternatively, release of  $\text{CO}_2$  gas during the destruction of carbonate cements within the host rocks could have contributed to acidity at the site of ore deposition (Machel, 1989).

Increased amounts of chlorite at Fishtie occur both with iron formation and within diamictites and siltstones of the Grand Conglomérat unit adjacent to normal faults (Figure 5.1). Chlorite in the iron formation is interpreted to have been precipitated during its formation. Chlorite in the fault-related mineralized zones replaces biotite and appears to replace potassium feldspar, albite, and muscovite in intensely mineralization zones. The distribution of this chlorite mineralization has a direct spatial relationship to zones with enhanced copper grades. Chlorite is also noted in sulfide-bearing quartz veins in the basement and in some sulfide-bearing dolomite veins in the Kakontwe Limestone unit. Thus, it appears that chlorite mineralization at Fishtie is

temporally associated with at least a portion of copper sulfide precipitation.

While chlorite is pervasive throughout the stratigraphic sequence at Kamoia it commonly forms the exterior layer on diamictite clast rims indicating it is paragenetically late relative to potassic alteration, silicification, and most sulfide precipitation (Schmandt et al., in press). Chlorite is commonly associated with mineralized assemblages in deposits of the Congolese portion of the Central African Copperbelt and is taken as evidence of magnesian alteration with copper mineralization (Muechez et al., 2008; El Desouky et al. 2009; Hitzman et al., 2012). In both the Congolese deposits and at Fishtie it appears that silicification accompanied chlorite mineralization. Thus, Fishtie shares more similarities in terms of concurrent late chlorite mineralization and copper sulfide mineralization with the Congolese Copperbelt deposits than Kamoia.

#### **9.4 Post Iron Formation Hydrothermal Sulfide Mineralization**

Diagenetic iron sulfides appear to have been relatively uncommon in the rocks at Fishtie. Although grains of pyrite and pyrrhotite with apparent framboidal or recrystallized framboidal textures are present they are rare. The sparse isotopic data available for these sulfides indicates they have isotopically heavy  $\delta^{34}\text{S}$  values unlike those for diagenetic sulfides elsewhere in the Central African Copperbelt.

Copper-sulfides at Fishtie occur from the basement to the top of the preserved Kakontwe Limestone unit. Copper sulfides are concentrated along and adjacent to normal faults and display a gross zonation vertically within the sequence and laterally from the faults from bornite to chalcopyrite to pyrite typical of sedimentary rock-hosted stratiform copper deposits (Hitzman et al., 2005). This suggests that the ore fluids at Fishtie were oxidized, similar to those elsewhere in the Central African Copperbelt.

Sulfides in the Fishtie deposit occur in veins in all of the stratigraphic units and within mineral rims to clasts in the diamictites but are most abundant as disseminations within the Grand Conglomérat unit and in dolomitic siltstones of the Kakontwe Limestone unit. In the dolomitic siltstones of the Kakontwe unit a clear relationship between abundant carbonaceous material and sulfide abundance is observed. The reason for sulfide precipitation in the rocks of the Grand Conglomérat unit is less clear. Neither carbonaceous matter nor diagenetic pyrite appears to have been common in these rocks. The muscovite mineralization together with the relatively light carbon isotopic values of sulfide-related carbonate minerals in the Grand Conglomérat unit suggest that mobile hydrocarbons, such as natural gas, may have been present and served as a reductant as has been suggested for a number of deposits in the Central African Copperbelt (Selley et al., 2005; Hitzman et al., 2012).

Sulfides at Fishtie display a relatively restricted set of sulfur isotopic values compared to many deposits in the Central African Copperbelt (Dechow and Jensen, 1965; Annels, 1989; Hoy and Ohmoto, 1989; Sweeny and Binda, 1989; McGowan et al., 2006; Cailteux et al., 2005; Lerouge et al., 2005, Selley et al., 2005; Haest et al., 2005; Muchez et al., 2010). The heterogeneity of sulfur isotopic values in these deposits is generally attributed to reduction of seawater sulfate to sulfide through both thermochemical sulfate reduction and bacterial sulfate reduction over a long period of time (Selley et al., 2005). Sulfur isotopic values for sulfides at Fishtie are generally heavy with values ranging from +3 to +19‰ and most values being above 10‰. Sulfides at Fishtie, as at Kamoia (Schmandt et al., in press), display a general trend to heavier values with increasing stratigraphic height and through time. Similar trends have been noted in the Zambian Copperbelt by Dechow and Jensen (1965), Annels (1989), and Sweeney and Binda (1989).

The sulfur isotopic values of sulfides at Fishtie are in stark contrast to those at Kamoa where copper sulfides have  $\delta^{34}\text{S}$  values between -12 and +3‰, with most values between -12 to -5‰ (Schmandt et al., in press). The abundant diagenetic pyrite at Kamoa has sulfur isotopic values ranging from -11 to +3‰ leading Schmandt et al. (in press) to conclude that the primary sulfur source for the copper deposit was diagenetic pyrite. As evidenced by the presence of iron formation at Fishtie and its absence at Kamoa, the two deposits, while both containing megascopically similar styles of sulfide-mineralized rock, have fundamental differences.

Given the apparent absence of anhydrite in the host rocks at Fishtie a possible source of reduced sulfur for the deposit was a reservoir of sour gas, similar to what has been envisioned for many of the sandstone-hosted deposits in the Zambian Copperbelt (Selley et al., 2005). Such a reservoir could account for the apparent low degree of sulfur isotopic fractionation as well as the observed muscovite mineralization that is at least in part probably temporally associated with sulfide mineralization. Alternatively, the heavy sulfur isotopic values of the Fishtie sulfides may indicate derivation of sulfur from Neoproterozoic seawater sulfate through thermochemical sulfate reduction with a relatively low degree of isotopic fractionation.

## CHAPTER 10

### CONCLUSIONS

The Fishtie copper deposit occurs at a higher stratigraphic level than most deposits in the Central African Copperbelt but is similarly located to the major Kamao and Lonshi deposits. All these deposits occur where the traditional host rocks for orebodies of the Roan Group were absent due to tectonically-related erosion or nondeposition. The Fishtie deposit was fundamentally controlled by normal faults. Three-dimensional modeling and isopach maps of the Grand Conglomérat unit indicate the thickest successions of diamictite occur adjacent to these faults indicating they had synsedimentary movement.

Fishtie contains the first Sturtian age iron formation described from the Central African Copperbelt. The iron formation occurs within the Grand Conglomérat unit and consists of bands of nearly monomineralic to intermixed magnetite, ankerite, apatite, and quartz. Iron formation thickens towards normal faults indicating they formed conduits for iron-rich hydrothermal solutions. The absence of iron formation clasts in the diamictite and presence of disseminated magnetite, ankerite, and apatite in adjacent diamictites suggests the iron formation formed by magnetite-ankerite-apatite precipitation within siltstones postdating deposition of the Grand Conglomérat unit. Like many other Neoproterozoic iron formations, that at Fishtie appears to have formed from hydrothermal fluids within a structurally enclosed sub-basin.

Later hydrothermal mineralization overprinted the iron formation and affected the entire preserved sequence of Katangan sedimentary rocks and locally basement rocks at Fishtie. Early potassium feldspar and biotite mineralization appears pervasive in both the Grand Conglomérat and Kakontwe Limestone units and is not clearly related to copper mineralization as has been suggested for the Zambian Copperbelt. Muscovite mineralization followed potassium feldspar

and biotite mineralization. Muscovite replaced earlier formed potassium feldspar and biotite and likely resulted in carbonate dissolution. This style of mineralization is similar to that observed in some deposits of the Zambian Copperbelt where it has been attributed to interaction of an oxidized ore fluid with trapped natural gas. The mineralogical and isotopic evidence from Fishtie is compatible with such a scenario. Chlorite mineralization, together with weak silicification, was that last major phase of mineralization at Fishtie and was temporally associated with extensive copper sulfide precipitation.

Copper sulfides at Kamoia display a relatively homogeneous distribution of relatively heavy sulfur isotopic values unlike many deposits in the Central African Copperbelt. These values could have resulted from sulfide derivation from either a sour gas reservoir or thermochemical reduction of Neoproterozoic seawater sulfate. In either case it is likely sulfide production involved a relatively low degree of isotopic fractionation.

The textures of alteration minerals and sulfides at Fishtie are strikingly similar to those at the recently discovered giant Kamoia deposit. However, the presence of iron formation and absence of abundant diagenetic pyrite at Fishtie, and the differing sulfur isotopic compositions of sulfides between the two deposits suggest there are fundamental differences in terms of a source of reduced sulfur. These differences may help to account for the difference of the sizes of the deposits. However, a more likely explanation for their different sizes is the differing locations of the deposits in relation to regional basinal architecture. Kamoia lies on the edge of the main Katangan basin in an area where basinally-derived hydrothermal fluids were focused into the Grand Conglomérat along a thinning wedge of underlying sandstones. Fishtie is located on the edge of a small sub-basin to the basin hosting the Zambian Copperbelt. It lacks a basal sequence of sandstones beneath the Grand Conglomérat that could have served as a regional aquifer for

basinally-derived hydrothermal fluids. Hydrothermal fluids at Fishtie were channeled upwards into the Grand Conglomérat unit along high angle normal faults.

## REFERENCES CITED

- Annels, A.E., 1989, Ore genesis in the Zambian Copperbelt, with particular reference to the northern sector of the Chambishi basin: Geological Association of Canada, Special Paper 36, p. 427–452.
- Armstrong, R.A., Master, S., and Robb, L.J., 2005, Geochronology of the Nchanga Granite, and constraints on the maximum age of the Katanga Supergroup, Zambian Copperbelt: *Journal of African Earth Science*, v.42, p. 41–60.
- Badenhorst, F.P., 1988, The lithostratigraphy of the Chuos mixtite in part of the southern central zone of the Damara Orogen, South West Africa: *Communications of the Geological Survey of Namibia*, v. 4, p. 103-110.
- Barron, J. W., 2003, The stratigraphy, metamorphism, and tectonic history of the Solwezi area, Northwest Province, Zambia: Integrating geological field observations and airborne geophysics in the interpretation of regional geology: Unpublished Ph.D. thesis, Golden, Colorado, Colorado School of Mines, 233 p.
- Batumike, M., Kampunzu, A., and Cailteux, J., 2006, Petrology and geochemistry of the Neoproterozoic Nguba and Kundelungu Groups, Katangan Supergroup, southeast Congo: Implications for provenance, paleoweathering and geotectonic setting: *Journal of African Earth Sciences*, v. 44, p. 97-115.
- Batumike, M. J., Cailteux, J. L. H., and Kampunzu, A.B., 2007, Lithostratigraphy, base metal deposits, and regional correlations of the Neoproterozoic Nguba and Kundelungu rock successions, central African Copperbelt: *Gondwana Research*, v. 11, p. 432-447.
- Beaudoin, G., Taylor, B., Rumble III, D., and Thiemens, M., 1994, Variations in the sulfur isotope composition of troilite from the Cañon Diablo iron meteorite: *Geochimica et Cosmochimica Acta*, v. 58, p. 4253-4255.
- Bekker, A., Slack, J.F., Planavsky, N., Krapez, B., Hofmann, A., Konhauser, K.O., and Rouxel, O.J., 2010, Iron Formation: The sedimentary product of a complex interplay among mantle, tectonic, oceanic, and biospheric processes: *Economic Geology*, v. 105, p. 467-508.
- Berger, M., Erickson, J., Fithian, M., Olson, C., Lagrava, P., Capistrant, P., Hitzman, M., Emsbo, P., Humphrey, J., and Broughton, D., 2013, An investigation into the Kipushi Zn-Cu-Pb-Ge deposit of the Central African Copperbelt: timing and source of fluids, sulfur, and metals: Program with abstracts, The Association of Mineral Exploration British Columbia, Mineral Exploration Roundup Conference, Vancouver, Canada.

- Binda, P.L., and van Eden, J.G., 1972, Sedimentological evidence on the origin of the Precambrian Great Conglomerat (Kundelungu Tillite), Zambia: *Palaeogeography, Palaeoclimatology, Palaeoecology*, v. 12, p. 151–168.
- Bodiselitsch, B., Koeberl, C., Master, S., and Reimold, W., 2005, Estimating duration and intensity of Neoproterozoic snowball Earth glaciations from Ir anomalies: *Science*, v. 308, p. 239–242.
- Bowring, S.A., Grotzinger, J.P., Condon, D.J., Ramezani, J., Newall, M.J., and Allen, P.A., 2007, Geochronologic constraints on the chronostratigraphic framework of the Neoproterozoic Huqf Supergroup, Sultanate of Oman: *American Journal of Science*, v. 307, p. 1097-1145.
- Brand, U. and Veizer, J., 1980, Chemical diagenesis of multicomponent carbonate system 1. Trace elements: *Journal of Sedimentary Petrology*, v. 50, 1219–1250.
- Bull, S., Selley, D., Broughton, D., Hitzman, M., Cailteux, J., Large, R., and McGoldrick, P., 2011, Sequence and carbon isotopic stratigraphy of the Neoproterozoic Roan Group strata of the Zambian copperbelt: *Precambrian Research*, v. 190, p. 70-89.
- Cahen, L., 1978, Les mixtites anté-cambriennes de l'est du Zaïre: mise au point interimaire. Musée Royale d'Afrique Centrale, Tervuren (Belgique), Département de Géologie et Minéralogie, Rapport Annuel, 1977, p. 33–64.
- Cailteux, J.L.H., Kampunzu, A.B., Lerouge, C., Kaputo, A.K., and Milesi, J.P., 2005a, Genesis of sediment-hosted stratiform copper-cobalt deposits, Central African Copperbelt: *Journal of African Earth Sciences*, v. 42, p. 134-158.
- Cailteux, J.L.H., Kampunzu, A.B., and Lerouge, C., 2007, Neoproterozoic Mwashya-Kansuki sedimentary rock succession in the central African Copperbelt, its Cu-Co mineralization and regional correlations: *Gondwana Research*, v. 11, p. 414-431.
- Canfield, D.E., 2004, The evolution of the Earth surface sulfur reservoir: *American Journal of Science*, v. 304, p. 839-861.
- Canfield, D.E., Poulton, S.W., Knoll, A.H., Narbonne, G.M., Ross, G., Goldberg, T., and Strauss, H., 2008, Ferruginous conditions dominated later Neoproterozoic deep-water chemistry: *Science*, v. 321, p. 949-952.
- Clifford, T.N., 2008, The geology of the Neoproterozoic Swakop-Otavi transition zone in the Outjo District, northern Damara Orogen, Namibia: *South African Journal of Geology*, v. 111, p. 117-140.
- Chumakov, N.M., 2007, Climates and climate zonality of the Vendian: geological evidence, in Vickers-Rich, P. and Komarower, P., (eds.), *The Rise and Fall of the Ediacaran Biotia*: Geological Society, London, Special Publications, v. 286, p. 15-26.

- Claypool, G., Hosler, W., Kaplan, I., Saki, H., and Zak, I., 1980, The age curves of sulfur and oxygen isotopes in marine sulfate and their mutual interpretation: *Chemical Geology*, v. 28, p. 199-260.
- Cornet, J., 1910, Gisements de minerais de fer du Congo, in *The Iron Ore Resources of the World: XI Int. Geol. Congr., Stockholm 1910*, vol. II. Generalstabens Litografiska Anstalt, Stockholm, p. 1037-1042.
- Corsetti, F.A. and Kaufman, A.J., 2003, Stratigraphic investigations of carbon isotope anomalies and Neoproterozoic ice ages in Death Valley, California: *Geological Society of America Bulletin*, v. 111, p. 916-932.
- Craig, H., 1957, Isotopic standards for carbon and oxygen and correction factors for mass-spectrometric analysis of carbon dioxide: *Geochemica et Cosmochemica Acta*, v. 12, p.133-149.
- Darnley, A.G., 1960, Petrology of some Rhodesian Copperbelt orebodies and associated rocks: *Institute of Mining and Metallurgy Transactions*, v. 69, p. 137–173.
- Dechow, E. and Jensen, M., 1965, Sulfur isotopes of some central African sulfide deposits: *Economic Geology*, v. 60, p. 894-941.
- de Magnée, I. and François, A., 1988, The origin of the Kipushi (Cu, Zn, Pb) deposit in direct relation with a Proterozoic salt diapir, Copperbelt of Central Africa, Shaba, Republic of Zaire, in Friedrich, G.H., et al. (eds.), *Base metal sulfide deposits*: Berlin, Springer-Verlag, p. 74–93.
- Derry, L.A., Kaufman, A.J., and Jacobsen, S.B., 1992, Sedimentary cycling and environmental change in the late Proterozoic, evidence from stable and radiogenic isotopes: *Geochimica et Cosochimica Acta*, v. 56, 1317–1329.
- De Waele, B., Kampunzu, A.B., Mapani, B.S.E., and Tembo, F., 2006, The Irumide Belt of Zambia: *Journal African Earth Science*, v. 46, p. 36-70.
- Dorr, J.V.N., II, 1945, Manganese and iron deposits of Morro do Urucum, Mato Grosso, Brazil: *U.S. Geological Survey Bulletin*, v. 946-A, p. 1-47.
- El Desouky, Muchez, P., and Cailteux, J., 2009, Two Cu-Co phases and contrasting fluid systems in the Katanga Copperbelt, Democratic Republic of Congo: *Ore Geology Reviews*, v. 36, p. 315-332.
- Friedman, I. and O'Neil, J., 1977, Compilation of stable isotope fractionation: Factors of geochemical interest, in *Data of Geochemistry 6th ed: Geology Survey Prof. Paper, Vol. KK* (ed. M. Fleischer), USGS.

- Gross, G.A., 1965, Iron-formation of the Snake River area, Yukon and Northwest Territories: Geological Survey of Canada, Paper 65-1, 143p.
- Haest, M., Muchez, P., Dewaele, S., Boyce, A., von Quadt, A., and Schneider, J., 2009, Petrographic, fluid inclusion and isotopic study of the Dikulushi Cu-Ag deposit, Katanga (D.R.C.): implications for exploration: *Mineralium Deposita*, v. 44, p. 505-522.
- Halverson, G.P., Hoffman, P.F., Schrag, D.P., Maloof, A.C., and Rice, A.H.N., 2005, Toward a Neoproterozoic composite carbon-isotope record: *Geological Society of America Bulletin*, v. 117, p. 1181-1207.
- Halverson, G.P., Wade, B.P., Hurtgen, M.T., and Barovich, K.M., 2010, Neoproterozoic chemostratigraphy: *Precambrian Research*, v. 182, p. 337-350.
- Hanson, R.E., Wardlaw, M.S., Wilson, T.J., and Mwale, G., 1993, U-Pb zircon ages from the Hook granite massif and Mwembeshi dislocation: Constraints on Pan-African deformation, plutonism, and transcurrent shearing in central Zambia: *Precambrian Research*, v. 63, p. 189-209.
- Hanssen, M.G., 2008, Kashime Copper Project, Mkushi: Copper Resource: Digital Mining Services, Harare, Zimbabwe.
- Hitzman, M.W., Broughton, D., Selley, D., Woodhead, J., Wood, D., and Bull, S., 2012, The Central African Copperbelt: diverse stratigraphic, structural, and temporal settings in the World's largest sedimentary copper district, *in* Hedenquist, J.W., Harris, M., and Camus, F., eds., *Geology and Genesis of Major Copper Deposits and Districts of the World: A Tribute to Richard H. Sillitoe*: SEG Special Publication 16, p. 487-514.
- Hitzman, M., Selley, D., and Bull, S., 2010, Formation of Sedimentary Rock-Hosted Stratiform Copper Deposits through Earth History: *Economic Geology*, v.105, p. 627-639.
- Hitzman, M., Kirkham, R., Broughton, D., Thorson, J., Selley, D., 2005, The sediment-hosted stratiform copper ore system, *in* Hedenquist, J. W., Thompson, J.F.H., Goldfarb, R. J., and Richards, J.P, eds.: *Economic Geology - 100th Anniversary Volume*, p. 609-642.
- Hoffman, P.F., Kaufman, A.J., Halverson, G.P., and Schrag, D.P., 1998b, A Neoproterozoic snowball Earth: *Science*, v. 281, p. 1342-1346.
- Hoy, L.D., and Ohmoto, H., 1989, Constraints for the genesis of redbed-associated stratiform Cu deposits from sulphur and carbon mass-balance relations: *Geological Association of Canada Special Paper* 36, p. 151-172.
- Ilyin, A.V., 2009, Neoproterozoic banded iron formations: *Lithology and Mineral Resources*, v. 44, p. 78-86.

- Jacobsen, S.B., Kaufman, A.J., The Sr, C, and O isotopic evolution of Neoproterozoic seawater: *Chemical Geology*, v. 161, p. 37-57.
- Jackson, M., Warin, O., Woad, G., and Hudec, M., 2003, Neoproterozoic allochthonous salt tectonics during the Lufilian orogeny in the Katangan Copperbelt, central Africa: *Geological Society of America Bulletin*, v. 115, p. 314-330.
- Jamotte, A., 1950, L'importance des gisements de fer du Haut Lualaba et leur signification métallogénique: C.R. Congrès Scient., Élisabethville 1950, Comité Special du Katanga, Bruxelles, vol. III, p. 119-128.
- Jiafu, T., Fu, H., and Yu, Z., 1987, Stratigraphy, type and formation conditions of Late Precambrian banded iron ores in South China: *Chinese Journal of Geochemistry*, v. 6, p. 332-351.
- Jiang, G., Kennedy, M.J., Christie-Blick, N., 2003, Stable isotopic evidence for methane seeps in Neoproterozoic postglacial cap carbonates: *Nature*, v. 426, p. 822–826.
- John, T., Schenk, V., Mezger, K., and Tembo, F., 2004, Timing and PT evolution of whiteschist metamorphism in the Lufilian arc-Zambezi belt orogeny (Zambia): Implications for the assembly of Gondwana: *Journal of Geology*, v. 122, p. 71–90.
- Kampunzu, A.B., and Cailteux, J., 1999, Tectonic evolution of the Lufilian arc (Central Africa Copper Belt) during Neoproterozoic Pan African orogenesis: *Gondwana Research*, v. 2, p. 401–421.
- Klein, C. and Ladeira, E.A., 2004, Geochemistry and mineralogy of Neoproterozoic banded iron-formations and selected siliceous manganese formations from the Urucum District, Mato Grosso Do Sul, Brazil: *Economic Geology*, v. 99, p. 1233-1244.
- Key, R.M., Liyungu, A.K., Njamu, F.M., Somwe, V., Banda, J., Mosley, P.N., and Armstrong, R.A., 2001, The western arm of the Lufilian arc in NW Zambia and its potential for copper mineralization: *Journal of African Earth Sciences*, v. 33, p. 503–528.
- Kirschvink, J.L., 1992, Late Proterozoic low-latitude global glaciation: the snowball Earth, *in* Schopf, J.W., and Klein, C., eds., *The Proterozoic Biosphere: A Multidisciplinary Study*: Cambridge University Press, Cambridge, p. 51-52.
- Klein, C. and Beukes, N.J., 1993, Sedimentology and geochemistry of the glaciogenic Late Proterozoic Rapitan iron-formation in Canada: *Economic Geology*, v. 88, p. 542- 565.
- Lerouge, C., Cailteux, J., Kampunzu, A., Milesi, J., and Flehoc, C., 2005, Sulfur isotope constraints on formation conditions of the Luiswishi ore deposit, Democratic Republic of Congo (DRC): *Journal of African Earth Sciences*, v. 42, p. 173-182.

- Lottermoser, B.G. and Ashley, P.M., 2000, Geochemistry, petrology and origin of Neoproterozoic ironstones in the eastern part of the Adelaide Geosyncline, South Australia: *Precambrian Research*, v. 101, p. 49-67.
- Macdonald, F.A., Jones, D.S., and Schrag, D.P., 2009, Stratigraphic and tectonic implications of a newly discovered glacial diamictite-cap carbonate couplet in southwestern Mongolia: *Geology*, v. 37, p. 123-126.
- Macdonald, F.A., Schmitz, M.D., Crowley, J.L., Roots, C.F., Jones, D.S., Maloof, A.C., Strauss, J.V., Cohen, P.A., Johnston, D.T., and Schrag, D.P., 2010a, Calibrating the Cryogenian: *Science*, v. 327, p. 1241-1243.
- Macdonald, F.A., Strauss, J.V., Rose, C.V., Dubás, F. Ñ., and Schrag, D.P., 2010b, Stratigraphy of the Port Nolloth Group of Namibia and South Africa and implications for the age of Neoproterozoic iron formations: *American Journal of Science*, v. 310, p. 862-888.
- Machel, H.G., 1989, Relationships between sulphate reduction and oxidation of organic compounds to carbonate diagenesis, hydrocarbon accumulations, salt domes, and metal sulphide deposits: *Carbonates and Evaporites*, v. 4, p. 137-151.
- Machel, H., Krouse, H., and Sassen, R., 1995, Products and distinguishing criteria of bacterial and thermochemical sulfate reduction: *Applied Geochemistry*, v. 10, p.373-389.
- Master, S. and Wendorff, M., 2011, Neoproterozoic glaciogenic diamictites of the Katanga Supergroup, Central Africa, in Arnaud, E., Halverson, G. P. and Shields-Zhou, G. (eds): *The Geological Record of Neoproterozoic Glaciations*. Geological Society, London, *Memoirs*, no. 36, p. 173-184.
- McGowan, R.R., 2003, The origin of the Nchanga copper-cobalt deposits of the Zambian Copperbelt: Unpublished Ph.D. thesis, Southampton, UK, University of Southampton, 204 p.
- McGowan, R., Roberts, R., and Boyce, A., 2006, Origin of the Nchanga copper-cobalt deposits of the Zambian Copperbelt: *Mineralium Deposita*, v. 40, p. 617-638.
- Morad, S., Ketzer, J., and De Ros, L., 2000, Spatial and temporal distribution of diagenetic alterations in siliciclastic rocks: implications for mass transfer in sedimentary basins: *Sedimentology*, v. 47, p.95-120.
- Muchez, P., Brems, D., Clara, E., De Cleyn, A., Lammens, L., Boyce, A., De Muynck, D., Mukumba, W., and Sikazwe, O., 2010, Evolution of Cu-Co mineralizing fluids at Nkana Mine, Central African Copperbelt, Zambia: *Journal of African Earth Sciences*, v. 58, p. 457-474.
- Muchez, P., Vanderhaeghen, P., El Desouky, H., Schneider, J., Boyce, A., Dewaele, S., and Cailteux, J., 2008, Anhydrite pseudomorphs and the origin of stratiform Cu-Co ores in

- the Katangan Copperbelt (Democratic Republic of Congo): *Mineral Deposita*, v. 43, p. 575-589.
- Ohmoto, H., and Goldhaber, M.B., 1997, Sulfur and carbon isotopes, *in* Barnes, H.L., ed., *Geochemistry of hydrothermal ore deposits*, 3rd edition: New York, Wiley, p. 517–612.
- Porada, H. and Berhorst, V., 2000, Towards a new understanding of the Neoproterozoic-Early Paleozoic Lufilian and northern Zambezi belts in Zambia and the Democratic Republic of Congo: *Journal of African Earth Sciences*, v. 30, p. 727-771.
- Prave, A.R., 1999, Two diamictites, two cap carbonates, two  $\delta^{13}\text{C}$  excursions, two rifts: The Neoproterozoic Kingston Peak Formation, Death Valley, California: *Geology*, v. 27, p. 339-342.
- Preiss, W.V., 1987, The Adelaide Geosyncline: Late Proterozoic stratigraphy, sedimentation, paleontology and tectonics: *Geological Survey of South Australia Bulletin*, v. 53, 438 p.
- Rainaud, C., Master, S., Armstrong, R.A., Phillips, D., and Robb, L.J., 2002, Contributions to the geology and mineralisation of the Central African Copperbelt: II. Monazite U-Pb dating and  $^{40}\text{Ar}$ - $^{39}\text{Ar}$  thermochronology of metamorphic events during the Lufilian orogeny [abs.]: 11th IAGOD Quadrennial Symposium and Geocongress, Windhoek, Namibia, Geological Survey Namibia. (CD-ROM)
- Schmandt, D., Broughton, D., Hitzman, M.W., Plink-Bjorklund, P., Edwards, and D., Humphrey, J., *in press*, The Kamao Copper Deposit, Democratic Republic of Congo: Stratigraphy, Diagenetic and Hydrothermal Alteration, and Mineralization: *Economic Geology*.
- Schmandt, D., 2012, Stratigraphy and mineralization of the Kamao Cu deposit, Katanga, Democratic Republic of Congo: Unpub. M.S. thesis, Colorado School of Mines, Golden, CO., 89 p.
- Scotese, C. R., 2009, Late Proterozoic plate tectonics and palaeogeography: a tale of two supercontinents, Rodinia and Pannotia, *in* Craig, J. Thurow, J., Thusu, B., Whitham, A., and Abutarruma, Y. (eds.), *Global Neoproterozoic Petroleum Systems: The Emerging Potential in North Africa*, Geological Society, London, Special Publications, no. 326, p. 67-83.
- Selley, D., Broughton, D., Scott, R., Hitzman, M., Bull, S., Large, R., McGoldrick, P., Croaker, M., Pollington, N., Barra, F., 2005, A new look at the geology of the Zambian Copperbelt: *Economic Geology 100th Anniversary Volume*, p. 965–1000.
- Sengor, A.M.C., Burke, K, and Dewey, J.F., 1978, Rifts at right angles to orogenic belts: tests for their origin and the Upper Rhine graben as an example: *American Journal of Science*, v. 278, p. 24-40.

- Sverjensky, D.A., 1981, Isotopic alteration of carbonate host rocks as a function of water to rock ratios – an example from the Upper Mississippi Valley zinc–lead district: *Economic Geology*, v. 76, 154–172.
- Smith, A.G., 2009, Neoproterozoic timescales and stratigraphy, *in* Craig, J. Thurow, J., Thusu, B., Whitham, A., and Abutarruma, Y. (eds.), *Global Neoproterozoic Petroleum Systems: The Emerging Potential in North Africa*, Geological Society, London, Special Publications, no. 326, p. 27-54.
- Stillman, C.J., 1965, The Geology of the Musofu River and Mkushi Areas, Explanation of Degree Sheet 1329, Part of NW. Quarter, and SW. Quarter: *Zambian Geologic Survey Report no. 12*, p.1-51, 2 plates.
- Strauss, H., 1997, The isotopic composition of sedimentary pyrite through time: *Palaeogeography, Palaeoclimatology, Palaeoecology*, v. 132, p. 97-118.
- Strauss, H., Banerjee, D., and Kumar, V., 2001, The sulfur isotopic composition of Neoproterozoic to early Cambrian seawater - evidence from cyclic Hanseran evaporites, NW India: *Chemical Geology*, v. 175, p. 17-28.
- Sun, S. and McDonough, W., F., 1989, Chemical and isotopic systematics of oceanic basalts: implications for mantle composition and processes: *Geological Society, London, Special Publications*, v. 42, p.313-345.
- Sweeney, M. and Binda, P., 1989, The role of diagenesis in the formation of the Konkola Cu-Co ore-body of the Zambian Copperbelt, *in* Boyle, R. et al., eds., *Sediment hosted stratiform copper deposits: Geological Association of Canada Special Paper 36*, p. 427-452.
- Trompette, R., de Alvarenga, C.J.S., and Walde, D., 1998, Geological evolution of the Neoproterozoic Corumba graben system (Brazil). Depositional context of the stratified Fe and Mn ores of the Jacadigo Group: *Journal of South American Earth Sciences*, v. 11, p. 587-597.
- Tucker, M., 2001, *Sedimentary Petrology: An Introduction to the Origin of Sedimentary Rocks*, third edition: Blackwell publishing, p. 100-109.
- Urban, H., Stribny, B., and Lippoly, H.J., 1992, Iron and manganese deposits of the Urucum District, Matto Grosso do Sul, Brazil: *Economic Geology*, v. 87, p. 1375-1892.
- Walsh, J.J., and Watterson, J., 1989, Displacement gradients on fault surfaces: *Journal of Structural Geology*, v. 11, p. 307–316.
- Wang, J. and Li, Z.-X., 2003, History of Neoproterozoic rift basins in South China: implications for Rodinia break-up: *Precambrian Research*, v. 122, p. 141-158.

- Wendorff, M. and Key, R.M., 2009, The relevance of the sedimentary history of the Grand Conglomérat Formation (Central Africa) to the interpretation of the climate during a major Cryogenian glacial event: *Precambrian Research*, v. 172, p. 127-142.
- Woodhead, J., 2013, The Neoproterozoic Roan Group in the Zambian Copperbelt: sequence stratigraphy, alteration, and mineralization: Unpub. Ph.D. dissertation, Colorado School of Mines, Golden, CO., 281p.
- Xu, B., Xiao, S., Zou, H.-B., Chen, Y., Li, Z.-X., Song, B., Liu, D.-Y., Zhou, C.-M., and Yuan, X.-L., 2009, SHRIMP zircon U-Pb age constraints on Neoproterozoic Quruqtah diamictites in NW China: *Precambrian Research*, v. 168, p. 247-258.
- Yeo, G.M., 1981, The Late Proterozoic Rapitan glaciation in the northern Cordillera, *in* Campbell, F.H.A., ed., *Proterozoic Basins of Canada: Geological Survey of Canada Paper 81-10*, p. 25-46.
- Yeo, G.M., 1986, Iron-formation in the Late Proterozoic Rapitan Group, Yukon and Northwest Territories: *Canadian Inst. Mining Metallurgy Spec. Vol. 37*, p. 142-153.
- Young, G. M., 1976, Iron-formations and glaciogenic rocks of the Rapitan Group, Northwest Territories, Canada: *Precambrian Research*, v .3, p. 137-178.
- Young, G.M., 2002, Stratigraphic and tectonic settings of Proterozoic glaciogenic rocks and banded iron-formations: relevance to the snowball Earth debate: *Journal of African Earth Sciences*, v. 35, p. 451-466.
- Yoshioka, H., Asahara, Y., Tojo, B., and Kawakami, S., 2003, Systematic variations in C, O, and Sr isotopes and elemental concentrations in Neoproterozoic carbonates in Namibia: implications for a glacial to interglacial transition: *Precambrian Research*, v. 124, p. 69-85.
- Zheng, Y.F., Hoefs, J., 1993. Carbon and oxygen isotope covariations in hydrothermal calcites: *Mineralium Deposita* 28, 79–89.

## APPENDIX A

### AEROMAGNETIC, RADIOMETRIC, INDUCED POLARIZATION AND LANDSAT DATA

#### A.1 Methods

An aeromagnetic survey was flown over the Fishtie area in 2006 at an average elevation of 90 meters above terrain. The survey utilized 80 meter line spacing with 200 meter tie line spacing. The raw data was reduced to pole and filtered using standard horizontal gradient, analytic signal and terracing techniques by Misac Nabighan at the Colorado School of Mines Center for Gravity, Electrical and Magnetic research (CGEM) and exported as text files. 506,217 discrete data points were generated for each filter method and geocoded with easting and northing values using a UTMWGS84 Zone35S projection. Nano-tesla or gradient data (Z-value) at each geocoded point was gridded using the average of coincident points in a minimum curvature method to generate continuously variable surfaces that are clipped using a buffer technique. The minimum curvature method utilized an interior tension of 25 and an exterior tension of 0, a maximum of 50 iterations between points, and a cell size of 25.

Radiometric data was collected under the same flight specifications as the aeromagnetic survey. Counts for potassium, uranium, and thorium were collected every 0.1 seconds for 512 in<sup>3</sup> volume generation. These data were plotted with the same surface generation techniques used for magnetic data.

Induced polarization data was collected using a time domain technique and dipole-dipole array. Electrodes were spaced 50m and profiled along a grid extending beyond the eastern margin of the drill grid. Measurements were collected starting at 54.8 seconds, and every 148.7 seconds after for a total of 14 resistivity values generated on each line on average. Data was reduced to provide apparent resistivity, chargeability, and metal factor by external consulting

geophysicists. These reduced data were used to create false color surfaces using the same techniques used for magnetic and radiometric data.

## **A.2 Results**

Aeromagnetic data suggests Fishtie is located near the northeast margin of the Lusale basin. Directly north of the deposit area Katangan sediments form a possible connection to the Katangan basin east of the Zambian Copperbelt. Magnetic data indicates the presence of intrusive bodies northwest of the deposit area and in the center of the Lusale basin. The basement rocks that form the western margin of the Lusale basin are complexly deformed. A small sub-basin ~10 km northeast of Fishtie hosts anomalous Cu values in soil samples (Figures A-1 through A-4).

Radiometric data effectively outlines the Katangan sediments of the Lusale basin, but do not provide vectors to alteration zones in the deposit area (Figures A-5 through A-7).

Chargeability from induced polarization surveys broadly correlates to projected-to-surface copper grade, but resistivity and metal factor do not appear to correlate with known mineralized zones (Figure A-8a, b, c).

Landsat imagery effectively shows the large quartzite ridge northwest of the deposit area and also shows the complexly deformed basement rocks near the southwest basin margin (Figure A-9).

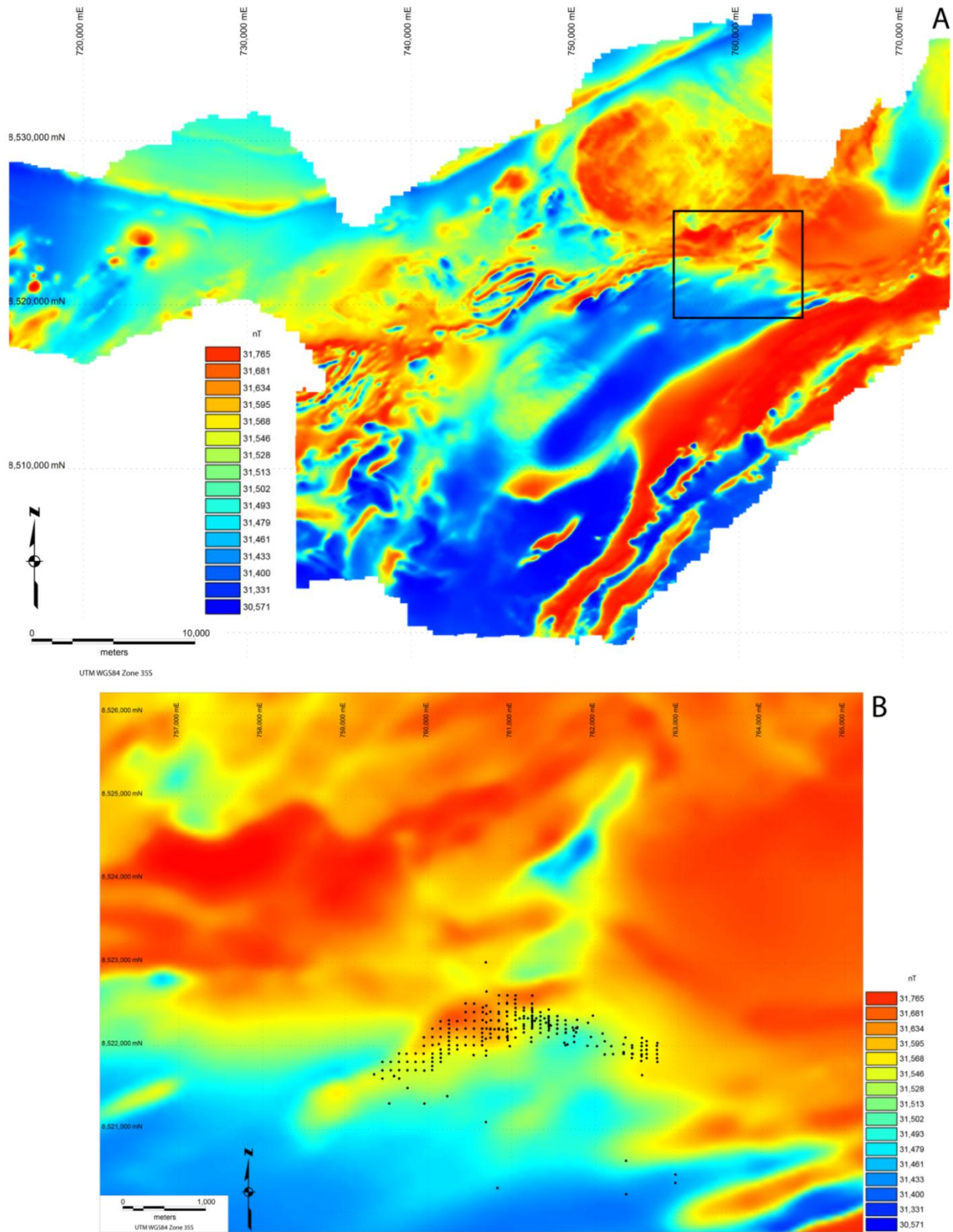


Figure A-1: Reduced to pole (RTP) aeromagnetic maps: (A) Lusale Basin and surrounding area with Figure B outlined in black. (B) The Fishtie copper deposit area. Drill holes are denoted by black circles.

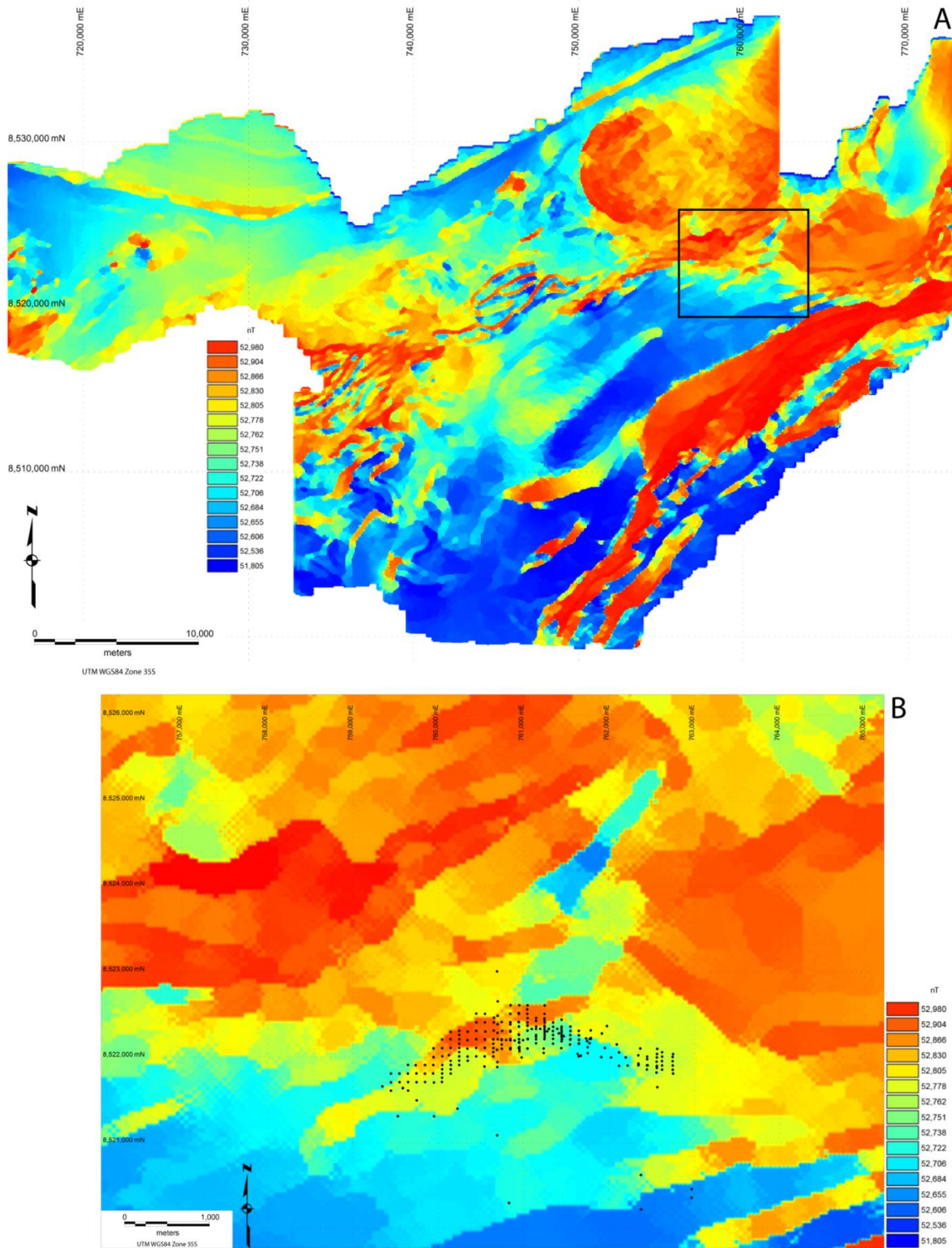


Figure A-2: Terraced aeromagnetic maps: (A) Lusale Basin and surrounding area with Figure B outlined in black. (B) The Fishtie copper deposit area. Drill holes are denoted by black circles.

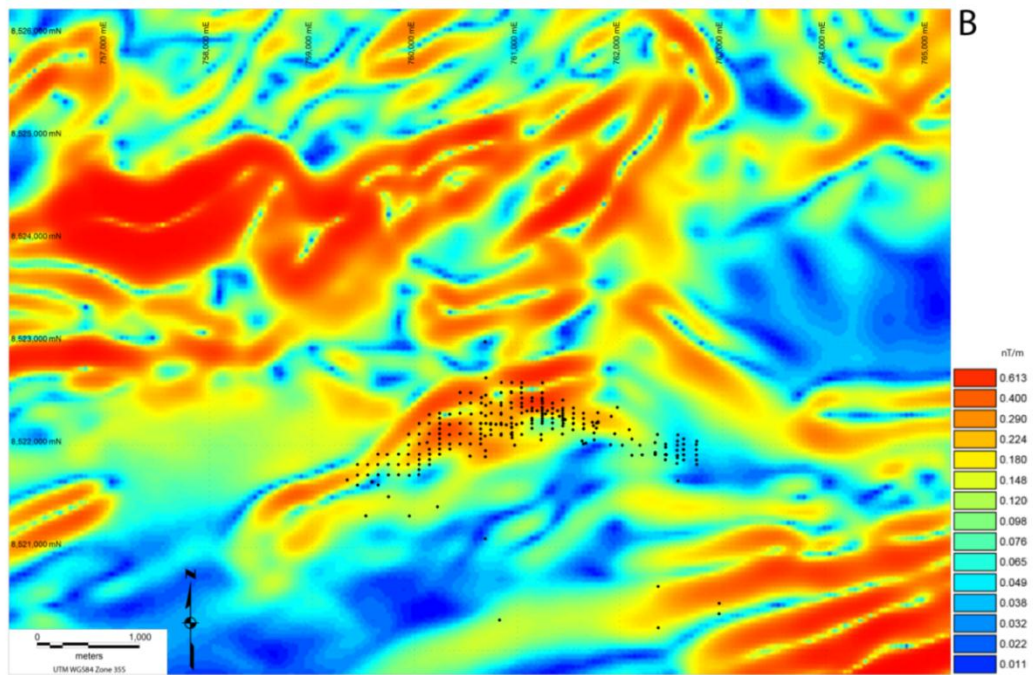
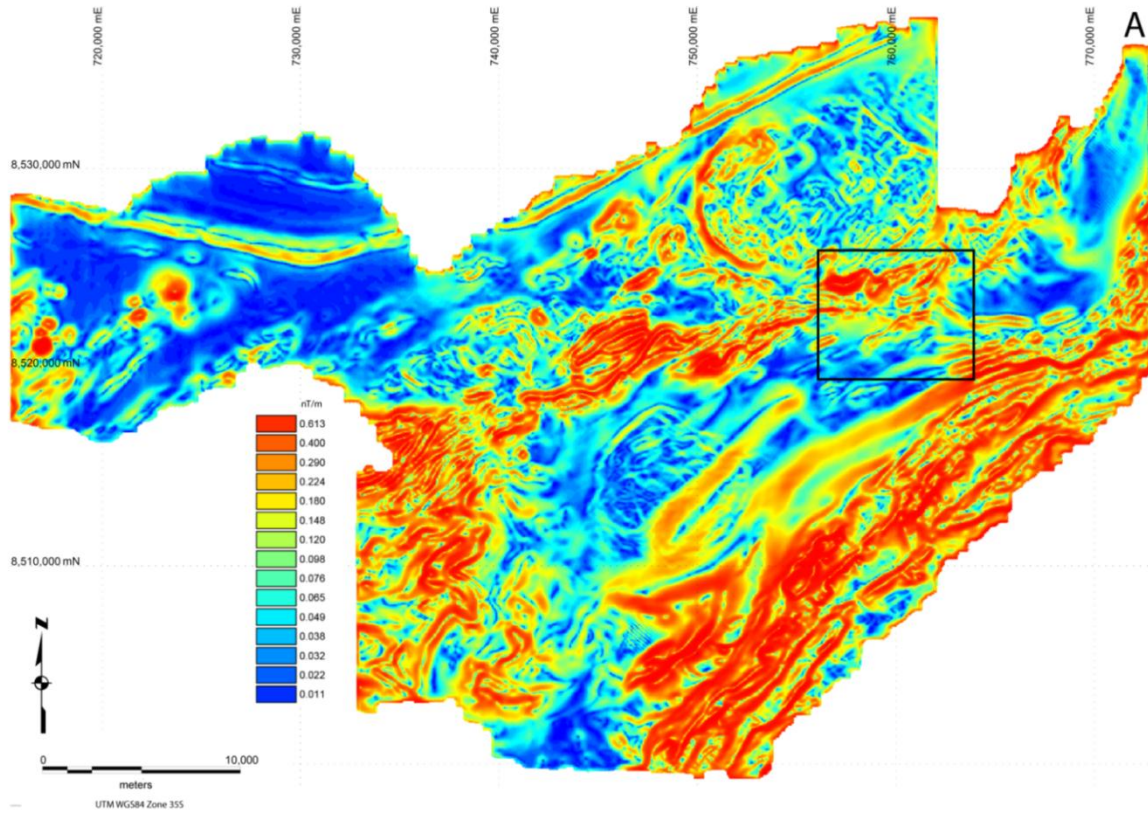


Figure A-3: Horizontal Gradient filtered aeromagnetic maps: (A) Lusale Basin and surrounding area with Figure B outlined in black. (B) The Fishtie copper deposit area. Drill holes are denoted by black circles.

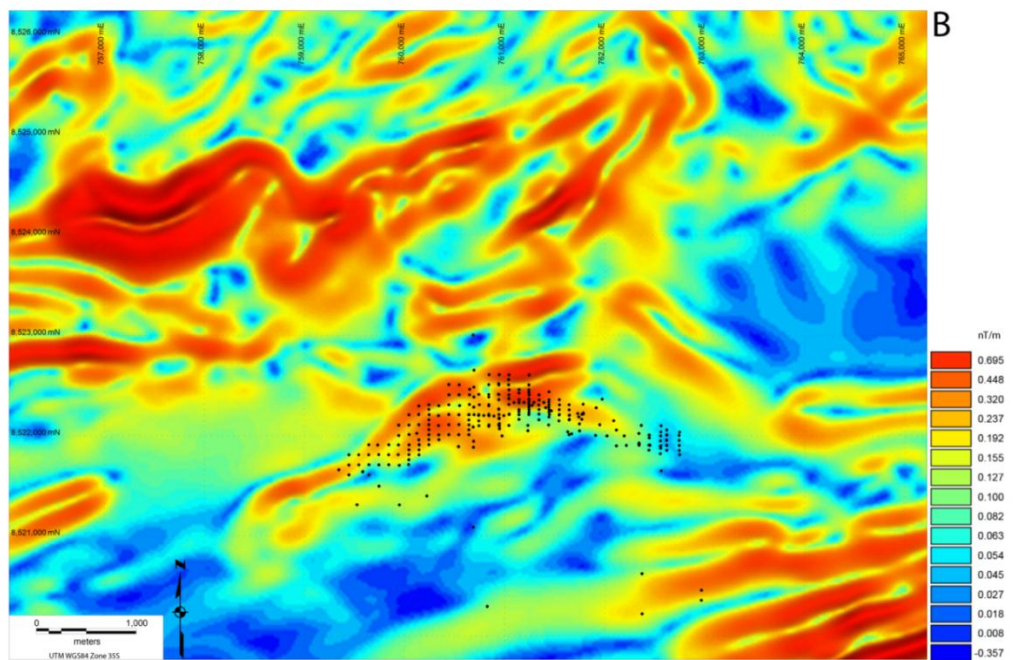
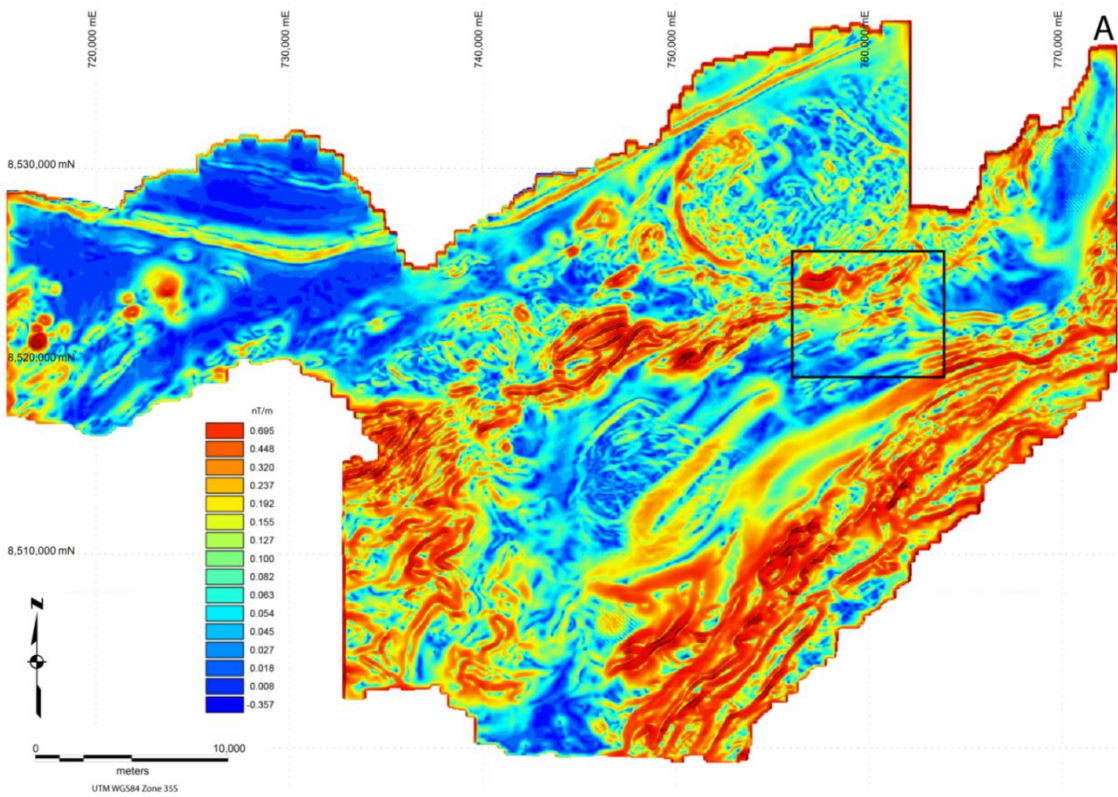


Figure A-4: Analytic Signal filtered aeromagnetic maps: (A) Lusale Basin and surrounding area with Figure B outlined in black. (B) The Fishtie copper deposit area. Drill holes are denoted by black circles.

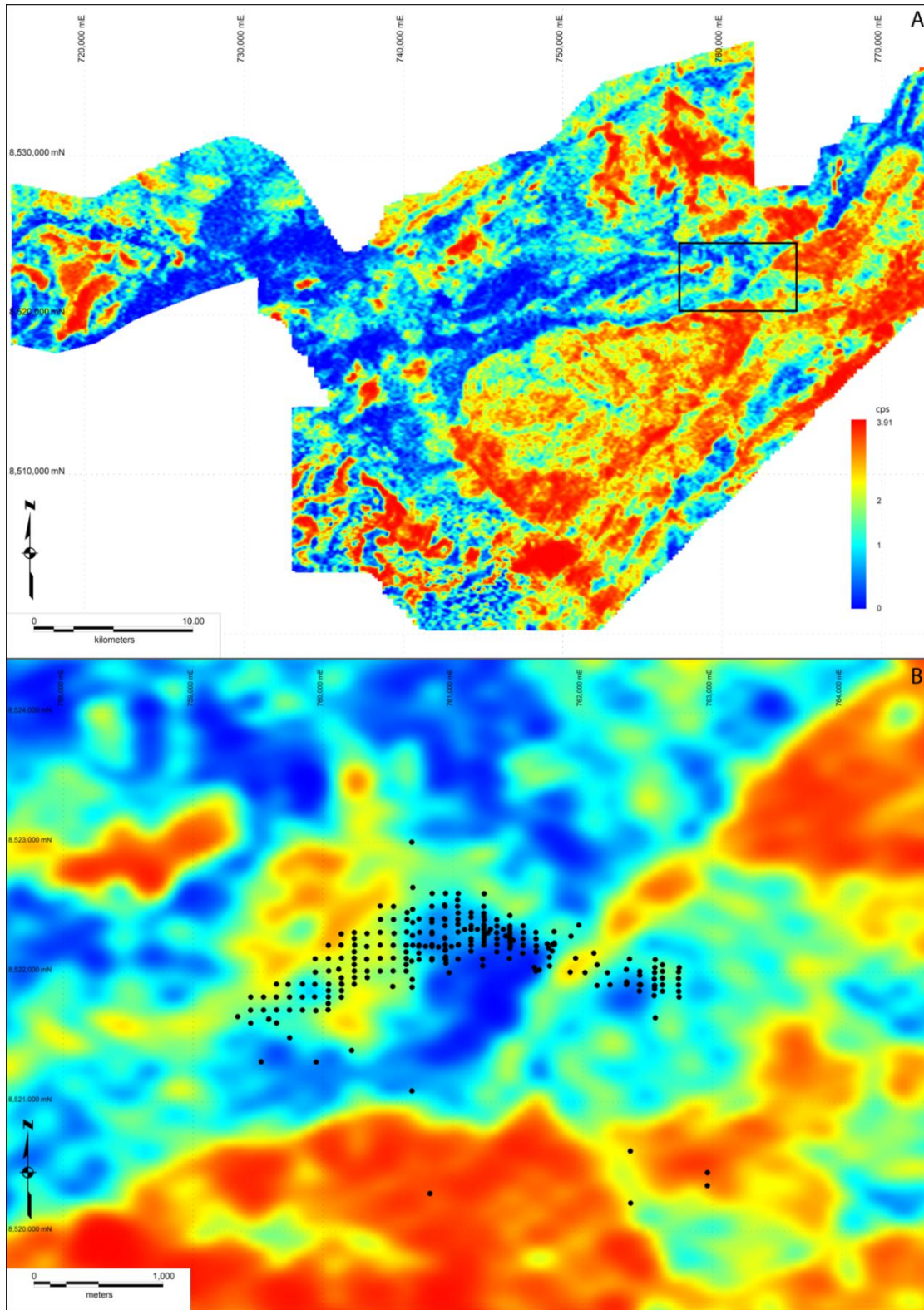


Figure A-5: Potassium radiometric anomaly maps: (A) Lusale Basin and surrounding area with Figure B outlined in black. (B) The Fishtie copper deposit area. Drill holes denoted by black circles.

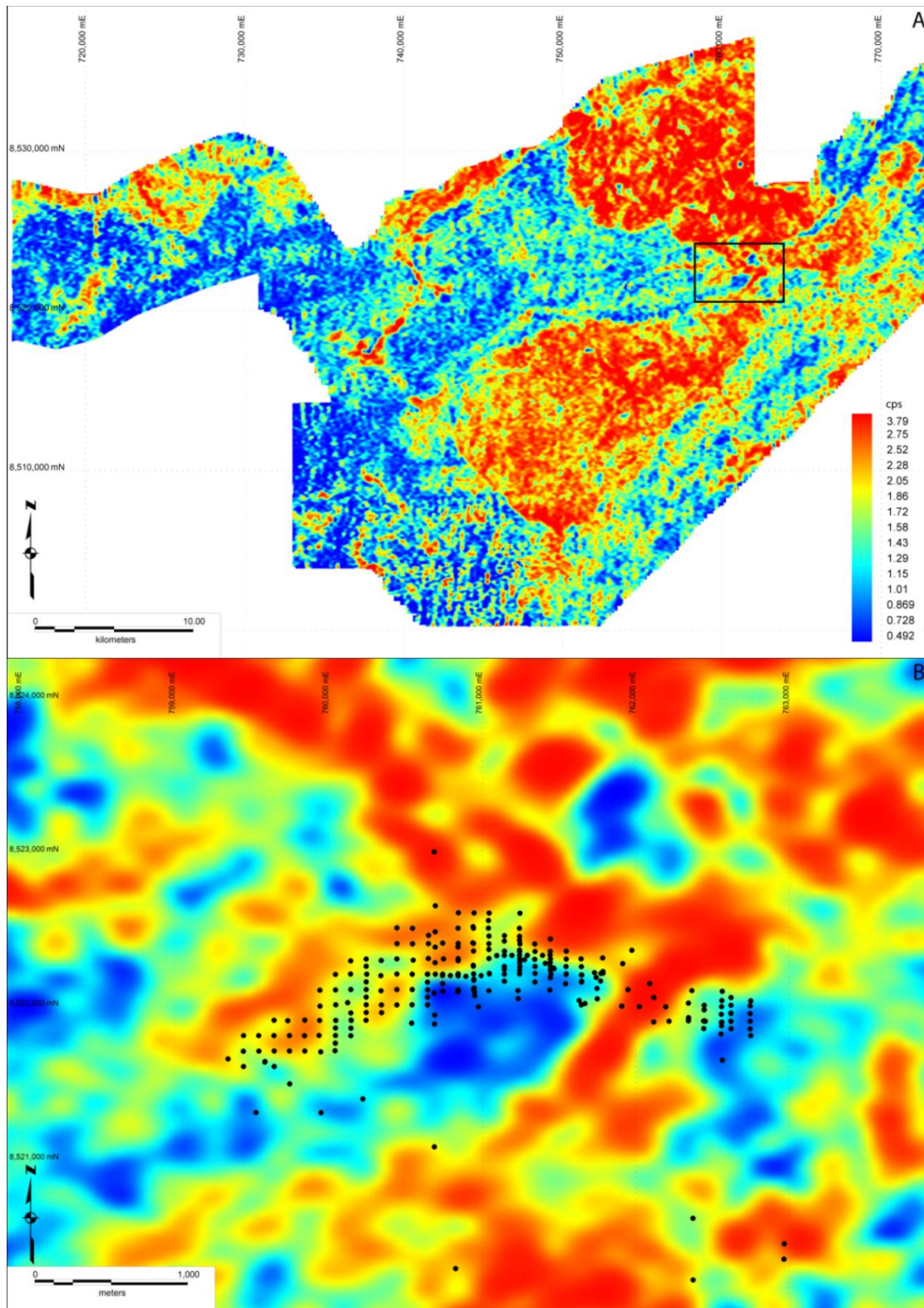


Figure A-6: Uranium radiometric anomaly maps: (A) Lusale Basin and surrounding area with Figure B outlined in black. (B) The Fishtie copper deposit area. Drill holes denoted by black circles.

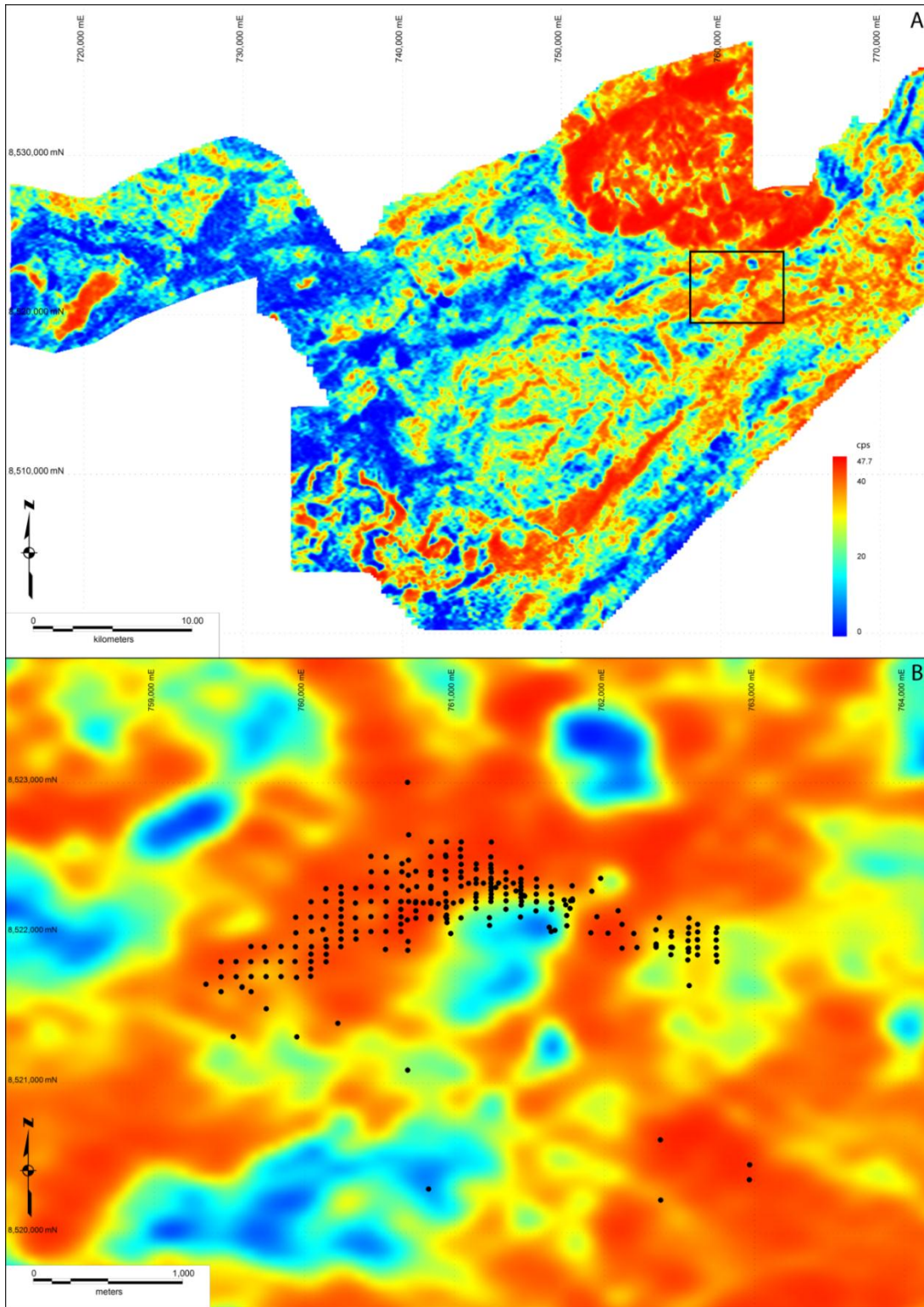


Figure A-7: Thorium radiometric anomaly maps: (A) Lusale Basin and surrounding area with Figure B outlined in black. (B) The Fishtie copper deposit area. Drill holes denoted by black circles.

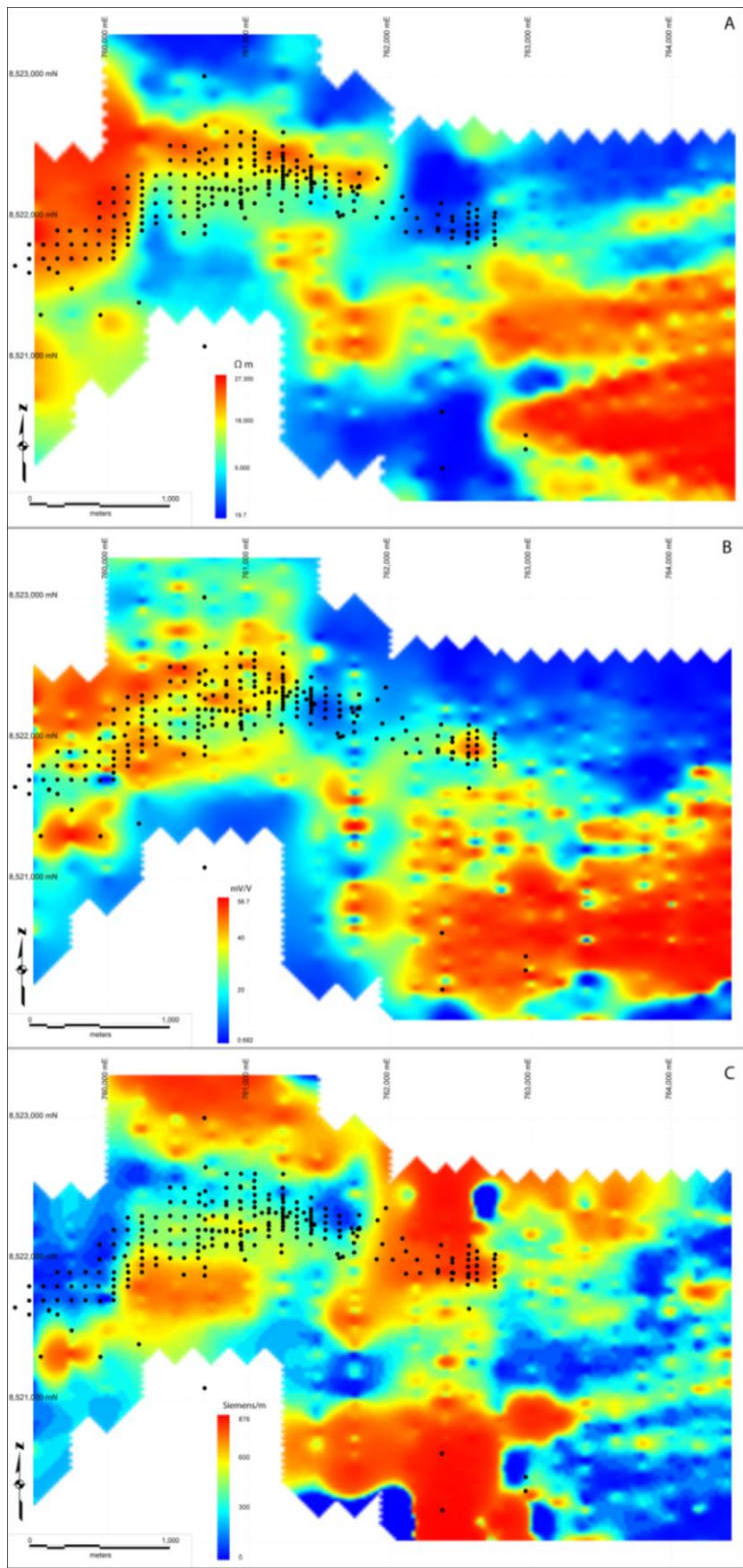


Figure A-8: Induced polarization anomaly maps of the Fishtie area: (A) Resistivity. (B) Chargeability. (C) Metal Factor.

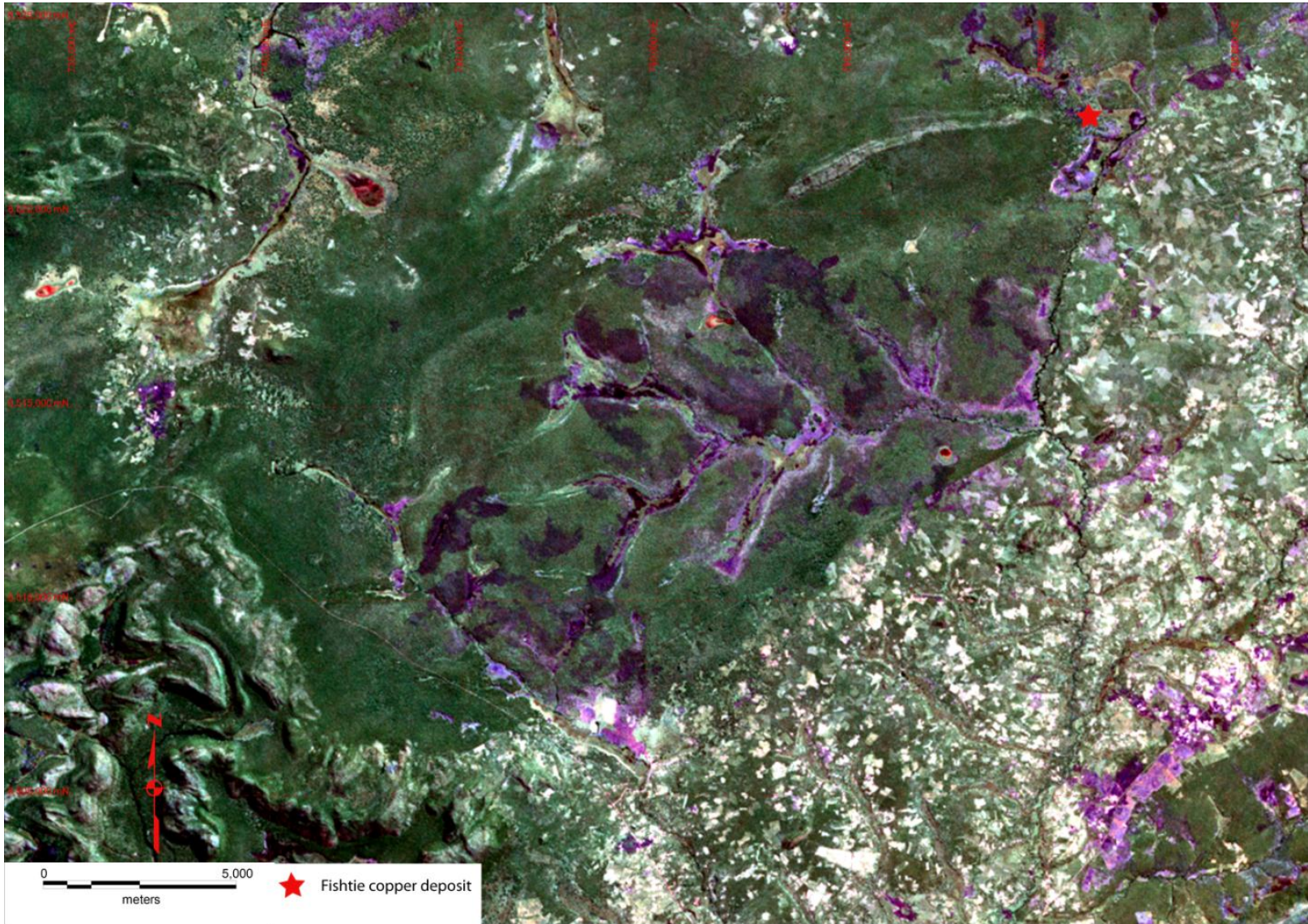


Figure A-9: Landsat image of the Lusale basin and surrounding area. The Fishtie copper deposit is denoted by the red star.

APPENDIX B  
MAJOR ELEMENT AND TRACE ELEMENT GEOCHEMISTRY

**B.1 Methods**

Twenty-eight samples were collected for whole rock and trace element geochemistry analysis that was conducted at ALS Chemex in Elko, Nevada. Both unaltered and altered and mineralized samples of all the lithological units, including the iron formation, at Fishtie were analyzed. Samples from a weakly altered hole (KEDD0076) outside the mineralized zone were utilized to provide comparative baseline values. Sampling focused on siltstone units within the Grand Conglomérat rather than diamictite units as the abundant lithic clasts in the diamictites complicates whole rock composition.

Samples for whole rock geochemical analyses were crushed and then decomposed using Lithium Metaborate/ Lithium Tetraborate. Samples for trace element analysis were crushed and then decomposed using Lithium Metaborate Fusion. Whole rock and trace element analysis was accomplished through Inductively Coupled Plasma-Atomic Emission Spectrometry (ICP-AES).

All rare earth element abundances were normalized to chondritic values using data from Sun and McDonough (1989).

**B.2 Results**

Iron formation has elevated phosphate and total carbon values. The quartz-carbonate vein has elevated calcium, magnesium, carbon, sulfur, and cobalt values. The basement rock from DDH KEDD0012 is enriched in calcium and magnesium (Table B-1, Figure B-1).

Trace element contents of all rock units are relatively consistent, with general enrichment in barium, chromium, rubidium, strontium, zirconium, vanadium, arsenic, and bismuth (Table B-2, Figure B-2).

Metal content is variable across rock units. Most samples contain anomalous copper and cobalt. Silver is conspicuously absent and molybdenum occurs at low values. Nickel, lead, and zinc are variably anomalous in some carbonate units, siltstones, the carbonate vein, and basement rock in DDH KEDD0012 (Table B-3, Figure B-3).

Rare earth element geochemistry is relatively consistent in all rock units, with light rare earth elements occurring in higher concentration than heavy rare earth elements. Enrichment in lanthanum, cerium and neodymium, and depletion in praseodymium is most common (Tables B-4 through B-6, Figures B-4 through B-6).

Table B-1: Major element values (in weight %) of the basement, altered basement, Grand Conglomérat diamictite and siltstone, iron formation, Kakontwe Limestone unit, and quartz-carbonate veins from DDH KEDD0012.

Sample Number	Lithology	SiO2	Al2O3	Fe2O3	CaO	MgO	Na2O	K2O	Cr2O3	TiO2	MnO	P2O5	SrO	BaO	C	S	Co	Cu	LOI	Total
GX-08-133	Basement schist	62.6	17.8	6.23	0.44	1.86	0.24	4.74	0.01	0.89	0.04	0.09	0.01	0.1	0.11	0.05			3.66	98.71
GX-33-74.5	Basement schist	72.3	14.75	3.74	0.32	1.14	0.59	3.44	0.01	0.78	0.03	0.02		0.06	0.61	0.04			3.31	100.49
GX-34-155	Basement schist	72	14.25	3.77	0.28	1.13	0.81	3.46	0.01	0.61	0.03	0.03	0.01	0.06	0.34	0.03			2.76	99.21
GX-76-177.2	Basement Quartzite	93.4	2.16	1.47	1.18	0.65	0.02	0.47		0.08	0.01	0.01		0.01	0.31	0.01			1.17	100.63
GX-135-89	Kakontwe Limestone Unit	23.2	4.66	2.14	19.3	16.75	0.02	1.73		0.29	0.21	0.13	0.02	0.01	8.35	0.51			30.2	98.66
GX-142-88.5	Kakontwe Limestone Unit	36.4	7.35	2.51	13.15	11.75	0.04	2.74	0.01	0.54	0.15	0.17	0.02	0.03	5.69	1.04		2.85	19.75	94.61
GX-142-150	Kakontwe Limestone Unit	4.55	0.76	0.74	29.4	20.9	0.01	0.36		0.05	0.21	0.04	0.02		12.15	0.02			44.8	101.84
GX-135-153	Kakontwe Limestone Unit	6.13	1.58	0.78	27.9	20	0.01	0.84		0.1	0.21	0.06	0.01	0.01	11.65	0.01			43.4	101.03
GX-34-85	Kakontwe Limestone Unit	2.09	0.29	0.64	30.3	21.5	0.03	0.13		0.01	0.27	0.04	0.02		12.4				46.2	101.52
GX-76-38	Kakontwe Limestone Unit	67.2	6.08	1.21	9.28	9.63	3.42	0.13		0.05	0.06	0.04			0.93	0.01			4.52	101.62
GX-76-99.5	Kakontwe Limestone Unit	2.26	0.29	0.68	30.8	21.3	0.01	0.14		0.02	0.37	0.03	0.02		12.35				45.9	101.82
GX-76-114.9	Kakontwe Limestone Unit	4.44	0.93	0.71	51.5	1.14	0.01	0.32		0.06	0.22	0.03	0.15		10.85	0.23			41	100.51
GX-06-62	Grand Conglomérat diamictite	38.5	6.33	28.8	10.4	2.54	0.09	2.07	0.01	0.43	0.34	3.89	0.02	0.02	1.85	0.17			6.91	100.35
GX-135-223	Grand Conglomérat diamictite	69.6	11.15	4.32	1.74	3.35	1	2.62	0.01	0.71	0.13	0.13	0.01	0.05	0.74	0.29			4.18	99
GX-76-160.3	Grand Conglomérat diamictite	94	0.73	1.39	2.04	0.28	0.03	0.22	0.01	0.05	0.01				0.57	0.01			0.76	99.52
GX-06-61	Iron Formation	58.5	13.75	16.25	1	3.58	1.23	1.9	0.01	0.88	0.1	0.4		0.03	0.14	0.09			3.67	101.3
GX-33-44	Iron Formation	36	3.47	42.9	3.66	3.18	0.03	0.84		0.32	0.68	0.89	0.01	0.01	2.72	0.1			8.85	100.84
GX-34-112.5	Iron Formation	31.9	4.97	45.6	6.93	2.24	0.09	0.85		0.39	0.25	3.95	0.02	0.01	0.94	0.23			3.26	100.46
GX-76-126.3	Grand Conglomérat siltstone	57.7	14.95	9.85	2.3	2.99	0.27	4.06	0.01	0.95	0.12	0.32	0.01	0.08	0.63	0.37			4.76	98.37
GX-06-85.2	Grand Conglomérat siltstone	36.5	14.65	12.9	6.92	9.72	2.94	0.86	0.03	0.84	0.4	0.06	0.01	0.01	2.84	0.4			13.4	99.24
GX-06-76	Grand Conglomérat siltstone	58.6	15.95	9.44	1.15	3.59	0.5	4.04	0.01	1.02	0.07	0.41		0.07	0.24	0.63			3.99	98.84
GX-08-104	Grand Conglomérat siltstone	58.5	14.95	9.66	1.94	3.46	0.09	3.94	0.01	0.95	0.12	0.52	0.01	0.08	0.54	0.07			4.92	99.15
GX-135-176	Grand Conglomérat siltstone	62.1	15.9	6.69	1.01	2.64	0.11	4.65	0.01	0.88	0.07	0.19		0.08	0.32	0.37			4	98.33
GX-142-199	Grand Conglomérat siltstone	63.8	16.15	6.1	1.05	2.61	0.12	4.59	0.01	0.91	0.08	0.21		0.07	0.3	0.36			4.42	100.12
GX-33-53	Grand Conglomérat siltstone	59.7	14.25	9.48	2.17	3.18	0.62	3.37	0.01	0.95	0.13	0.34	0.01	0.06	0.75	0.31			5.47	99.74
GX-34-118	Grand Conglomérat siltstone	58.1	13.65	10.15	2.52	3.47	0.45	3.15	0.01	0.91	0.21	0.37	0.01	0.06	0.92	0.27			5.66	98.72
GX-142-92.5	Quartz-carbonate vein	1	0.14	1.89	20.1	13.2	0.01	0.05		0.01	0.51	0.02	0.01		8.19	6.83	10.9		11.8	48.74
GX-12-129	Green/pink basement	3.75	0.54	0.48	29.5	20.8	0.01	0.24		0.04	0.09	0.03	0.02		12.05				45.2	100.7

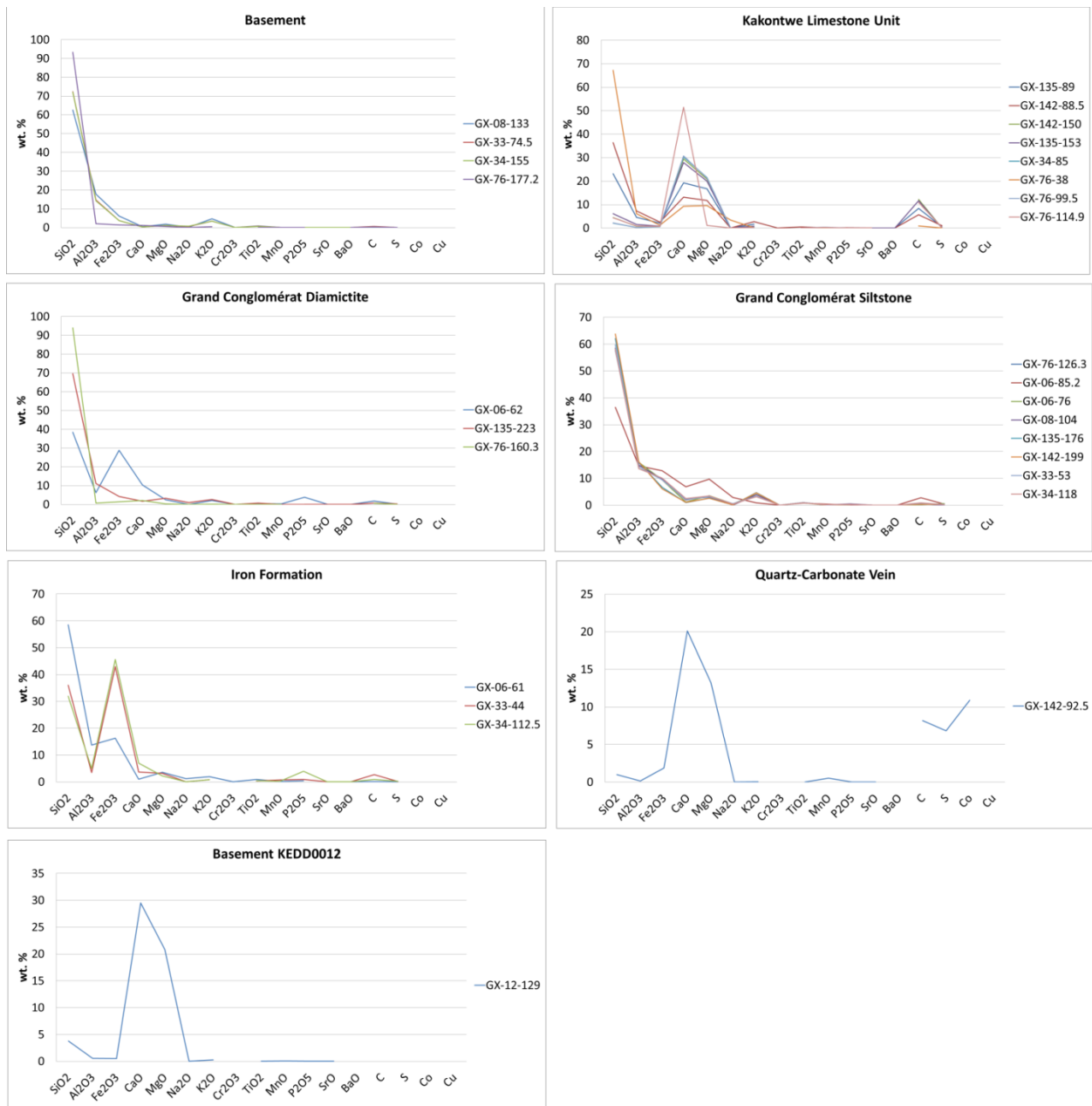


Figure B-1: Graphs of major element values (in weight %) of the basement, altered basement, Grand Conglomérat diamictite and siltstone, iron formation, Kakontwe Limestone unit, and quartz-carbonate veins from DDH KEDD0012.

Table B-2: Trace element values (in ppm) of the basement, altered basement, Grand Conglomérat diamictite and siltstone, iron formation, Kakontwe Limestone unit, and quartz-carbonate veins from DDH KEDD0012.

Sample Number	Lithology	Ba	Ce	Cr	Cs	Ga	Hf	Nb	Rb	Sr	Ta	Th	Ti	U	V	W	Zr	As	Bi	Hg	Sb	Se	Te
GX-08-133	Basement schist	840	113	70	5.7	24.3	9.8	21.5	208	50.7	1.9	28.3	0.6	3.95	71	4	371	3.7	0.11	0.044	0.4	0.4	0.01
GX-33-74.5	Basement schist	474	91.7	100	3.02	20.1	11.6	15.2	155.5	33.6	1.7	24.5		3.79	60	2	439	24.5	0.59	0.029	0.22	0.2	
GX-34-155	Basement schist	521	77.8	90	6.54	20.3	8.8	14.8	176.5	41.1	1.6	21.1	0.6	3.93	47	3	324	9.8	0.13	0.009	0.1	0.2	0.01
GX-76-177.2	Basement Quartzite	96.2	22.3	40	1.05	3.3	9	2.8	18.8	12.7	0.3	6.24		6.19	10	1	359	4.7	0.04	0.065	0.15		
GX-135-89	Kakontwe Limestone Unit	117	26.6	40	5.67	6.6	1.8	6.9	68.4	190	0.5	4.3	0.5	1.52	66	1	69	6.1	0.2	0.418	0.64	1.4	
GX-142-88.5	Kakontwe Limestone Unit	267	40.8	70	5.76	10.5	2.7	12.1	97.2	152	0.8	6.36	1.8	15.3	109	1	107	250	146.5	0.057	2.41	3.2	0.03
GX-142-150	Kakontwe Limestone Unit	28.5	5.1	10	0.37	1.1	0.3	1.2	9.3	126	0.1	0.94		0.81	17		12	3.8	0.3	0.051	0.28	0.6	0.01
GX-135-153	Kakontwe Limestone Unit	62.1	9.6	30	0.73	2.2	0.6	2.2	25.4	114	0.1	1.48		1.94	32		24	0.8	0.13	0.025	0.17	0.3	0.02
GX-34-85	Kakontwe Limestone Unit	23.1	3.2	10	0.13	0.8		0.4	3.6	154		0.87		0.65	11		5	3.1	0.05	0.014	0.39	0.3	0.01
GX-76-38	Kakontwe Limestone Unit	28	7.3	20	0.23	7.1	2.3	1.5	4.4	30.8	0.1	2.47		0.6	16		73	3.1	0.03	0.037	0.18		
GX-76-99.5	Kakontwe Limestone Unit	35.6	4.2	10	0.16	0.7		0.6	4.1	150.5		0.93		0.36	14		5	0.3	0.04	0.034	0.08	0.3	0.01
GX-76-114.9	Kakontwe Limestone Unit	46.1	10.1	10	0.12	1.7	0.4	1.8	10.1	1230	0.1	1.43		2.82	16		13	6.2	0.02	0.179	0.24	0.6	0.03
GX-06-62	Grand Conglomérat diamictite	137	48.8	50	20.5	9.4	2	10.4	199.5	181	0.8	9.47	0.6	1.8	64		91	4	0.18	0.04	0.3	0.7	0.02
GX-135-223	Grand Conglomérat diamictite	434	83.2	80	4.48	15.8	6.3	17.2	123.5	43.5	1.5	17.4		5.6	81	3	247	24.3	0.27	0.019	0.33	0.5	0.04
GX-76-160.3	Grand Conglomérat diamictite	37.2	22.2	60	0.28	1.8	4.2	1.1	5.5	30.8	0.1	2.39		0.49	11	1	159	11.2	0.04	0.122	0.24		0.01
GX-06-61	Iron Formation	240	106.5	90	7.68	19.2	6	24.7	111.5	35.6	1.8	20.4	0.5	3.07	119	2	226	2.7	0.12	0.046	0.38	0.5	0.02
GX-33-44	Iron Formation	97.7	27.6	50	4.6	5.9	2.2	7.1	47.6	80.2	0.5	5.13		1.03	61	1	87	27.8	3.76	0.015	0.34	0.4	0.03
GX-34-112.5	Iron Formation	96.2	44.5	40	3.51	7.8	0.9	9.2	50.1	179	0.7	7.7		1.42	62	1	38	9.9	0.68	0.012	0.32	0.9	0.07
GX-76-126.3	Grand Conglomérat siltstone	669	109	110	7.67	22.2	6.6	27.2	172.5	47.4	2	22.3	0.6	3.62	125	4	259	1.8	0.52	0.029	0.26	1	0.13
GX-06-85.2	Grand Conglomérat siltstone	124	2.8	250	2.2	14.4	1.4	4.4	41.6	80.1	0.2	0.7		0.33	208	2	51	56.8	1.39	0.073	0.27	0.6	0.02
GX-06-76	Grand Conglomérat siltstone	601	116.5	110	7.19	23	6.7	27.8	176.5	37	2.1	23.5	0.7	3.74	127	3	261	1.8	2.35	0.048	0.44	1.2	0.11
GX-08-104	Grand Conglomérat siltstone	655	99.1	110	6.17	22.1	6.5	26.2	164.5	45.1	2	21.6	0.6	11.05	129	3	247	8.2	0.18	0.058	0.43	0.5	0.02
GX-135-176	Grand Conglomérat siltstone	624	160	80	5.24	24.5	7.1	36	177.5	29.6	2.8	36.8	0.6	6.19	114	4	267	5.7	0.76	0.07	1.02	1.2	0.1
GX-142-199	Grand Conglomérat siltstone	598	150	80	5.52	24.8	7.1	35.6	177	31	2.9	34.8	0.6	5.24	112	4	269	14.6	0.88	0.035	0.54	1	0.08
GX-33-53	Grand Conglomérat siltstone	463	107	110	6.64	20.8	6.7	25.5	152.5	55.1	1.9	21.2	0.5	3.42	127	3	255	76.1	0.59	0.014	0.3	0.9	0.05
GX-34-118	Grand Conglomérat siltstone	505	95.9	90	3.86	19.8	6.8	24.5	124	68.2	1.8	20.1		3.36	116	2	260	13.1	0.38		0.21	0.8	0.02
GX-142-92.5	Quartz-carbonate vein	12.6	5.1	10	0.2	0.6		0.8	1.7	111.5		1.65		34.3	21		5	250	151	0.274	20.3	21.4	2.41
GX-12-129	Green/pink basement	31.1	3.6	10	0.19	0.8	0.2	0.8	6.2	165.5		0.51		0.5	15		10	0.3	0.1	0.021	0.08	0.2	0.01

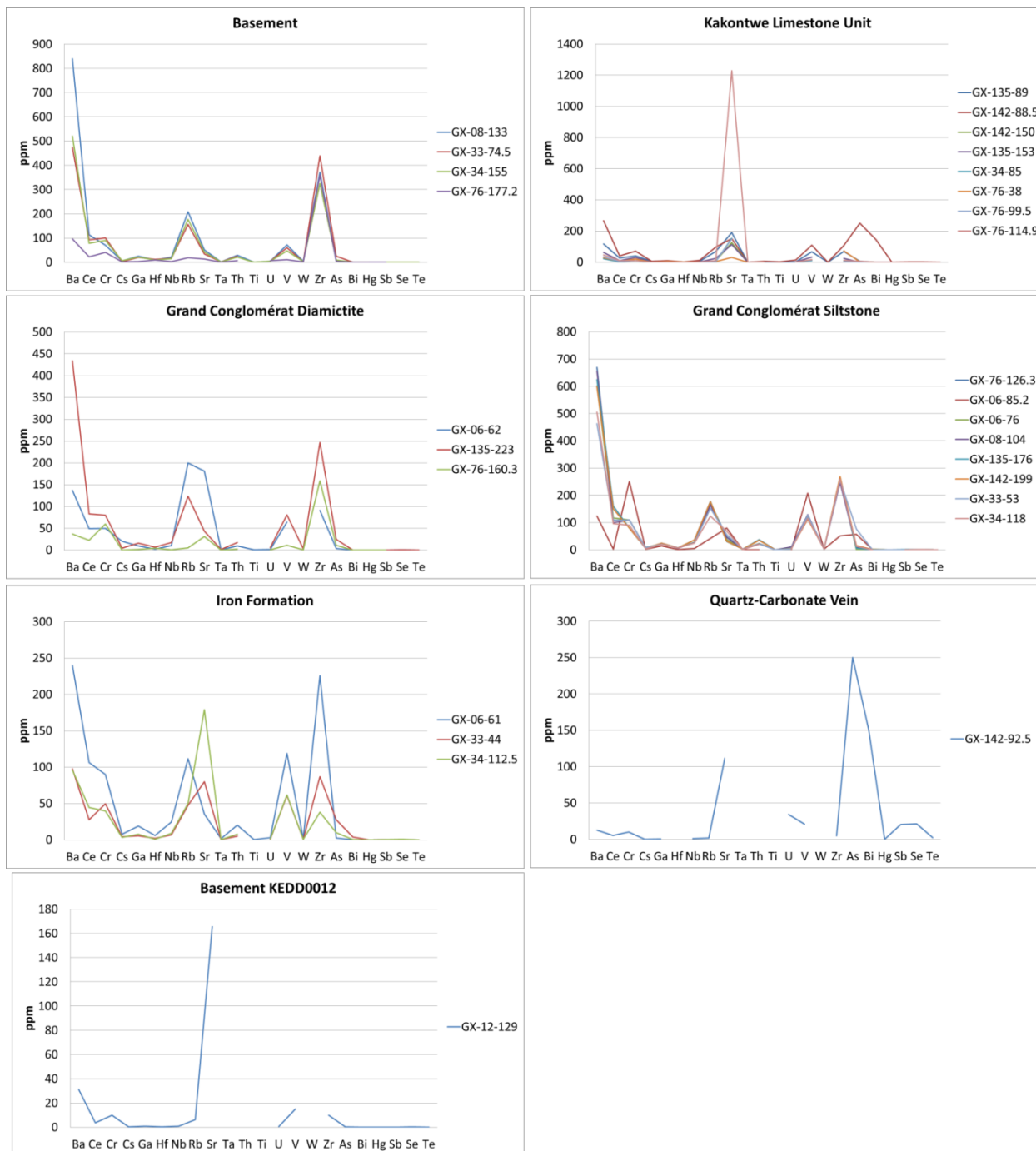


Figure B-2: Graphs of trace element values (in ppm) of the basement, altered basement, Grand Conglomérat diamictite and siltstone, iron formation, Kakontwe Limestone unit, and quartz-carbonate veins from DDH KEDD0012.

Table B-3: Metal values (in ppm) of the basement, altered basement, Grand Conglomérat diamictite and siltstone, iron formation, Kakontwe Limestone unit, and quartz-carbonate veins from DDH KEDD0012.

Sample Number	Lithology	Ag	Cd	Co	Cu	Mo	Ni	Pb	Zn
GX-08-133	Basement schist			14	357		19	17	25
GX-33-74.5	Basement schist			28	382	2	40	16	76
GX-34-155	Basement schist			14	251	1	20	15	39
GX-76-177.2	Basement Quartzite			6	56		2	11	27
GX-135-89	Kakontwe Limestone Unit		5	3	404	4	5	4	9140
GX-142-88.5	Kakontwe Limestone Unit	6.9		548	10000	15	46	29	48
GX-142-150	Kakontwe Limestone Unit			9	432	2	2		393
GX-135-153	Kakontwe Limestone Unit			8	222	1	3	7	54
GX-34-85	Kakontwe Limestone Unit			6	344	1		5	23
GX-76-38	Kakontwe Limestone Unit			5	1		10	3	29
GX-76-99.5	Kakontwe Limestone Unit			7	81	2	5	6	31
GX-76-114.9	Kakontwe Limestone Unit		0.6	2	4	1	4	9	1490
GX-06-62	Grand Conglomérat diamictite		0.9	18	192		10	5	48
GX-135-223	Grand Conglomérat diamictite			20	52	3	28	8	52
GX-76-160.3	Grand Conglomérat diamictite				1		1	4	2
GX-06-61	Iron Formation			32	624		31	4	62
GX-33-44	Iron Formation		0.9	24	649		1	2	31
GX-34-112.5	Iron Formation		1.3	13	80	1	5		47
GX-76-126.3	Grand Conglomérat siltstone			20	11		39		51
GX-06-85.2	Grand Conglomérat siltstone		0.5	72	2840		75	3	129
GX-06-76	Grand Conglomérat siltstone			21	4250		33	8	91
GX-08-104	Grand Conglomérat siltstone			39	822		33	3	50
GX-135-176	Grand Conglomérat siltstone			21	3930	2	41	4	67
GX-142-199	Grand Conglomérat siltstone			16	3570	1	39		68
GX-33-53	Grand Conglomérat siltstone			71	55	2	34	2	37
GX-34-118	Grand Conglomérat siltstone			28	41	2	35	4	51
GX-142-92.5	Quartz-carbonate vein	2.8		10000	4490	10	3680	14	16
GX-12-129	Green/pink basement			2	14		4	19	44

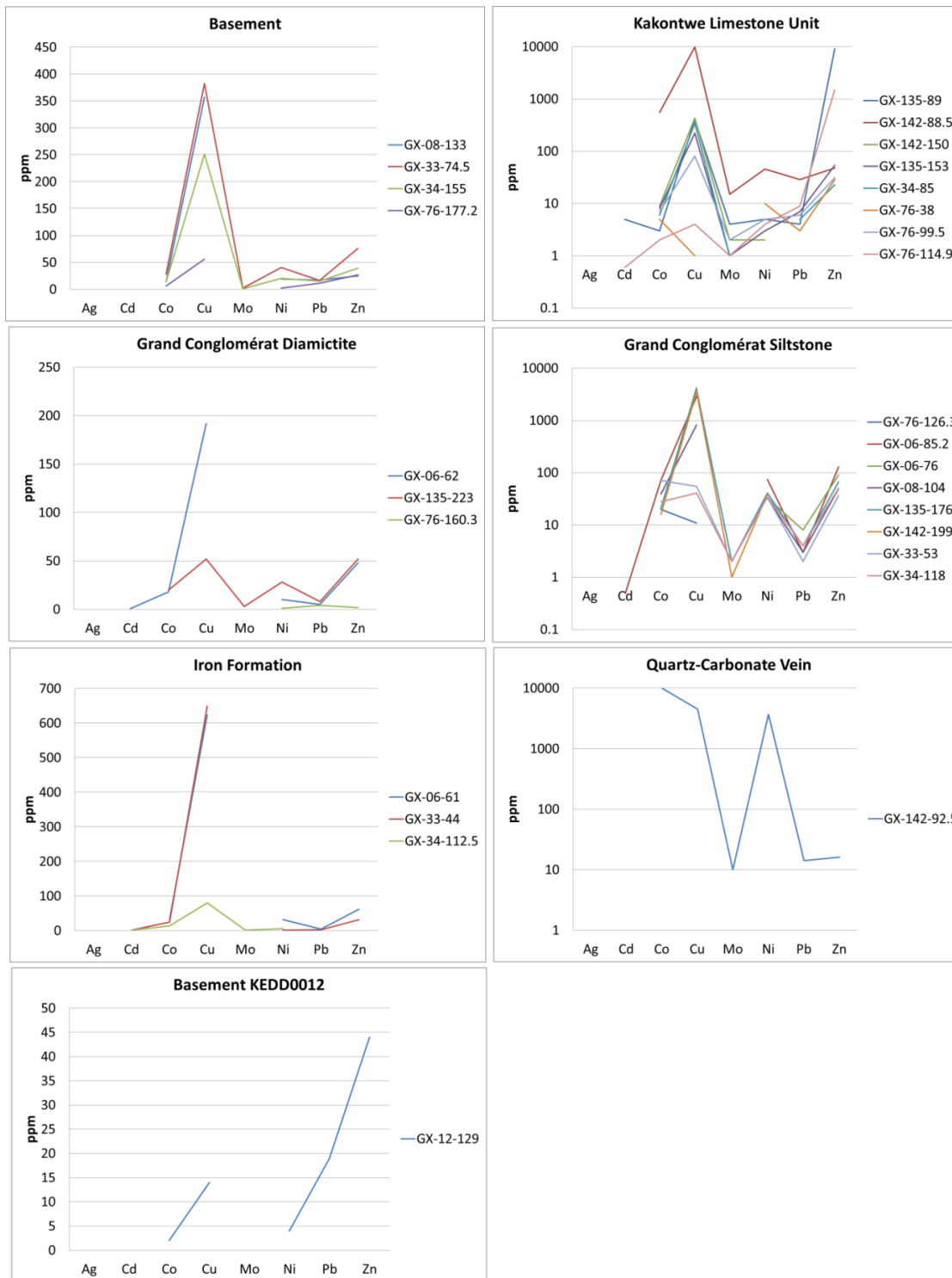


Figure B-3: Graphs of metal values (in ppm) of the basement, altered basement, Grand Conglomérat diamictite and siltstone, iron formation, Kakontwe Limestone unit, and quartz-carbonate veins from DDH KEDD0012.

Table B-4: Rare earth element values (in ppm) of the basement, altered basement, Grand Conglomérat diamictite and siltstone, iron formation, Kakontwe Limestone unit, and quartz-carbonate veins from DDH KEDD0012.

Sample Number	Lithology	La	Ce	Pr	Nd	Sm	Eu	Gd	Tb	Dy	Ho	Er	Yb	Lu
GX-08-133	Basement schist	13.98	69.16	1.28	22.65	1.35	0.10	1.44	0.03	1.25	0.05	0.42	0.44	0.01
GX-33-74.5	Basement schist	11.42	56.12	1.05	18.40	1.06	0.06	1.17	0.03	1.16	0.05	0.44	0.47	0.01
GX-34-155	Basement schist	9.62	47.61	0.90	15.97	0.94	0.05	1.05	0.03	1.05	0.04	0.37	0.39	0.01
GX-76-177.2	Basement Quartzite	2.56	13.65	0.22	3.74	0.21	0.01	0.21	0.01	0.21	0.01	0.08	0.11	
GX-135-89	Kakontwe Limestone Unit	3.01	16.28	0.31	5.93	0.39	0.03	0.48	0.01	0.55	0.02	0.21	0.21	
GX-142-88.5	Kakontwe Limestone Unit	4.69	24.97	0.48	9.01	0.53	0.03	0.62	0.02	0.64	0.03	0.24	0.25	0.01
GX-142-150	Kakontwe Limestone Unit	0.52	3.12	0.07	1.35	0.11	0.01	0.13		0.16	0.01	0.05	0.04	
GX-135-153	Kakontwe Limestone Unit	1.04	5.88	0.11	2.29	0.15	0.01	0.18		0.19	0.01	0.07	0.06	
GX-34-85	Kakontwe Limestone Unit	0.28	1.96	0.04	0.75	0.06	0.00	0.07		0.07		0.03	0.03	
GX-76-38	Kakontwe Limestone Unit	0.73	4.47	0.09	1.68	0.11	0.01	0.13		0.15	0.01	0.06	0.07	
GX-76-99.5	Kakontwe Limestone Unit	0.47	2.57	0.05	1.07	0.10	0.01	0.13		0.14	0.01	0.05	0.04	
GX-76-114.9	Kakontwe Limestone Unit	1.23	6.18	0.11	2.10	0.13	0.01	0.15		0.20	0.01	0.07	0.07	
GX-06-62	Grand Conglomérat diamictite	5.24	29.87	0.62	12.75	0.90	0.14	1.16	0.03	1.18	0.05	0.42	0.38	0.01
GX-135-223	Grand Conglomérat diamictite	10.59	50.92	0.87	15.08	0.83	0.06	0.90	0.02	0.90	0.04	0.36	0.37	0.01
GX-76-160.3	Grand Conglomérat diamictite	2.54	13.59	0.19	3.04	0.15	0.01	0.17	0.01	0.21	0.01	0.08	0.09	
GX-06-61	Iron Formation	13.41	65.18	1.13	19.52	1.07	0.08	1.07	0.03	1.13	0.05	0.45	0.48	0.01
GX-33-44	Iron Formation	3.37	16.89	0.31	5.70	0.30	0.02	0.39	0.01	0.48	0.02	0.23	0.26	0.01
GX-34-112.5	Iron Formation	4.86	27.23	0.53	10.13	0.63	0.06	0.84	0.02	0.95	0.05	0.39	0.38	0.01
GX-76-126.3	Grand Conglomérat siltstone	13.37	66.71	1.18	20.97	1.24	0.09	1.47	0.04	1.48	0.06	0.55	0.53	0.01
GX-06-85.2	Grand Conglomérat siltstone	0.33	1.71	0.03	0.70	0.09	0.01	0.31	0.01	0.63	0.03	0.23	0.19	0.00
GX-06-76	Grand Conglomérat siltstone	14.41	71.30	1.23	22.04	1.35	0.10	1.57	0.04	1.52	0.07	0.54	0.52	0.01
GX-08-104	Grand Conglomérat siltstone	11.80	60.65	1.10	19.85	1.20	0.09	1.40	0.04	1.48	0.07	0.55	0.53	0.01
GX-135-176	Grand Conglomérat siltstone	19.29	97.92	1.71	29.00	1.50	0.10	1.63	0.05	1.95	0.09	0.74	0.72	0.02
GX-142-199	Grand Conglomérat siltstone	18.39	91.80	1.59	26.81	1.35	0.08	1.41	0.04	1.54	0.07	0.58	0.58	0.01
GX-33-53	Grand Conglomérat siltstone	13.04	65.48	1.15	20.59	1.22	0.09	1.40	0.04	1.45	0.06	0.54	0.51	0.01
GX-34-118	Grand Conglomérat siltstone	11.61	58.69	1.04	18.54	1.10	0.08	1.36	0.04	1.42	0.06	0.51	0.50	0.01
GX-142-92.5	Quartz-carbonate vein	0.43	3.12	0.07	1.49	0.17	0.01	0.28	0.01	0.39	0.02	0.13	0.14	
GX-12-129	Green/pink basement	0.40	2.20	0.04	0.84	0.06		0.07		0.07		0.03	0.03	

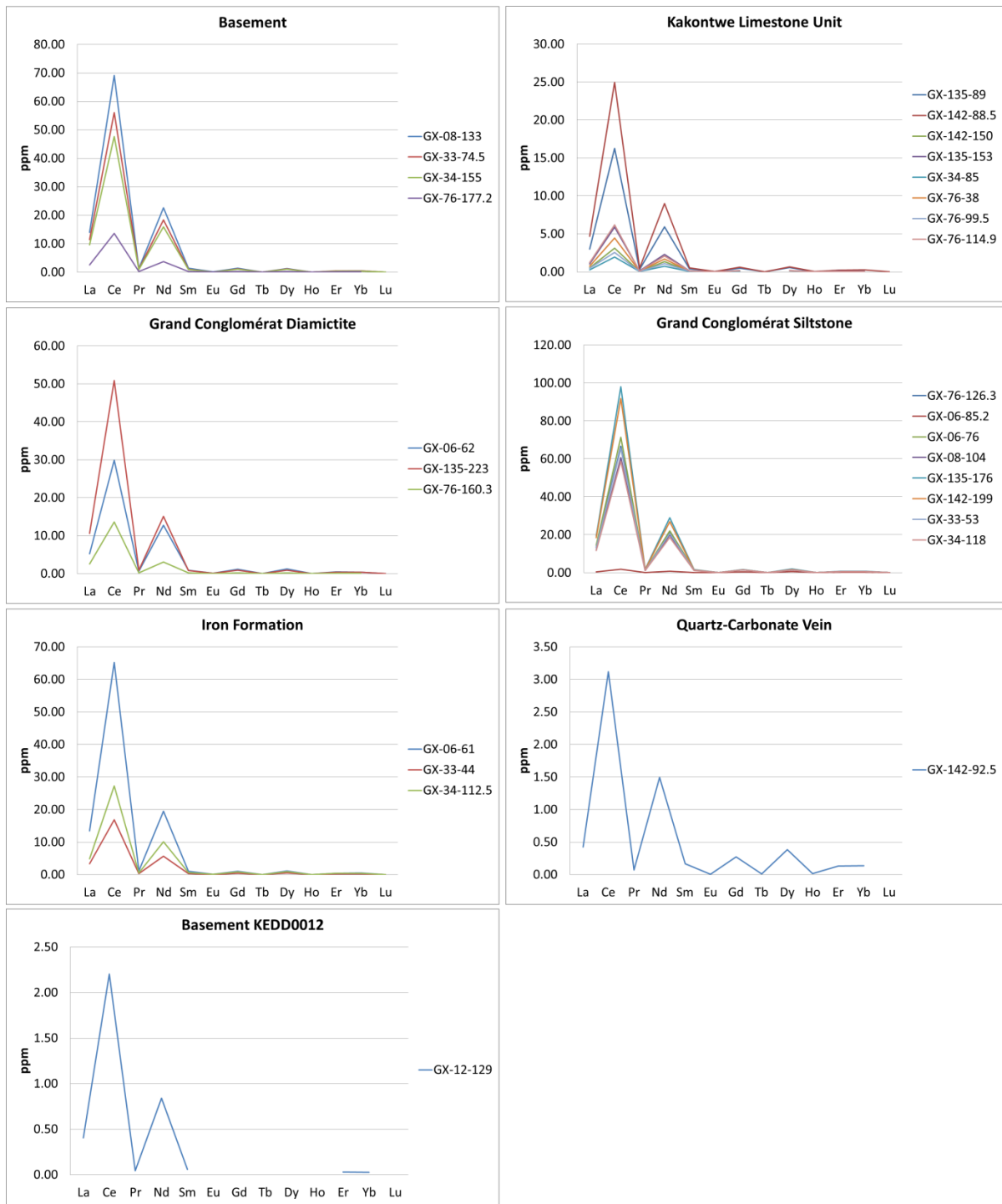


Figure B-4: Graphs of rare earth element values (in ppm) of the basement, altered basement, Grand Conglomérat diamictite and siltstone, iron formation, Kakontwe Limestone unit, and quartz-carbonate veins from DDH KEDD0012.

Table B-5: Heavy rare earth element values (in ppm) of the basement, altered basement, Grand Conglomérat diamictite and siltstone, iron formation, Kakontwe Limestone unit, and quartz-carbonate veins from DDH KEDD0012.

Sample Number	Lithology	Tb	Dy	Ho	Er	Yb	Lu
GX-08-133	Basement schist	0.03	1.25	0.05	0.42	0.44	0.01
GX-33-74.5	Basement schist	0.03	1.16	0.05	0.44	0.47	0.01
GX-34-155	Basement schist	0.03	1.05	0.04	0.37	0.39	0.01
GX-76-177.2	Basement Quartzite	0.01	0.21	0.01	0.08	0.11	
GX-135-89	Kakontwe Limestone Unit	0.01	0.55	0.02	0.21	0.21	
GX-142-88.5	Kakontwe Limestone Unit	0.02	0.64	0.03	0.24	0.25	0.01
GX-142-150	Kakontwe Limestone Unit		0.16	0.01	0.05	0.04	
GX-135-153	Kakontwe Limestone Unit		0.19	0.01	0.07	0.06	
GX-34-85	Kakontwe Limestone Unit		0.07		0.03	0.03	
GX-76-38	Kakontwe Limestone Unit		0.15	0.01	0.06	0.07	
GX-76-99.5	Kakontwe Limestone Unit		0.14	0.01	0.05	0.04	
GX-76-114.9	Kakontwe Limestone Unit		0.20	0.01	0.07	0.07	
GX-06-62	Grand Conglomérat diamictite	0.03	1.18	0.05	0.42	0.38	0.01
GX-135-223	Grand Conglomérat diamictite	0.02	0.90	0.04	0.36	0.37	0.01
GX-76-160.3	Grand Conglomérat diamictite	0.01	0.21	0.01	0.08	0.09	
GX-06-61	Iron Formation	0.03	1.13	0.05	0.45	0.48	0.01
GX-33-44	Iron Formation	0.01	0.48	0.02	0.23	0.26	0.01
GX-34-112.5	Iron Formation	0.02	0.95	0.05	0.39	0.38	0.01
GX-76-126.3	Grand Conglomérat siltstone	0.04	1.48	0.06	0.55	0.53	0.01
GX-06-85.2	Grand Conglomérat siltstone	0.01	0.63	0.03	0.23	0.19	0.00
GX-06-76	Grand Conglomérat siltstone	0.04	1.52	0.07	0.54	0.52	0.01
GX-08-104	Grand Conglomérat siltstone	0.04	1.48	0.07	0.55	0.53	0.01
GX-135-176	Grand Conglomérat siltstone	0.05	1.95	0.09	0.74	0.72	0.02
GX-142-199	Grand Conglomérat siltstone	0.04	1.54	0.07	0.58	0.58	0.01
GX-33-53	Grand Conglomérat siltstone	0.04	1.45	0.06	0.54	0.51	0.01
GX-34-118	Grand Conglomérat siltstone	0.04	1.42	0.06	0.51	0.50	0.01
GX-142-92.5	Quartz-carbonate vein	0.01	0.39	0.02	0.13	0.14	
GX-12-129	Green/pink basement		0.07		0.03	0.03	

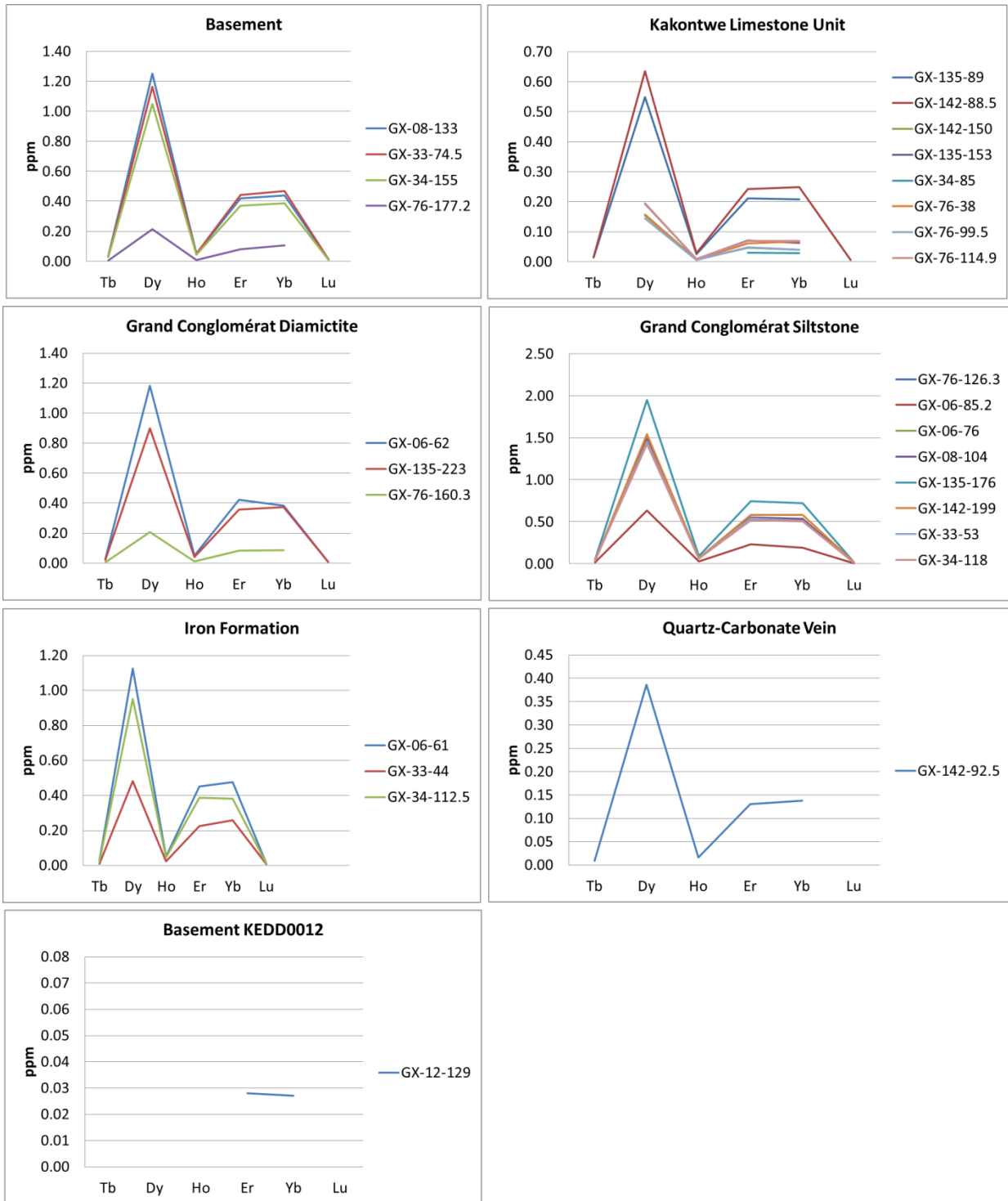


Figure B-5: Graphs of heavy rare earth elements (values in ppm) of the basement, altered basement, Grand Conglomérat diamictite and siltstone, iron formation, Kakontwe Limestone unit, and quartz-carbonate veins from DDH KEDD0012.

Table B-6: Light rare earth element values (in ppm) of the basement, altered basement, Grand Conglomérat diamictite and siltstone, iron formation, Kakontwe Limestone unit, and quartz-carbonate veins from DDH KEDD0012.

Sample Number	Lithology	La	Ce	Pr	Nd	Sm	Eu	Gd
GX-08-133	Basement schist	13.98	69.16	1.28	22.65	1.35	0.10	1.44
GX-33-74.5	Basement schist	11.42	56.12	1.05	18.40	1.06	0.06	1.17
GX-34-155	Basement schist	9.62	47.61	0.90	15.97	0.94	0.05	1.05
GX-76-177.2	Basement Quartzite	2.56	13.65	0.22	3.74	0.21	0.01	0.21
GX-135-89	Kakontwe Limestone Unit	3.01	16.28	0.31	5.93	0.39	0.03	0.48
GX-142-88.5	Kakontwe Limestone Unit	4.69	24.97	0.48	9.01	0.53	0.03	0.62
GX-142-150	Kakontwe Limestone Unit	0.52	3.12	0.07	1.35	0.11	0.01	0.13
GX-135-153	Kakontwe Limestone Unit	1.04	5.88	0.11	2.29	0.15	0.01	0.18
GX-34-85	Kakontwe Limestone Unit	0.28	1.96	0.04	0.75	0.06	0.00	0.07
GX-76-38	Kakontwe Limestone Unit	0.73	4.47	0.09	1.68	0.11	0.01	0.13
GX-76-99.5	Kakontwe Limestone Unit	0.47	2.57	0.05	1.07	0.10	0.01	0.13
GX-76-114.9	Kakontwe Limestone Unit	1.23	6.18	0.11	2.10	0.13	0.01	0.15
GX-06-62	Grand Conglomérat diamictite	5.24	29.87	0.62	12.75	0.90	0.14	1.16
GX-135-223	Grand Conglomérat diamictite	10.59	50.92	0.87	15.08	0.83	0.06	0.90
GX-76-160.3	Grand Conglomérat diamictite	2.54	13.59	0.19	3.04	0.15	0.01	0.17
GX-06-61	Iron Formation	13.41	65.18	1.13	19.52	1.07	0.08	1.07
GX-33-44	Iron Formation	3.37	16.89	0.31	5.70	0.30	0.02	0.39
GX-34-112.5	Iron Formation	4.86	27.23	0.53	10.13	0.63	0.06	0.84
GX-76-126.3	Grand Conglomérat siltstone	13.37	66.71	1.18	20.97	1.24	0.09	1.47
GX-06-85.2	Grand Conglomérat siltstone	0.33	1.71	0.03	0.70	0.09	0.01	0.31
GX-06-76	Grand Conglomérat siltstone	14.41	71.30	1.23	22.04	1.35	0.10	1.57
GX-08-104	Grand Conglomérat siltstone	11.80	60.65	1.10	19.85	1.20	0.09	1.40
GX-135-176	Grand Conglomérat siltstone	19.29	97.92	1.71	29.00	1.50	0.10	1.63
GX-142-199	Grand Conglomérat siltstone	18.39	91.80	1.59	26.81	1.35	0.08	1.41
GX-33-53	Grand Conglomérat siltstone	13.04	65.48	1.15	20.59	1.22	0.09	1.40
GX-34-118	Grand Conglomérat siltstone	11.61	58.69	1.04	18.54	1.10	0.08	1.36
GX-142-92.5	Quartz-carbonate vein	0.43	3.12	0.07	1.49	0.17	0.01	0.28
GX-12-129	Green/pink basement	0.40	2.20	0.04	0.84	0.06		0.07

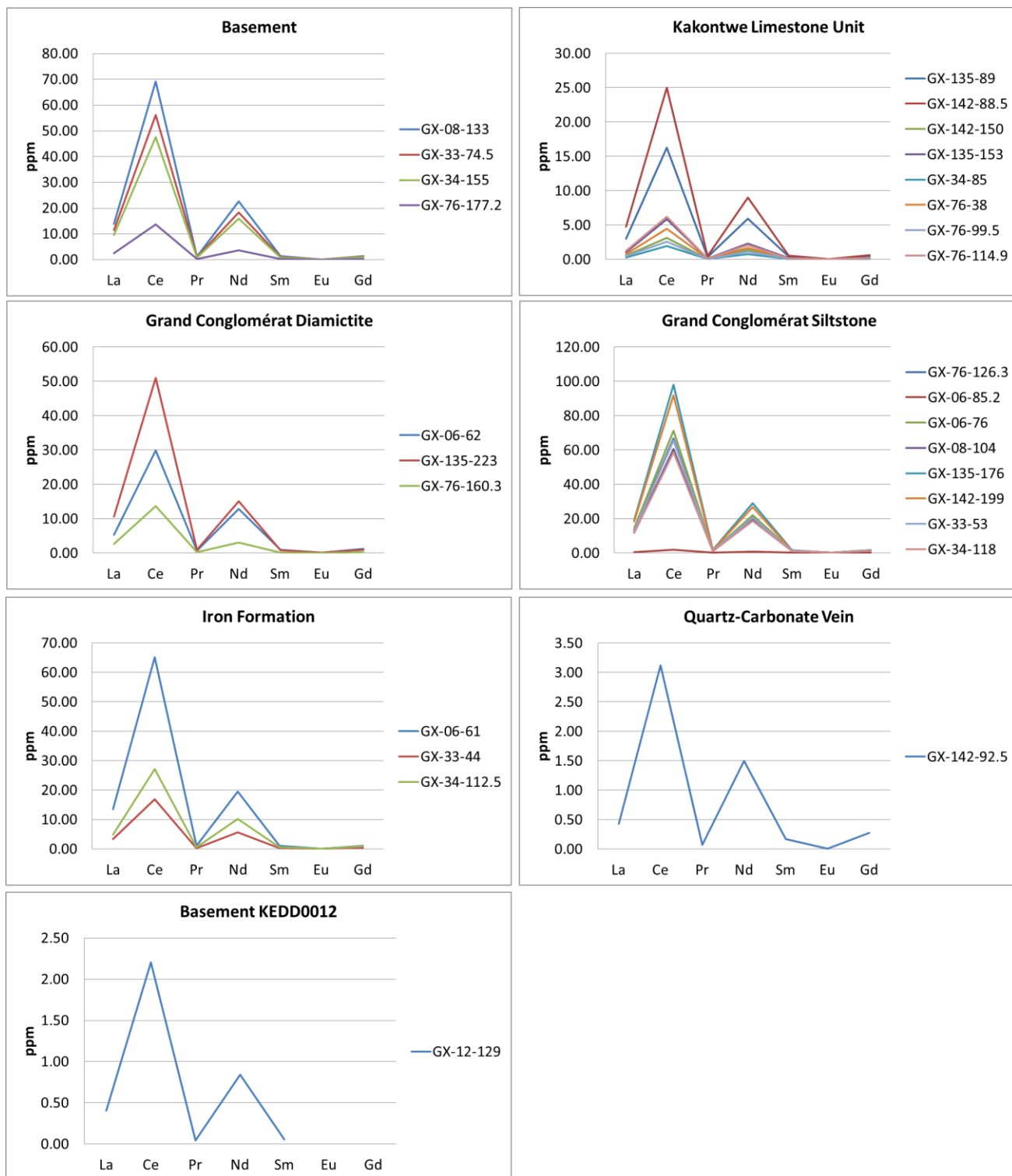


Figure B-6: Graphs of light rare earth element values (in ppm) of the basement, altered basement, Grand Conglomérat diamictite and siltstone, iron formation, Kakontwe Limestone unit, and quartz-carbonate veins from DDH KEDD0012.

APPENDIX C  
SOIL GEOCHEMISTRY SURVEY DATA AND PROJECTED TO SURFACE COPPER  
GRADE

**C.1 Methods**

A soil geochemical sampling program was conducted by First Quantum Ltd. across the Lusale basin. Samples were collected every 100 meters on 1000 meter line spacing. A higher density of soil samples (every 50 meters on 250 meter line spacing) was collected over the Fishtie deposit area. Sample collection was in compliance with company QA/QC procedures. The samples were analyzed at ALS Chemex in Johannesburg, South Africa. Data are presented in ppm and weight percent values (Figures C-1 through C-4). Each sample point was geocoded with easting and northing values using a UTM WGS84 Zone35S projection. Weight percent and ppm values of elements at each geocoded point were gridded using the average of coincident points in a minimum curvature method to generate continuously variable surfaces that were clipped using a buffer technique. The minimum curvature method utilized an interior tension of 25 and an exterior tension of 0, a maximum of 50 iterations between points, and a cell size of 25. Each surface was contoured at spacing specific to the range of values for each element.

The soil geochemical data was then compared to known areas of copper sulfide mineralization at the Fishtie deposit by projection of drill results to surface. A map of copper grades in the Fishtie deposit projected to surface was created by three-dimensional modeling of ore grade in Discover 3D and projecting values to surface as a grid file. This grid was contoured using the same methods used for soil geochemical data (Figure C-5).

## **C.2 Results**

Copper, cobalt, phosphorus, bismuth, and sulfur in soil samples are strongly correlated to the main ore zone at Fishtie, with iron and manganese showing a comparatively weaker correlation (Figures C-1, C-2). Bismuth is the most strongly correlated, followed by copper, cobalt, sulfur, phosphorous, manganese, and iron. Arsenic, calcium, and magnesium are enriched along a northeast-striking corridor that transects the eastern and satellite structural domains (Figures C-1, C-2)

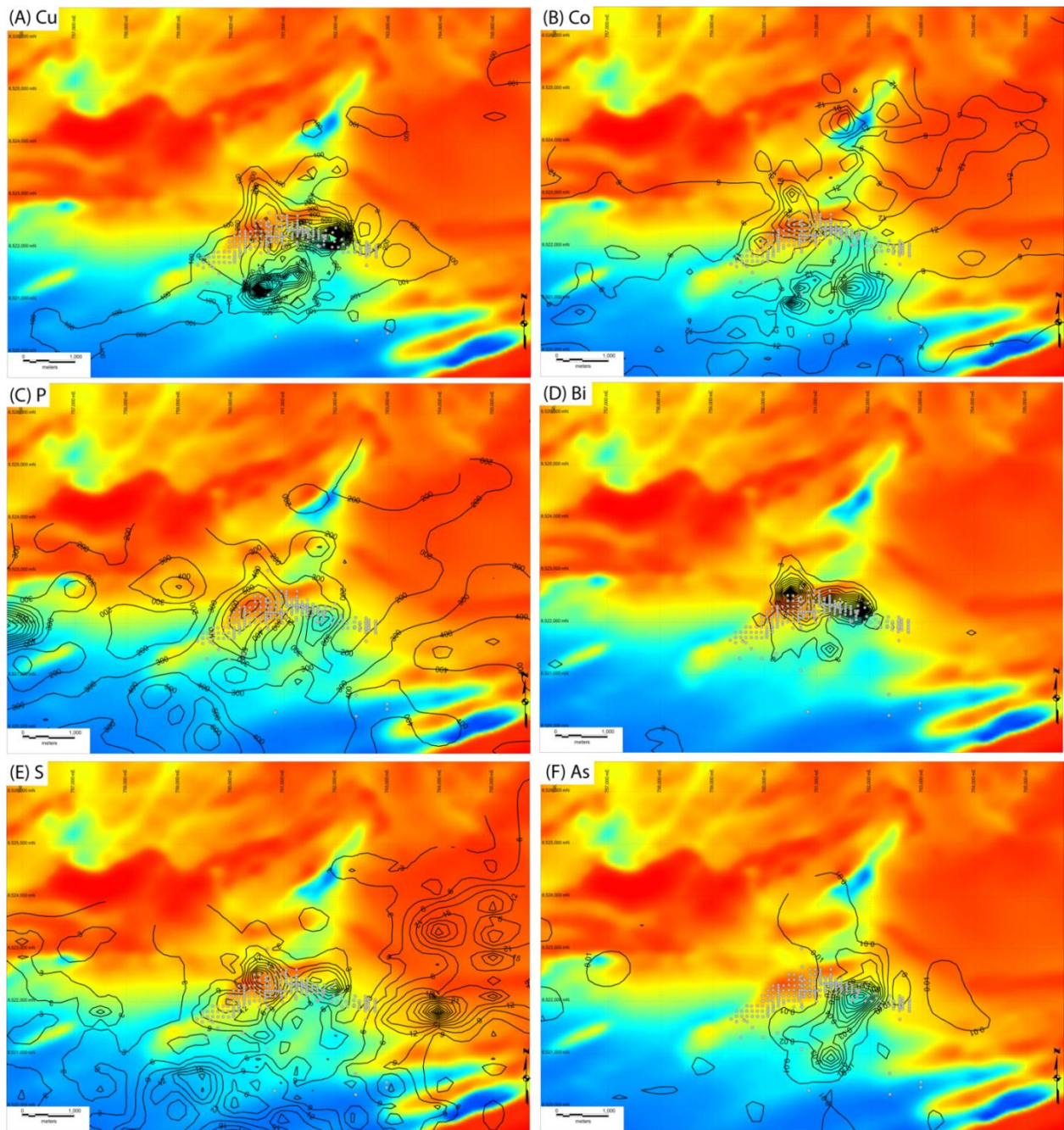


Figure C-1: Soil geochemistry contours on RTP magnetic map of the Fishtie area: (A) Cu (ppm), (B) Co (ppm), (C) P (ppm), (D) Bi (ppm), (E) S (wt. %), (F) As (wt. %).

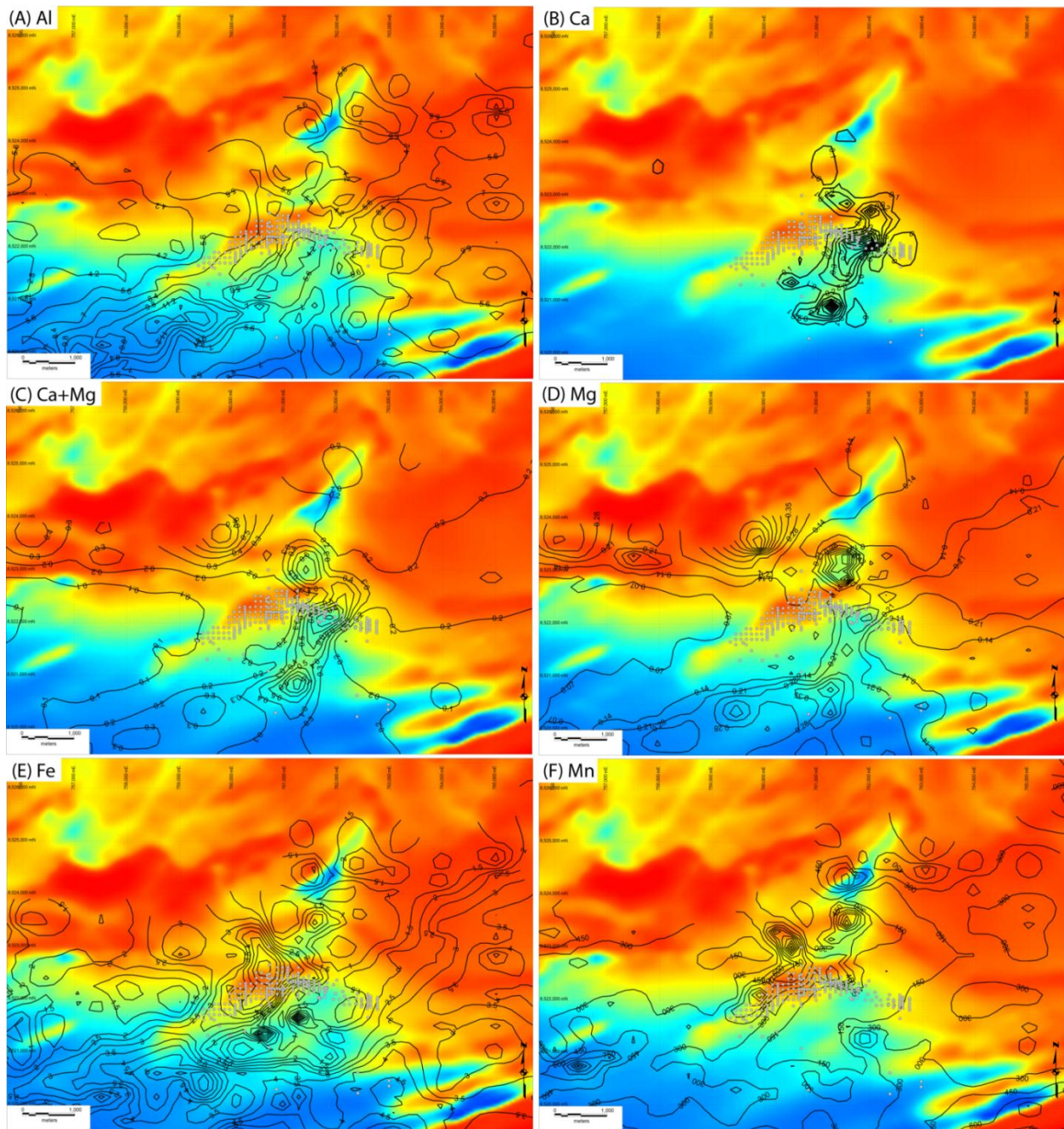


Figure C-2: Soil geochemistry contours on RTP magnetic map of the Fishtie area: (A) Al (wt. %), (B) Ca (wt. %), (C) Ca and Mg (wt. %), (D) Mg (wt. %), (E) Fe (wt. %), (F) Mn (ppm).

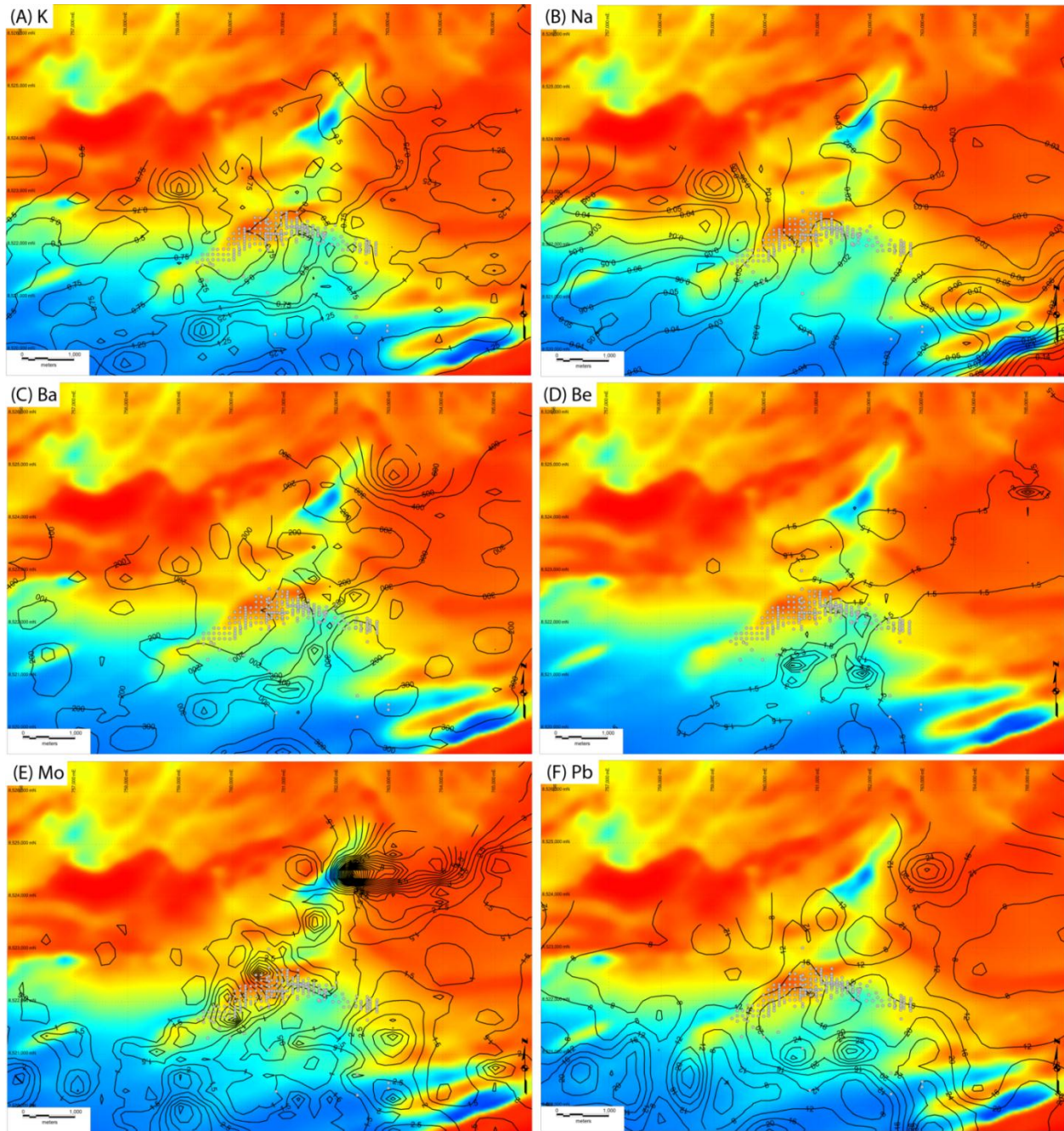


Figure C-3: Soil geochemistry contours on RTP magnetic map of the Fishtie area: (A) K (wt. %), (B) Na (wt. %), (C) Ba (ppm), (D) Be (ppm), (E) Mo (ppm), (F) Pb (ppm).

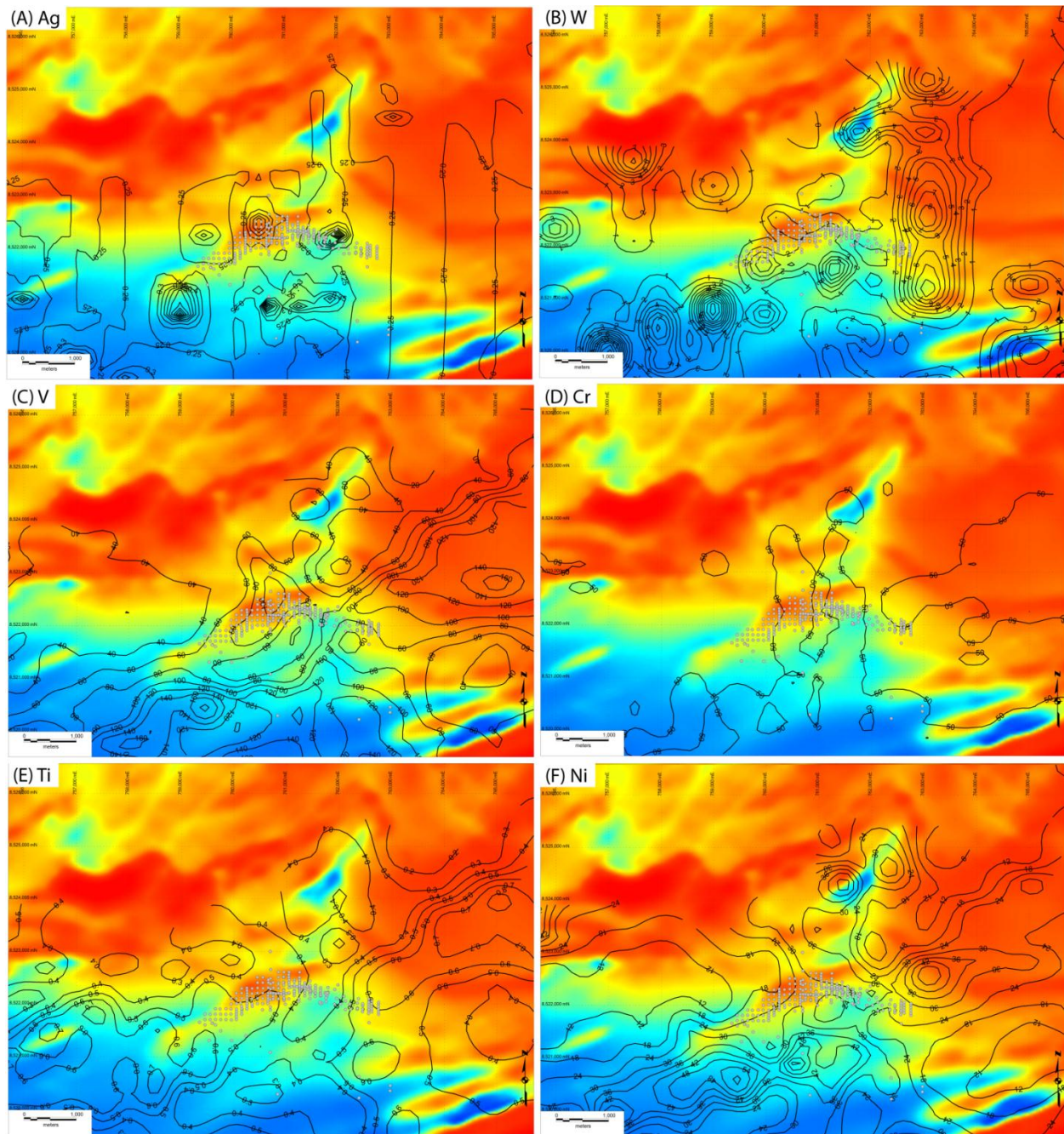


Figure C-4: Soil geochemistry contours on RTP magnetic map of the Fishtie area: (A) Ag (ppm), (B) W (ppm), (C) V (ppm), (D) Cr (ppm), (E) Ti (wt. %), (F) Ni (ppm).

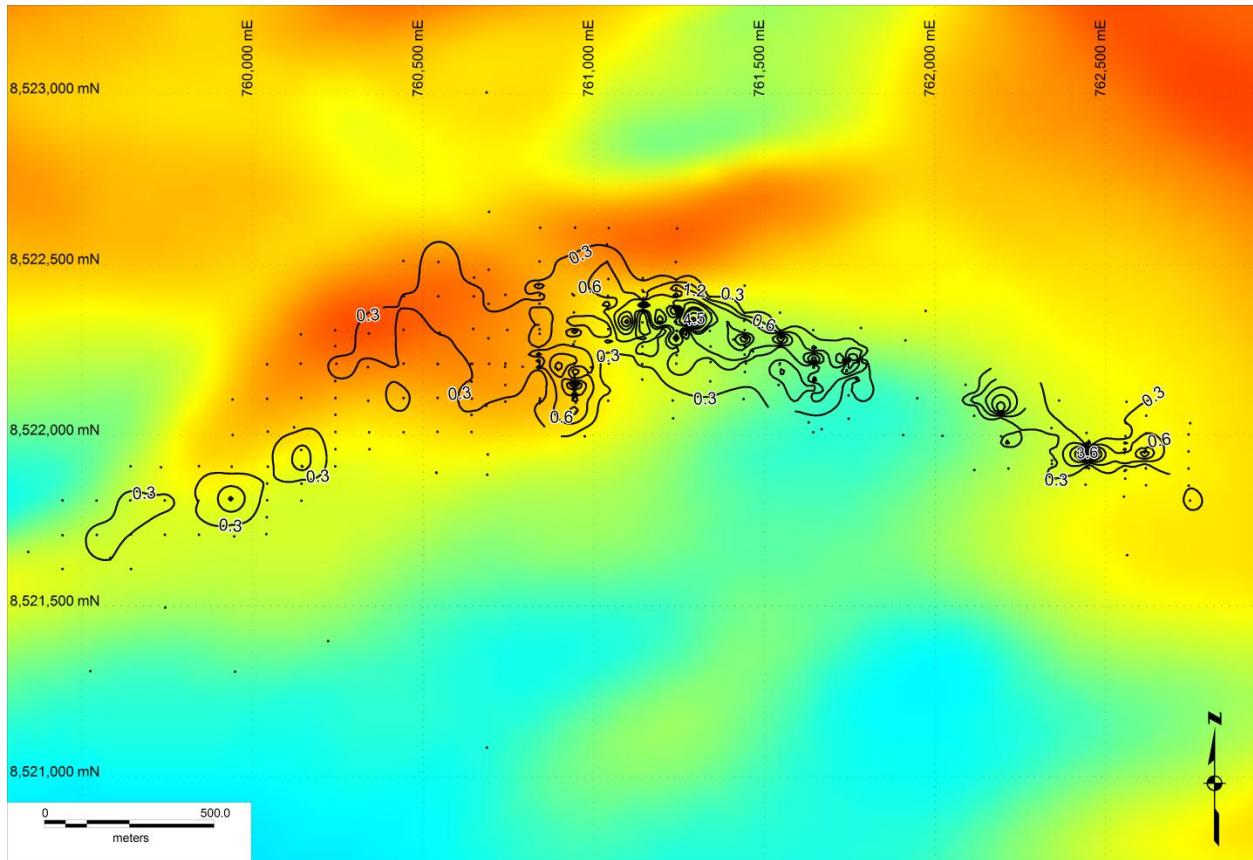


Figure C-5: Projected to surface copper grade of the Fishtie copper deposit for comparison to soil geochemistry graphs. Values are in weight percent.

## APPENDIX D

### THREE-DIMENSIONAL MODELING

#### **D.1 Methods**

Three-dimensional modeling of basement topography, structural features, diamictite, and ore grade at the Fishtie copper deposit was completed to better constrain structural architecture and controls on mineralization. Modeling was completed in Leapfrog Mining. Isosurfaces of basement rocks, diamictite, and copper grade were created by compositing of discrete interval values to create points which were then interpolated using default histogram equalization. Faults were drawn in manually using interpretations derived from cross sections and 3D basement topography. Interpolation of the volume of diamictite did not produce a perfectly continuous and clipped isosurface and is not presented. However, diamictite intervals are highlighted in brown to show their relationship with copper grade isosurfaces.

#### **D.2 Results**

The highest-grade portions of the deposit are restricted to supergene zones near the Grand Conglomérat-Kakontwe units contact that are closely related to faults (high gradients of basement topography; Figures D-1, D-2, and D-3). The hypogene portion of the deposit is centered in the central and satellite structural domains. In the central structural domain a series of east-striking normal faults define a half-graben that controlled copper mineralization in the Grand Conglomérat diamictite. In the satellite structural domain north-striking faults with significant east directed down drop were the first order control on copper mineralization in Kakontwe Limestone unit.

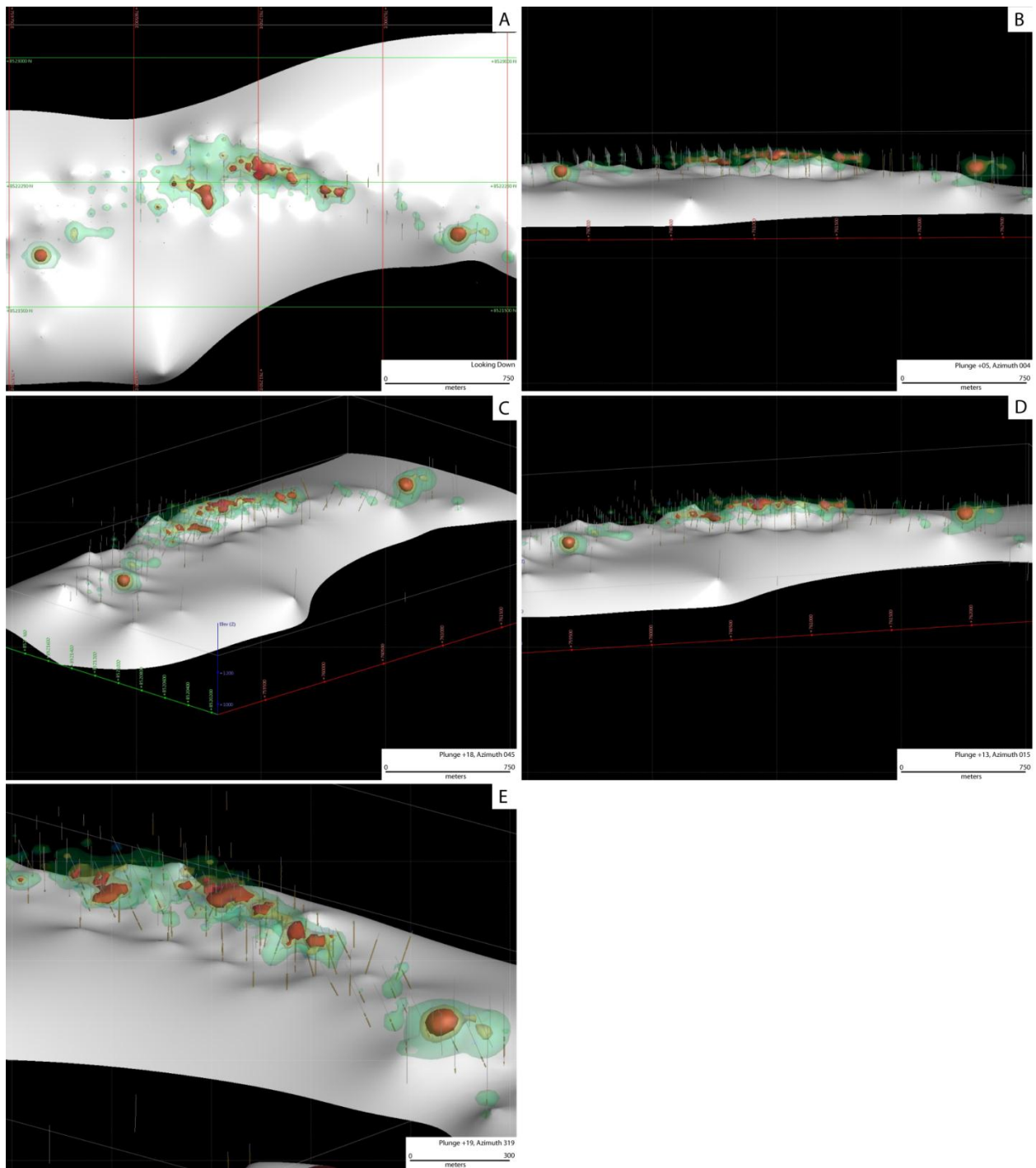


Figure D-1: Three-dimensional model of the upper surface of basement rocks (white), copper grade, and drill holes. The green ore shell represents a 0.5% Cu cutoff. The yellow ore shell represents a 1.1% Cu cutoff and the red ore shell represents a 1.6% Cu cutoff. Brown intervals in drill holes denote diamictite packages. (A) Top view of the entire deposit area. (B) North-directed view of the entire deposit. (C) Northeast directed view of the entire deposit. (D) North-northeast-directed view of the entire deposit. (E) Northwest-directed view of the main orebody in the central structural domain and the satellite orebody.

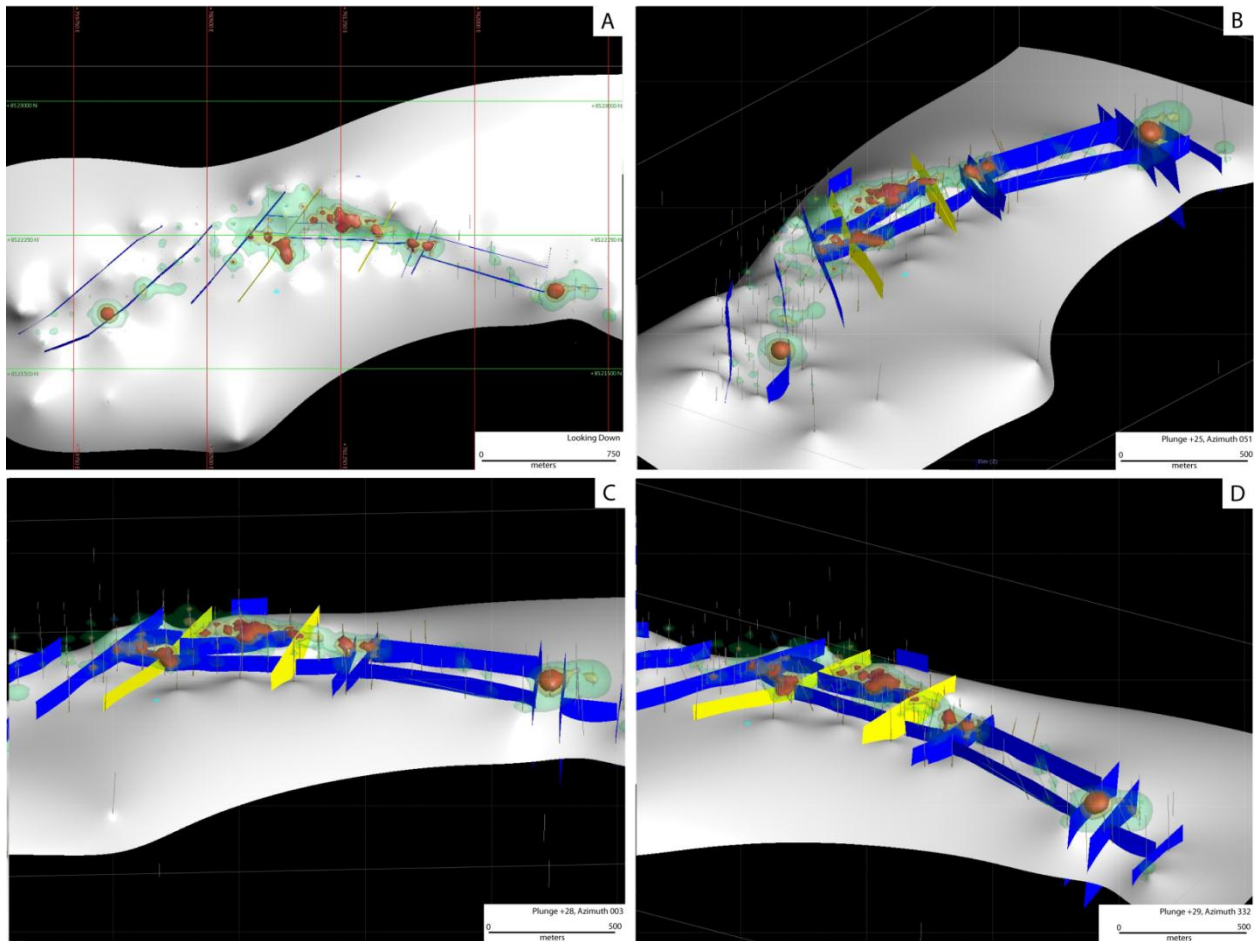


Figure D-2: Three-dimensional model of the upper surface of basement rocks (white), copper grade, drill holes, and faults. The green ore shell represents a 0.5% Cu cutoff. The yellow ore shell represents a 1.1% Cu cutoff and the red ore shell represents a 1.6% Cu cutoff. Brown intervals in drill holes denote diamictite packages. Blue faults are high angle normal; yellow faults had strike-slip movement. (A) Top view of the entire deposit. (B) Northeast directed view of the entire deposit. (C) North directed view of the central, eastern, and satellite structural domains. (D) Northwest directed view of the satellite, eastern, and central domains.

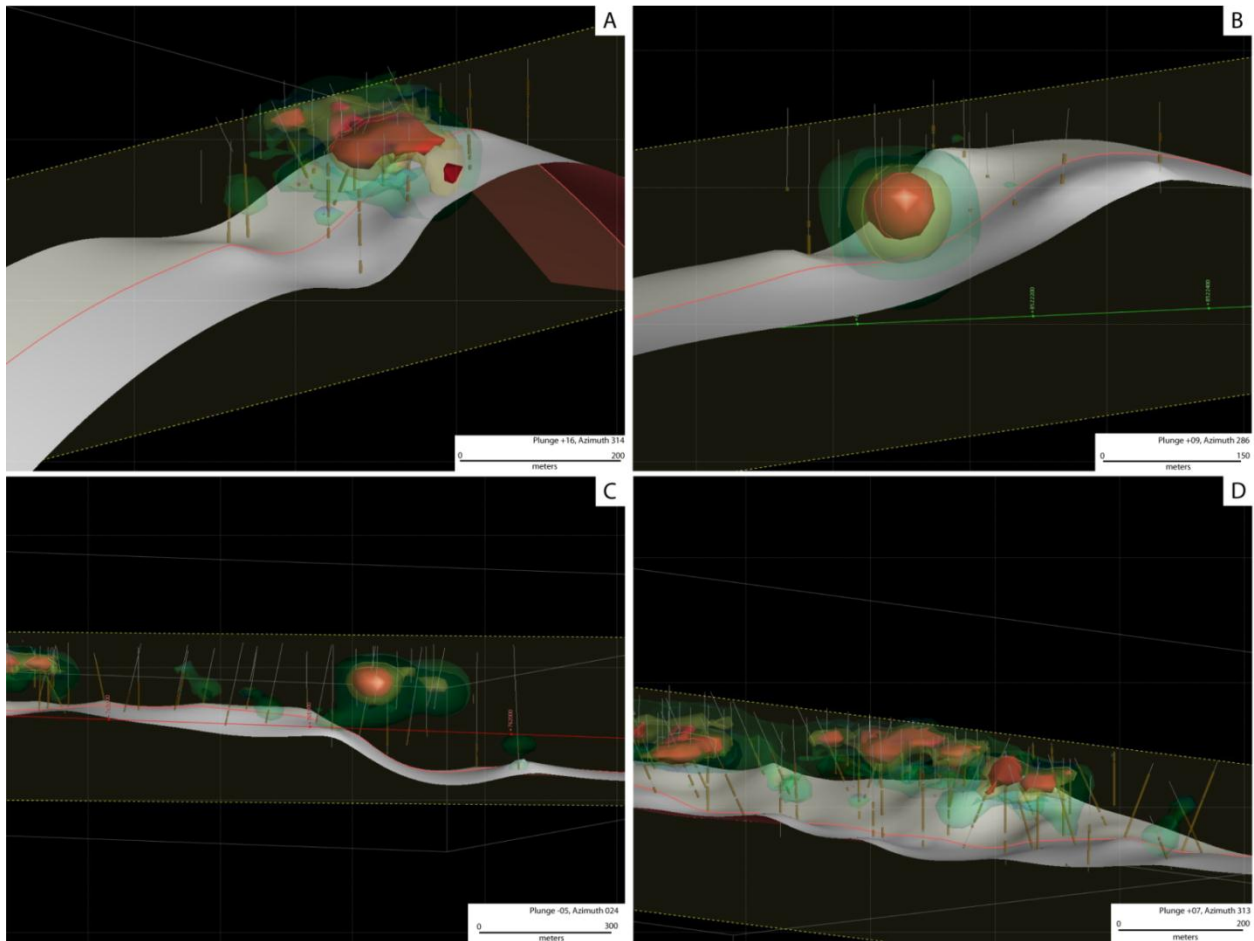


Figure D-3: Three-dimensional slices of the upper surface of basement rocks (white), copper grade, and drill holes. The green ore shell represents a 0.5% Cu cutoff. The yellow ore shell represents a 1.1% Cu cutoff and the red ore shell represents a 1.6% Cu cutoff. Brown intervals in drill holes denote diamictite packages. (A) North-south slice, north-west directed view of the central structural domain. (B) North-south slice, north-northwest-directed view of the western structural domains. (C) East-west slice, north directed view of the eastern and satellite structural domains. (D) East-west slice, north-northwest directed view of the central structural domain.

## APPENDIX E

### MODAL ABUNDANCE OF MINERALS

#### **E.1 Methods**

A PC-based software suite, iDiscover™, allowed estimation of modal abundances of minerals from data acquired using the QEMSCAN® instrument at the Colorado School of Mines. The QEMSCAN® instrument is an automated quantitative mineralogy tool that utilizes a Carl Zeiss EVO50 SEM platform, four Bruker energy dispersive (EDS) detectors, and proprietary software to produce false-colored mineral maps from backscatter electron signals and EDS (energy dispersive spectrometer) spectra.

#### **E.2 Results**

Weakly altered diamictite has a higher modal abundance of quartz, albite, and potassium feldspar compared to the three end member types (muscovite, chlorite, and biotite) of altered diamictite. Chlorite and biotite altered diamictite have higher modal abundance of apatite. All alteration styles show strong depletion in quartz and feldspar content relative to weakly altered diamictite. Iron formation is enriched in apatite and ankerite. Kakontwe Limestone unit limestone from a weakly altered portion of the deposit (eastern structural domain) is composed of calcite with lesser dolomite, ankerite, quartz, potassium feldspar, and pyrite. Kakontwe Limestone unit dolomitic siltstone from the satellite structural domain is composed of dolomite with interbeds of quartz and potassium feldspar (Figure E-1).

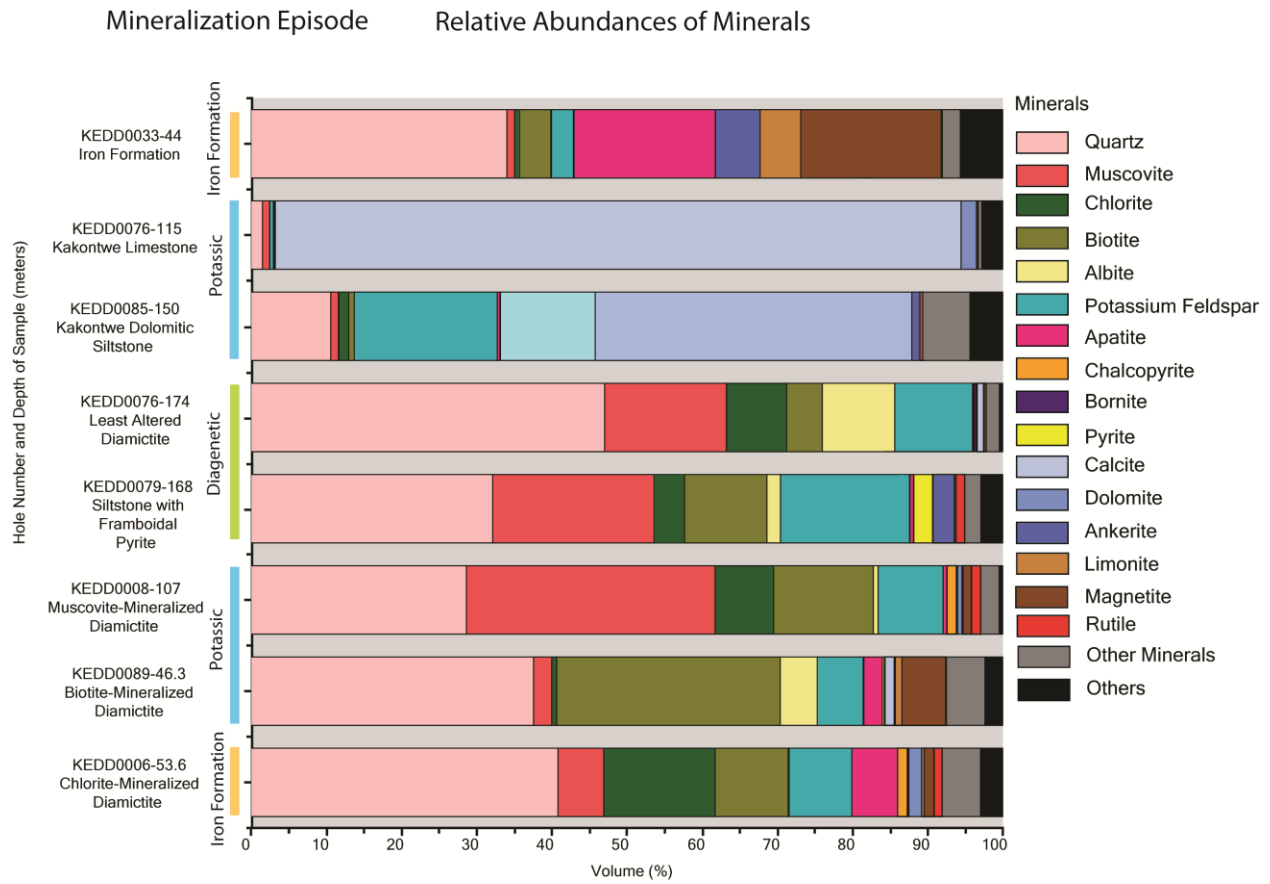


Figure E-1: Modal abundances of minerals calculated from QEMSCAN® analysis. Mineralization episode, sample description, hole number, and depth of sample (in meters) labeled for each sample.

## APPENDIX F

### CARBON AND OXYGEN ISOTOPE ANALYSIS

#### **F.1 Methods**

Forty-eight samples from the unaltered Nguba Group Kakontwe Limestone unit, twenty-one samples from mineralized portions of the Kakontwe Limestone unit, eight samples from calcite veins hosting or closely associated with copper sulfide minerals, and two samples from ankerite in iron formation were analyzed for stable carbon and oxygen isotopic values.

Approximately 50-100  $\mu\text{g}$  of sample was liberated from whole rock by micro drilling. The weight and size of the samples was dependent on the purity of the carbonate and mineralogy. Analysis was conducted at Colorado School of Mines Stable Isotope Laboratory where each sample was quantitatively acidified in vacuum using 100% orthophosphoric acid at 90 °C in an on-line auto-sampler. Carbon dioxide created in the reaction was cryogenically purified and analyzed for stable carbon and oxygen isotopes simultaneously using a Micromass Isoprime stable isotope ratio mass spectrometer with traditional dual-inlet techniques. Calcium carbonate powder from Colorado Yule Marble (CYM) calibrated with the 93-NBS-18 and 93-NBS-19 standards from the National Institute of Standards and Technology was used to calibrate laboratory standard reference gas.  $\delta^{13}\text{C}$  and  $\delta^{18}\text{O}$  permil values were calculated using the Vienna Pee Dee Formation Belemnite (VPDB) international reference standard.  $\delta^{17}\text{O}$  abundance in all data was corrected using the equations of Craig (1957). Repeated analysis yielded precision of 0.07‰ for carbon and 0.09‰ for oxygen. The  $\delta^{18}\text{O}$  (VPDB) data was converted to  $\delta^{18}\text{O}$  (SMOW) using the Freidman and O'Neil equation (1977) [ $\delta^{18}\text{O}$  (SMOW) = 1.03086 ( $\delta^{18}\text{O}$  (SMOW)) + 30.86].

## F.2 Results

See table F-1.

Table F-1: Carbon and oxygen isotopic values of unaltered and altered Kakontwe Limestone unit, calcite veins, and ankerite in iron formation.

Sample Number	Hole Number	Depth (m)	Sample Location	$\delta^{13}\text{C}$ (‰ VPDB)	$\delta^{18}\text{O}$ (‰ SMOW)
C1	KEDD0079	55	Unaltered Kakontwe Limestone Unit	4.0	27.1
C2	KEDD0079	59.4	Unaltered Kakontwe Limestone Unit	3.9	26.9
C3	KEDD0079	64	Unaltered Kakontwe Limestone Unit	3.7	27.1
C4	KEDD0079	70	Unaltered Kakontwe Limestone Unit	3.6	27.1
C5	KEDD0079	74	Unaltered Kakontwe Limestone Unit	3.5	27.3
C6	KEDD0079	79.9	Unaltered Kakontwe Limestone Unit	3.3	26.3
C7	KEDD0079	84	Unaltered Kakontwe Limestone Unit	3.2	26.6
C8	KEDD0079	89	Unaltered Kakontwe Limestone Unit	3.1	26.6
C9	KEDD0079	94	Unaltered Kakontwe Limestone Unit	3.0	26.3
C10	KEDD0079	100	Unaltered Kakontwe Limestone Unit	2.8	26.5
C11	KEDD0079	104.5	Unaltered Kakontwe Limestone Unit	2.5	26.6
C12	KEDD0079	110	Unaltered Kakontwe Limestone Unit	2.5	26.9
C13	KEDD0079	115	Unaltered Kakontwe Limestone Unit	2.1	26.4
C14	KEDD0079	119.5	Unaltered Kakontwe Limestone Unit	2.0	26.2
C15	KEDD0079	123	Unaltered Kakontwe Limestone Unit	1.8	26.1
C16	KEDD0079	126.5	Unaltered Kakontwe Limestone Unit	1.2	25.9
C17	KEDD0079	130	Unaltered Kakontwe Limestone Unit	1.6	26.1
C18	KEDD0079	135	Unaltered Kakontwe Limestone Unit	1.5	26.4
C19	KEDD0079	140.5	Unaltered Kakontwe Limestone Unit	-0.2	25.7
C20	KEDD0079	141.5	Unaltered Kakontwe Limestone Unit	-0.9	25.5
C21	KEDD0079	143.7	Unaltered Kakontwe Limestone Unit	-1.3	23.3
C22	KEDD0076	19.3	Unaltered Kakontwe Limestone Unit	4.1	27.4
C23	KEDD0076	20.6	Unaltered Kakontwe Limestone Unit	4.1	27.7
C24	KEDD0076	23	Unaltered Kakontwe Limestone Unit	4.0	27.8
C25	KEDD0076	26	Unaltered Kakontwe Limestone Unit	3.9	27.4
C26	KEDD0076	29	Unaltered Kakontwe Limestone Unit	3.8	26.8
C27	KEDD0076	32	Unaltered Kakontwe Limestone Unit	3.7	26.9
C28	KEDD0076	36.2	Unaltered Kakontwe Limestone Unit	3.6	27.0
C29	KEDD0076	40	Unaltered Kakontwe Limestone Unit	3.4	26.7
C30	KEDD0076	46.5	Unaltered Kakontwe Limestone Unit	3.3	26.4
C31	KEDD0076	48	Unaltered Kakontwe Limestone Unit	3.3	26.3
C32	KEDD0076	51	Unaltered Kakontwe Limestone Unit	3.2	26.8
C33	KEDD0076	52.5	Unaltered Kakontwe Limestone Unit	2.1	24.9
C34	KEDD0076	53.2	Unaltered Kakontwe Limestone Unit	3.1	26.1
C35	KEDD0076	57.6	Unaltered Kakontwe Limestone Unit	2.9	26.1
C36	KEDD0076	60.7	Unaltered Kakontwe Limestone Unit	2.9	25.9
C37	KEDD0076	66.2	Unaltered Kakontwe Limestone Unit	2.7	26.3
C38	KEDD0076	68.8	Unaltered Kakontwe Limestone Unit	2.7	26.1
C39	KEDD0076	72	Unaltered Kakontwe Limestone Unit	2.4	26.2
C40	KEDD0076	75.5	Unaltered Kakontwe Limestone Unit	2.3	25.9
C41	KEDD0076	80.5	Unaltered Kakontwe Limestone Unit	1.9	25.3
C42	KEDD0076	83	Unaltered Kakontwe Limestone Unit	1.8	25.4
C43	KEDD0076	89	Unaltered Kakontwe Limestone Unit	1.6	26.0
C44	KEDD0076	94.5	Unaltered Kakontwe Limestone Unit	1.3	25.7
C45	KEDD0076	96.4	Unaltered Kakontwe Limestone Unit	1.5	26.1
C46	KEDD0076	101	Unaltered Kakontwe Limestone Unit	1.5	26.4
C47	KEDD0076	108	Unaltered Kakontwe Limestone Unit	1.5	26.7
C48	KEDD0076	109.8	Unaltered Kakontwe Limestone Unit	-1.5	24.4
C49	KEDD0134A	144	Altered Kakontwe Limestone Unit	2.1	25.5
C50	KEDD0135	121.8	Altered Kakontwe Limestone Unit	1.3	21.3
C51	KEDD0135	170	Altered Kakontwe Limestone Unit	1.3	26.3
C52	KEDD0134A	164.5	Altered Kakontwe Limestone Unit	1.4	24.8
C53	KEDD0135	156	Altered Kakontwe Limestone Unit	1.6	25.2
C54	KEDD0135	131.1	Altered Kakontwe Limestone Unit	2.4	25.3
C55	KEDD0135	131.1	Vein	2.4	25.5
C56	KEDD0085	77	Altered Kakontwe Limestone Unit	3.0	25.7
C57	KEDD0142	190.7	Altered Kakontwe Limestone Unit	0.3	25.8
C58	KEDD0142	163.5	Altered Kakontwe Limestone Unit	2.1	25.0
C59	KEDD0142	162.5	Altered Kakontwe Limestone Unit	2.2	25.7
C60	KEDD0142	103.5	Vein	1.9	23.0
C61	KEDD0034	123.3	Vein	-4.9	17.3
C62	KEDD0034	85.5	Altered Kakontwe Limestone Unit	-8.5	16.1
C63	KEDD0034	85	Altered Kakontwe Limestone Unit	1.5	27.6
C64	KEDD0034	82	Altered Kakontwe Limestone Unit	1.6	27.3
C65	KEDD0089	55.4	Altered Kakontwe Limestone Unit	-0.7	18.9
C66	KEDD0064	43.7	Vein	-1.0	16.5
C67	KEDD0063	66	Vein	-8.6	15.8
C68	KEDD0006	65.7	Vein	-8.2	16.3
C69	KEDD0006	51.7	Vein	-5.3	18.2
C70	KEDD0006	44.6	Vein	-3.3	18.4
C71	KEDD0008	141	Vein	-5.4	11.6
C72	KEDD0008	81.5	Altered Kakontwe Limestone Unit	-3.3	15.9
C73	KEDD0008	70.2	Altered Kakontwe Limestone Unit	1.4	26.2
C74	KEDD0008	71.5	Altered Kakontwe Limestone Unit	1.0	26.0
C75	KEDD0008	63.8	Altered Kakontwe Limestone Unit	1.4	27.0
C76	KEDD0008	58.3	Altered Kakontwe Limestone Unit	1.6	26.5
C77	KEDD0008	58.3	Vein	1.5	26.6
C78	KEDD0008	83.4	Altered Kakontwe Limestone Unit	-1.7	17.4
C81	KEDD0033	44	Ankerite in Iron Formation	-8.6	16.3
C82	KEDD0034	112.9	Ankerite in Iron Formation	-8.6	16.1

## APPENDIX G

### SULFUR ISOTOPE ANALYSIS

#### **G.1 Methods**

Samples of apparently diagenetic pyrite from the Grand Conglomérat diamictite and siltstone, as well as chalcopyrite and ore stage pyrite from both the Grand Conglomérat and Kakontwe Limestone units were analyzed to help constrain the genesis of the Fishtie deposit. Approximately 30-100  $\mu\text{g}$  of sulfide was derived by micro drilling with sample size dependent on mineralogy and relationship with host rock (i.e. massive, disseminated, clast rim). Each sample was combusted at 1050°C in a Eurovector 3000 elemental analyzer at the Colorado School of Mines Stable Isotope Laboratory. Sulfur dioxide generated through combustion reactions was delivered to a Micromass Isoprime stable isotope ratio mass spectrometer in continuous flow mode in a stream of helium carrier gas. Isotope transient peaks of samples were compared to a laboratory standard sulfur dioxide reference gas calibrated against laboratory standard barium sulfate. Isotopic values are reported using the  $\delta$  notation as a permil difference from the Canyon Diablo Trilobite (CDT) international reference (Beaudoin et al., 1994). Laboratory barium sulfate was calibrated to CDT through repeated measurement against NBS-127 barium sulfate standard reference material from the National Institute of Standards and Technology. This method yielded precision of 0.01‰ determined from two blind duplicates of sample material.

#### **G.2 Results**

See Table G-1 and Figure G-1.

Table G-1: Sulfur isotopic values of chalcopyrite, bornite, and pyrite from the Grand Conglomérat and Kakontwe Limestone units. Sulfides from the Kakontwe Limestone unit plot at consistently higher values than those from the Grand Conglomérat unit.

Sample Number	Hole Number	Depth (m)	Style of Mineralization	Sulfide Hosting Unit	Structural Domain	Mineral	$\delta^{34}\text{S}$ (‰ CDT)
S1	KEDD0017	186.5	Vein	Grand Conglomérat	Western	Chalcopyrite	6.5
S2	KEDD0017	188	Vein	Grand Conglomérat	Western	Chalcopyrite	4.9
S3	KEDD0142	115.3	Vein	Kakontwe Limestone	Satellite	Chalcopyrite	19.0
S4	KEDD0142	117.3	Vein	Kakontwe Limestone	Satellite	Chalcopyrite	17.7
S5	KEDD0135	68	Bedding plane	Kakontwe Limestone	Satellite	Chalcopyrite	23.4
S6	KEDD0135	87	Bedding plane	Kakontwe Limestone	Satellite	Pyrite	25.7
S7	KEDD0135	95	Bedding plane	Kakontwe Limestone	Satellite	Chalcopyrite	22.7
S8	KEDD0135	113.7	Bedding plane	Kakontwe Limestone	Satellite	Chalcopyrite	13.8
S9	KEDD0135	116.5	Vein	Kakontwe Limestone	Satellite	Chalcopyrite	12.7
S10	KEDD0135	199	Clast rim	Grand Conglomérat	Satellite	Chalcopyrite	11.2
S11	KEDD0135	200.7	Disseminated	Grand Conglomérat	Satellite	Chalcopyrite	9.9
S12	KEDD0135	108.7	Bedding plane	Kakontwe Limestone	Satellite	Pyrite	15.3
S13	KEDD0134A	175.5	Bedding plane	Kakontwe Limestone	Satellite	Chalcopyrite	25.1
S14	KEDD0134A	200.6	Disseminated	Grand Conglomérat	Satellite	Chalcopyrite	10.1
S15	KEDD0085	84.5	Bedding plane	Kakontwe Limestone	Satellite	Chalcopyrite	21.9
S16	KEDD0085	82.6	Bedding plane	Kakontwe Limestone	Satellite	Chalcopyrite	20.5
S17	KEDD0142	136.5	Bedding plane	Kakontwe Limestone	Satellite	Chalcopyrite	14.1
S18	KEDD0064	49.3	Vein	Grand Conglomérat	Central	Chalcopyrite	2.5
S19	KEDD0064	58.2	Vein	Grand Conglomérat	Central	Bornite	5.8
S20	KEDD0064	82.5	Disseminated	Grand Conglomérat	Central	Pyrite	10.8
S21	KEDD0063	79.9	Disseminated	Grand Conglomérat	Central	Pyrite	11.6
S22	KEDD0063	121.5	Disseminated	Grand Conglomérat	Central	Chalcopyrite	8.5
S23	KEDD0063	122	Disseminated	Grand Conglomérat	Central	Chalcopyrite	8.2
S24	KEDD0063	123.9	Disseminated	Grand Conglomérat	Central	Chalcopyrite	8.4
S25	KEDD0006	76.6	Clast rim	Grand Conglomérat	Central	Chalcopyrite	12.8
S26	KEDD0076	125.8	Disseminated	Basement	Central	Chalcopyrite	4.6
S27	KEDD0085	132	Clast rim	Grand Conglomérat	Central	Chalcopyrite	7.3
S28	KEDD0006	56.2	Clast rim	Grand Conglomérat	Central	Chalcopyrite	8.3
S29	KEDD0079	168.5	Disseminated	Grand Conglomérat	Western	Pyrite	11.4
S30	KEDD0079	168	Disseminated	Grand Conglomérat	Western	Pyrite	11.4
S31	KEDD0089	51.6	Clast rim	Grand Conglomérat	Central	Chalcopyrite	11.0

